DISCLAIMER:

This document does not meet the
current format guidelines of
the Graduate School at
The University of Texas at Austin.

It has been published for
informational use only.

Copyright

by

SomayeSadat Rasouli

2017

The dissertation committee for SomayeSadat Rasouli certifies that this is the approved version of the following dissertation:

Degradation Mechanisms of Pt and Pt Alloy Nanocatalysts in Proton Exchange Membrane Fuel Cells

Committee:

Paulo J. Ferreira, Supervisor

Arumugam Manthiram

Guihua Yu

Naotoshi Nakashima

Kenji Higashida

Anusorn Kongkanand

Degradation Mechanisms of Pt and Pt Alloy Nanocatalysts in Proton Exchange Membrane Fuel Cells

by

SomayeSadat Rasouli, B.Sc.; M.Sc.

Dissertation

Presented to the Faculty of the Graduate School of
The University of Texas at Austin
in Partial Fulfillment
of the Requirements
for the Degree of

Doctor of Philosophy
The University of Texas at Austin
May 2017

Dedicated to

my parents and my husband

Without whose love and support, this could not have happened.

Acknowledgements

I would like to thank my PhD advisor, Prof. Paulo Ferreira for his supervision support. I am very grateful for the trust he put in my abilities and for the opportunities he provided to work at various laboratories and researcher groups and grow as a researcher. I would also like to thank my committee members: Prof. Arumugam Manthiram, Prof. Naotoshi Nakashima, Professor Kenji Higashida, Professor Guihua Yu, and Dr. Anusorn Kongkanand for serving on my committee and providing very valuable feedback on my research.

In addition to the honor to have Professor Nakashima and Professor Higashida in my committee, I would like to express my utmost gratitude for hosting me and welcoming me to their lab during my stay in Japan. Furthermore, a special “Thank you” goes to Kyoko Nakashima for her support and hospitality. どうもどうもありがとうございました.

I want to thank Dr. Ji-Ping Zhou and Dr. Karalee Jarvis, the Transmission Electron Microscopy (TEM) facility managers for teaching me how to use the equipment used for this research. I also thank Professor Syo Matsumura, the director of Ultra Microscopy Research Center at Kyushu University, Japan, Professor Tsuyohiko Fujigaya, and Dr. Tomokazu Yamamoto at Kyushu University, Japan for having given me access to their advanced microscopy facilities. I would like to thank Professor Peter Crozier, for the unique opportunity to work in his outstanding lab at Arizona State University. In addition, I would like to acknowledge Dr. Karl Weiss, Dr. Shery Chang, and Dr. Jingyu Liu at

LeRoy Eyring Center for Solid State Science at Arizona State University for their help with the microscopy facility used for this research.

I would like to thank my lab mates: Charles Amos, Daniel Groom, Hu Stone, and Kang Yu for all their help and valuable discussions. I would like to remember Federico Cardenas whose brilliance and kindness shall never be forgotten.

I thank the Fuel Cell Technologies Office of the U.S. Department of Energy (DOE), Office of Energy Efficiency and Renewable for providing financial support for this work.

Also, I would like to thank my father, Mr. Hassan Rasouli and my mother Mrs. Fatemeh Hossein Zadeh for a lifetime of support and encouragement. They taught me how to question everything and how not to give up in the difficult situations in my life. I thank my siblings Samira, Sajad, and Sajede Rasouli for always being there for me. I would also like to thank my friend, Hoda Hashemi, for being like my sister, thousands of miles away from my family. Finally, I thank my husband, my best friend and the love of my life, Dr. Volkmar Frinken for being always supportive, for accompanying me during the long nights and weekends on the microscope, and for all his help and sacrifices he made during my graduate school experience.

Degradation Mechanisms of Pt and Pt Alloy Nanocatalysts in Proton Exchange Membrane Fuel Cells

SomayeSadat Rasouli Ph.D.

The University of Texas at Austin, 2017

Supervisors: Paulo J. Ferreira

The goal of this PhD research is to fundamentally understand the degradation mechanisms and durability issues of Pt and Pt-alloy nanocatalysts in the cathode of proton exchange membrane fuel cells (PEMFCs). The primary tool for this research has been state-of-the-art transmission electron microscopy, including aberration-corrected TEM/STEM, in-situ TEM heating, 3D tomography, and Energy Dispersive Spectroscopy (EDS).

In order to reveal the degradation mechanisms of nanocatalysts, both indirect and direct TEM methods were used. In the first part of this research, we performed post-mortem transmission electron microscopy (TEM) on the membrane electrode assembly (MEA) of PEMFCs. Using a thorough composition and morphological analysis of the catalysts after fuel cell cycling, we showed that the mechanisms proposed in the literature do not fully explain the degradation of the nanocatalysts. Accordingly, new mechanisms were proposed, namely: 1- Modified Ostwald ripening until adjacent particles make contact with each other and coalesce, 2-preferential deposition of single atoms and atomic clusters between two or more particles and consequently bridging between them.

To evaluate these proposed mechanisms mentioned above, the second part of this work focused on determining the behavior of Pt and Pt-alloy nanoparticles during different stages of fuel cell cycling. The first challenge was to find a way to ensure that I was observing the exact same nanoparticles during the various stages of cycling. To accomplish this, we developed an experimental setup which replicates on a TEM grid the effect of voltage cycling on the cathode of an MEA. Using this approach, it was possible to track the behavior of a single nanoparticle at different stages of voltage cycling on the nano-atomic scale. Through these direct observations, we demonstrated that due to carbon corrosion the defects appear at the carbon/nanoparticle interface, which in turn result in particle migration and consequently coalescence. We also revealed the mass transfer mechanisms during the coalescence of nanoparticles. In addition, we revisited the commonly held view on the mechanism of particle dissolution and deposition. Thus, during the later stages of cycling, when the concentration of dissoluble Pt reaches a critical amount, single atoms and atomic clusters appear on the carbon support, which consequently move toward other particles and re-deposit on their surface. This dissolution happens preferentially at the corners and steps of the nanoparticle, while re-deposition occurs on {111} type planes. Contrary to the literature, it turned out that re-deposition is not necessarily an isotropic process as atomic clusters can deposit between two or more particles and bridge them.

Furthermore, we investigated the atomic surface evolution and phase segregation of Pt_3Co and PtNi nanoparticles under the effect of voltage through advanced spectroscopy technique such as EDS. While it is generally accepted in the literature that larger particles grow at the expense of smaller ones, this study showed that in case of alloys, deposition of Pt occurs on the surface of smaller particles rather than larger ones. This is due to the thicker Pt rich surfaces on the smaller particles, since the Pt rich surface act as nucleation sites for re-precipitation of Pt.

TABLE OF CONTENTS

CHAPTER 3: EXPERIMENTAL METHODS 46

LIST OF FIGURES

Chapter 1: Introduction

1.1 Motivation

A thorough knowledge of the atomic structure and composition of electrocatalyst nanoparticles is paramount to the development of advanced materials for proton exchange membrane fuel cells (PEMFC), one of the most promising energy conversion devices for automotive and stationary applications. The efficiency of the fuel cells is largely restricted by two main challenges: 1) the slow oxygen reduction reaction (ORR) kinetics catalyzed by platinum (Pt) based nanocatalysts in the cathode and 2) the instability of the nanocatalyst particles during fuel cell operation. Pt nanoparticles (NP) are currently used as the catalyst to promote the kinetics of hydrogen oxidation and ORR in the anode and cathode of the fuel cell, respectively. However, Pt-based alloys have being investigated to replace Pt on the cathode as a way to improve the efficiency of the fuel cell and reduce cost [1]–[5]. Although the enhancement in the ORR activity of Pt alloys is well established, the durability of the catalysts remains the main issue for their commercialization.

Due to their large surface area-to-volume ratio, Pt and Pt-alloy NPs have a strong tendency to grow in size over short time scales, which can lead to significant changes in their desirable properties with subsequent changes in the behavior and performance of PEMFC. In particular, the growth of the Pt-based NPs catalysts is responsible for a reduction in their electrochemically active surface area, which leads to an undesired catalyst deactivation and subsequent reduction in cell performance after several cycles [6]–[8]. Thus, it is critical to understand the fundamentals behind catalyst instability, to be able to develop more fruitful strategies towards preventing catalyst activity loss.

Ferreira et al proposed four mechanisms describing the loss of electrochemical active surface area of Pt NPs in the cathode of the PEMFC during cycling operation, namely 1) dissolution and re-deposition of Pt on large particles on the nanometer scale or Ostwald ripening, 2) particle migration on the carbon support and coalescence, 3) particle detachment from carbon support, and 4) particle dissolution and re-precipitation on the ionomer phase or/and membrane by chemical reduction of soluble Pt with permeated hydrogen from the anode side [7]. Many studies, including post mortem transmission electron microscopy (TEM) studies have been performed to address the mechanisms of catalyst degradation [6], [7], [9]–[14]. In these studies, a batch of randomly selected NPs were characterized before cycling and then compared to another batch of randomly selected NPs in the cathode of the membrane electrode assembly (MEA) after voltage cycling.

Moreover, the effect of alloying on the degradation mechanism and loss of active surface area of Pt-alloy nanocatalysts has also been investigated. Dubau et al have studied the decay characteristic of Pt_3Co alloy in a 16 cells –stack, showing a continuous dissolution of Co in the ionomer phase during operation, which resulted in a core shell structure with a Pt enriched surface [13]. In a different body of work, Chen et al. identified the increased thickness of Pt-enriched surface layer as the main factor responsible for the degradation of acid-treated PtxCo catalyst after potential cycling [11].

Although several issues have been addressed in the aforementioned studies, it is still unclear what is the dominant degradation mechanism, particularly because direct evidence of each mechanism is not available and thus a fundamental understanding of particle behavior in real time, at different stages of fuel cell cycling, is still challenging. Furthermore, when using Pt-alloy NPs, such as Pt-Ni or Pt-Co, we expect that new factors, such as heterogeneous dissolution of the elements during voltage cycling and enthalpy of mixing of the elements, might affect the mechanisms of loss of specific activity and the active surface area of the nanoparticles during fuel cell operation. So it is not clear yet what parameters control the degradation in alloy nanocatalysts and whether the four abovementioned mechanisms can fully explain the coalescence of alloy NPs.

As a consequence various key questions remain unanswered, namely: 1) Is modified Ostwald ripening or coalescence the main mechanism for particle growth within the cathode? 2) How does voltage cycling affect particle movement on the carbon support and consequently the coalescence of particles? 3) How does carbon degradation during voltage cycling affect the coalescence of particles? 4) How does alloying influence the degradation mechanism?

1.2 Approach

In the first part of this work, post-mortem parametric TEM studies will be performed on Pt_3Co nanocatalysts supported on amorphous carbon and present on the cathode side of the membrane electrode assembly. In the parametric study, particle growth will be monitored after 10K voltage cycling under different operating conditions, namely low humidity, high temperature and high voltage. Each of these conditions affect one of the possible coarsening mechanisms. High potential and low humidity conditions are extreme conditions that impact the Pt dissolution kinetics and migration in the ionomer phase, which affect modified Ostwald ripening and particle precipitation in the membrane, while high temperature will facilitate the Brownian motion of the NPs on the carbon support which influence particle movement and coalescence. In addition, considering the fact that due to the low Co/Co^{2+} redox potential and low enthalpy of mixing of Pt-Co, re-deposition of Co ions on the particles is not thermodynamically favorable, the parametric study of Pt3Co nanocatalysts allows us to track the dissolution and re-deposition process by compositional analysis of the nanoparticles before and after voltage cycling. Thus, this parametric study provides an insight into the dominant mechanism of electrochemical active surface area loss and helps us realize whether the four proposed mechanisms can explain the growth of alloyed NPs or new mechanisms should be considered.

To understand the details about each mechanism, the second part of this thesis will be focused on analyzing the behavior of Pt and Pt alloy NPs at different stages of fuel cell cycling, for which the best way would be performing in-situ voltage cycling of the MEAs inside the TEM. However, operating a fuel cell inside the microscope is extremely challenging, considering the simultaneous presence of hydrogen and oxygen (or nitrogen) on the anode and cathode side of the MEA inside the microscope. So the closest approach to an in-situ experiment will be used herein. For this purpose a set-up was developed to simulate the effect of voltage cycling on the cathode side of the fuel cell outside of the microscope. In this set up, catalysts NPs supported on carbon are deposited on gold TEM grids attached to a gold plate, which are used as a working electrode in a three electrode electrochemical cell. The TEM grids are cycled in N2 saturated 0.1 HClO4 liquid electrolyte for a different number of cycles. In this fashion, pre-defined locations of the electrocatalyst on the TEM grid are analyzed before and after cycling using aberration corrected TEM imaging. Performing this experiment on Pt NPs supported on carbon black and carbon nanotubes (CNTs) can provide direct evidence for the degradation mechanisms of Pt NPs, as well as information on the effect of voltage cycling and the type of carbon substrate on the behavior of NPs. They can also verify whether an applied voltage results in particle movement on the carbon support and how single atoms and atomic clusters play a role on particle coalescence. By performing the same experiment on Pt3Co and PtNi nanocatalysts and comparing the atomic structure and composition within identical individual NPs before and after voltage cycling, the effect of alloying on the degradation mechanism will be investigated.

1.3 Objectives and Main Contributions

1.3.1 Objectives

To address the aforementioned issues, the primary objective of this work is to fundamentally understand the dominant mechanisms that influence the loss of electrochemically active surface area of Pt and Pt-alloy nanocatalysts in the cathode of PEMFC. In particular, the objectives of this dissertation are as follows:

1- Determine whether modified Ostwald ripening, or particle movement and coalescence, dominate particle growth within the cathode of a PEMFC.

2- In case of coalescence, determine whether and how the applied voltage can lead to particle movement and consequently coalescence and understand the effect of the type of carbon support.

3- In case of Ostwald ripening, understand the mechanism of atomic deposition on the particles and determine if single atoms deposit homogenously on the surface of particles and/or atomic clusters form between the particles and consequently bridge them.

4- Understand the degradation mechanism of Pt alloy nanocatalysts and determine how voltage cycling affects the atomic structure and composition distribution of Pt-alloyed catalysts, which in turn influence the degradation mechanism of the cathode in the fuel cell.

1.3.2 Main Contributions

The main contributions of this dissertation are as follows:

1. Transmission electron microscopy characterization of Pt_3Co nanocatalysts on the cathode side of the MEA, after potential cycling under different operation conditions, namely baseline, low humidity, high voltage and high temperature. In this fashion, the mean particle size, particle loss from the cathode, particle

precipitation in the membrane, and chemical/morphological analysis throughout the cathode was obtained to address the dominant degradation mechanism.

2. Development of an experimental set up to determine the behavior of Pt NPs before and after various stages of potential cycling. This is achieved by replicating on a TEM grid the effect of potential cycling on the cathode of a fuel cell in a three electrode electrochemical cell in the presence of liquid electrolyte. Using this approach, it is possible, for the first time, to track the behavior of a single nanoparticle during voltage cycling on the atomic scale. Pt NPs supported on carbon nanotubes are used for this part due to their simpler 2-D morphology compared to the more complex 3-D structure of carbon black. However, Pt NPs supported on carbon black are also investigated using this approach. The TEM observations are performed using phase contrast imaging in aberration corrected instruments operated at 200 KV and 80 KV providing sub-Angstrom resolution and thus allows single atomic columns to be clearly identified within each NP.

3. Revealing the surface area loss mechanisms, surface evolution and phase segregation of Pt alloys such as PtNi and Pt_3Co NPs supported on amorphous carbon during electrochemical potential cycling, using aberration corrected scanning transmission electron microscopy (STEM) and energy dispersive spectroscopy (EDS).

1.4 Organization of the Dissertation

The dissertation is organized as follows:

In chapter 2, the current state of understanding is presented. The chapter starts with an introduction to the fuel cells and their basic theoretical background. Thereafter, proton exchange membrane fuel cells and their components, specifically the catalyst layer and its requirements and challenges are explained. The catalyst degradation and different methods of electrocatalysts testing are then discussed. The mechanisms of nanocatalysts surface area loss, theoretical analysis of nanoparticle coalescence, and degradation mechanisms of Pt-alloy nanocatalysts are also discussed. At the end, the recent studies on the effect of operating conditions on fuel cell degradation are explained. In summary, this chapter focuses on findings from the literature related to the durability of catalyst layer in proton exchange membrane fuel cells.

In chapter 3, the general experimental methods used for this work are presented. In particular, single cell evaluation test, cyclic voltammetry, and determination of electrochemically active surface area are explained. Subsequently, scanning/transmission electron microscopy, which was extensively used in this work, is presented. At the end, the identical location transmission electron microscopy is introduced and explained in detail.

Chapter 4 presents the post mortem TEM study of the cathode and membrane of MEAs after fuel cell potential cycling under different operating conditions. Through this study, the dominant degradation mechanisms are revealed and new surface area loss mechanisms are proposed and validated.

The focus of chapter 5 is on determining the behavior of Pt NPs at various stages of fuel cell cycling with the purpose of understanding and obtaining direct evidence about the degradation mechanisms. For this purpose the results of identical location TEM studies on Pt nanoparticles supported on carbon nanotubes and amorphous carbon are presented and analyzed. Subsequently the fundamentals behind particle movement and coalescence and particle dissolution and re-deposition are discussed.

In Chapter 6, the effect of alloying on the degradation of nanocatalysts is studied. For this purpose, the results of identical location STEM studies on Pt alloy nanocatalysts, such as Pt-Ni and Pt-Co are discussed. Subsequently, the surface evolution and composition distribution of the alloyed nanocatalysts before and after potential cycling is analyzed.

Lastly, chapter 7 presents the final conclusions from this study and provides some recommendations for future work.

Chapter 2: State of Understanding

2.1 Introduction

The demand for renewable energy is globally on the rise, while the concern toward pollution and potentially hazardous forms of power generation is increasing. To reduce our dependence on oil as the primary transportation fuel source, and to address environmental concerns associated with the use of fossil energy carriers, the development of clean, secure, and sustainable energy is becoming increasingly important. Compared to other energy generation technologies such as reciprocating engines and gas turbines, fuel cells are efficient and generate virtually no pollution such as nitrogen oxide (NOx), sulfur oxide (SO_x), or particulate matter (PM10), while dramatically reduce carbon dioxide (CO_2). In addition, with availability ratings better than 90%, fuel cells are not hampered by external influences such as time of day or weather that affect other environmentally-friendly technologies, such as wind turbines and solar power.

2.2 Principles of Fuel Cells

In the most basic description, fuel cell is an electrochemical cell that has reactants supplied from an external source. This electrochemical cell consists of two electrodes, an anode, a cathode, and an ion-conducting electrolyte. The reactants (oxidant and reductant, normally referred to as the fuel) are supplied to the electrodes and then react chemically to produce electrical energy. This can be distinguished from a battery, which is also an electrochemical cell, but the reactants are contained inside the cell [15]–[17]. In the case of a battery, once the reactants are consumed during the energy producing reaction, the battery must either be recharged (by connecting to an external electrical energy source) or replaced. In contrast, a fuel cell will operate continuously as long as reactants are supplied externally, or the fuel cell will degrade or fail. In other word, fuel cells can also be considered as energy-converting devices, converting chemical energy into electrical energy. There are different types of fuel cells based on the electrolyte used, namely; (i) proton exchange membrane fuel cells (PEMFC), (ii) alkaline fuel cells (AFC), (iii) phosphoric acid fuel cells (PAFC), (iv) molten carbonate fuel cells (MCFC), and (v) solid-oxide fuel cells (SOFC). While all types of fuel cells work based on similar electrochemical principles, their operating temperature range, type of fuel and oxidant, catalyst materials and performance characteristics differ from each other [15], [18], [19]. Among all types, PEMFCs appear uniquely suited for portable and transportation applications due to their high energy/power density and low operating temperature.

The overall reaction of a PEM fuel cell is based on the combustion reaction of oxygen and hydrogen, but by separating the half reactions, the chemical energy stored in the reactants can be converted to electrical energy. Hydrogen oxidation reaction (HOR) occurs in the anode, which produces protons and electrons. The protons and electrons are transported to the cathode through the membrane and the external circuit, respectively. Inside the cathode, oxygen reduction reaction (ORR) occurs where oxygen reacts with the protons and electrons to produce water and heat. The electrons traveling through the external circuit produce a current or electrical energy[15]–[17]. Figure 2-1 shows a basic illustration of a fuel cell operation. The electrochemical reactions in a PEM fuel cell can be expressed as follows:

Anode reaction: $2H_2 \rightarrow 4H^+ + 4e^-$ (2.1)

Cathode reaction: $O_2 + 4H^+ + 4e^- \rightarrow 2H_2O$ (2.2)

Overall reaction: $2 H_2 + O_2 \rightarrow 2H_2O$ (2.3)

2.2.1 PEM Fuel Cell Components

The main part of a fuel cell is a membrane electrode assembly (MEA) which consist of anode gas diffusion layer (GDL), anode catalyst layer (CL), proton exchange membrane (PEM), cathode CL, cathode GDL, as shown in Figure 2-2.

The gas diffusion layer (electrode backing) is placed in contact with the catalytic active layer. The GDL is usually prepared by depositing a mixture of carbon powder and polytetrafluoroethylene (PTFE) onto a carbon paper or carbon cloth. The carbon materials provide electronic conductivity for the GDL, while the PTFE helps to adjust the hydrophobicity of the GDL, ensuring fast liquid and gas transfer during cell operation [16]. Oxygen reduction and Hydrogen oxidation reactions take place at the catalytic active layers which are attached to either side of the membrane. Noble metals or noble metal alloys are used in the CL of PEMFC.

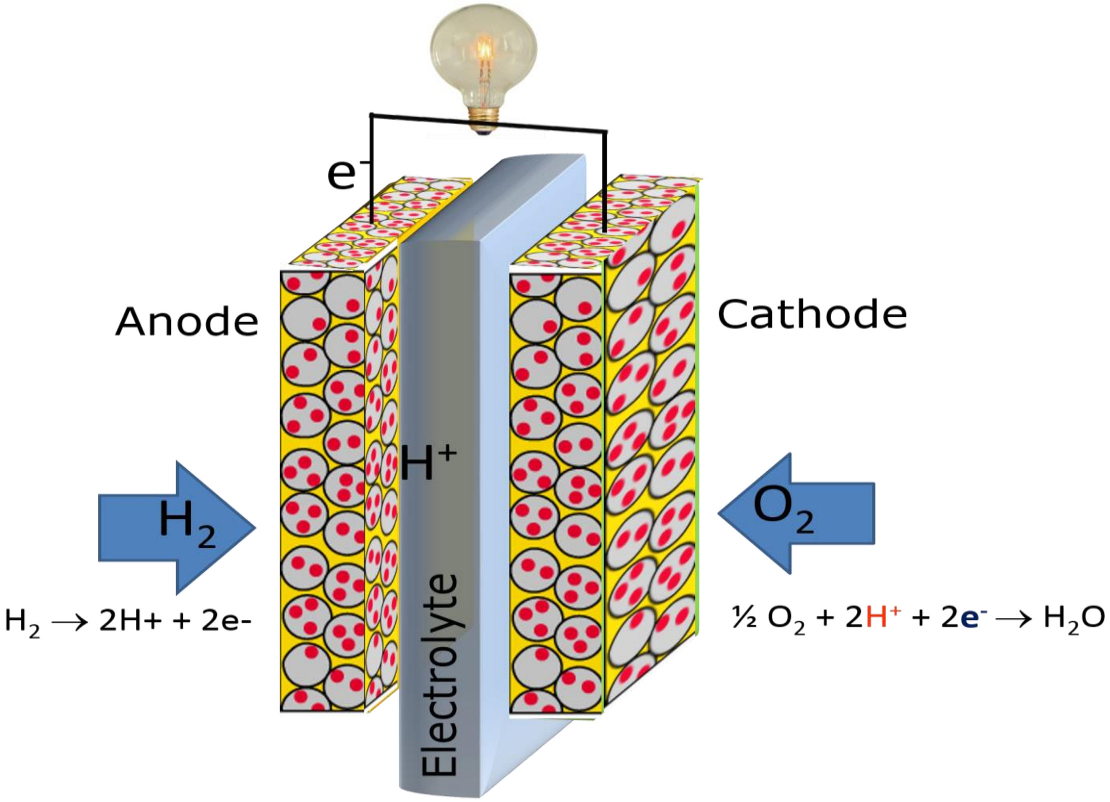

Figure 2-1 Basic illustration on a fuel cell operation

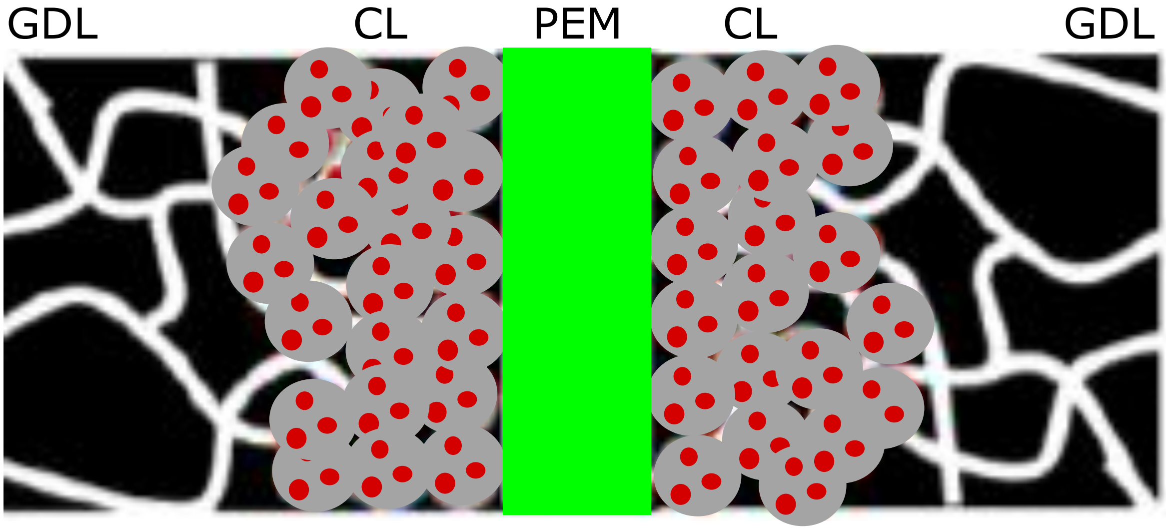

Figure 2-2 Schematic of a PEM fuel cell component

The heart of the PEM fuel cell is the proton exchange membrane, which serves as a pathway for the protons to be transferred from the anode to the cathode. In addition, the membrane also separate the fuel and oxidant gas phases and electronically insulates the cathode from the anode. Nafion, which is a sulfonated perfluorinated polymer is currently the commercially available membrane. The sulfonic acid (SO_3H) groups on the side chains of this polymer allow the protons or other cations to hop from one acid site to another, in the presence of water [20], [21].

2.3 Electrocatalysts

As HOR and ORR kinetics are too sluggish, catalysts are required to promote the reactions to happen at a proper rate. The cathode and anode catalytic active layers are placed on either side of the membrane. Three interfaces are required for the catalyst sites to be electrochemically active: (i) Pt catalyst surface, electrically connected to the external path to provide electron transport paths; (ii) ionomer or electrolyte contact to transport protons; and (iii) reactant gas phase access [16]. Typically, Pt or Pt alloy nanoparticles supported on carbon are used as the electrocatalysts for PEMFC. The carbon support ensures electron conductivity throughout the whole electroactive layer. It also provides the highest possible catalyst dispersion and electroactive catalyst surface [22]. Usually, liquid Nafion, which is the ionomer phase, is impregnated into the catalyst layer to provide an ion transport path for the protons inside the anode and cathode. The porous system enables the gas to access the electrocatalyst surfaces and provides a path for the removal of the byproduct water from the electrode.

2.4 Approaches for Less Expensive Catalysts

2.4.1 Pt Alloy Catalysts

Alloying Pt with less noble elements has been considered to increase the oxygen reduction activity in phosphoric acid fuel cells since 1970 [23]. In 1990s, when PEMFCs became more popular, various binary Pt-M (M = Ni, Cr, Co) ordered structure alloys have been discovered to show 2-5 times enhanced catalytic activity for ORR in PEMFC [2], [5], [24], [25]. To understand the reasons behind the catalysts activity enhancement in Pt alloys, different approaches, including modeling the catalyst surfaces and atomic structure were used. Using these approaches made it possible to predict new surfaces that show even greater activity for oxygen reduction reactions. Ross and Markovic characterized the surfaces of a series of bulk Pt_3M (M = V, Ti, Fe, Co, Ni) polycrystalline alloys by surface techniques [5]. They found a strong correlation between the composition of the surface and their post-treatment after synthesis. They showed that the samples that had been annealed in vacuum had Pt-rich skin due to the segregation of Pt to the surfaces, while the composition of the surfaces sputtered with Ar was similar to the bulk. This segregation has been predicted by density functional theory (DFT) calculations of Pt alloys by Norskov’s group [26]. The Pt-rich surfaces over PtFe and PtCo showed the most active catalyst in diluted acid environment. A shift of the d-band center of Pt was found to be responsible for the enhancement in the catalytic activity as measured using ultra-violet photoelectron spectroscopy (UPS). As a result of the shift in the d-band center, the bonding between Pt and OH groups on the surface of the catalyst becomes weaker, which in turn results in a reduction in OH coverage. This will lead to a greater number of sites to be available for oxygen adsorption, dissociation, and reduction. In a different paper, Markovich et al. measured the Pt_3Ni activity of low index planes, showing an activity ranking of (100) < (110) << (111). The activity enhancement was attributed to a large shift in the d-band center [27].

Norskov's research group has shown that the strength of the catalyst-oxygen bond is found to be a key factor predicting the ORR activity of the catalyst resulting in a volcano plot (see Figure 2-3) [28]. Alloy compositions with intermediate metal-oxygen binding energy have the highest activity due to the slow removal of adsorbed O and OH species. Higher O binding energies results in a decrease in the activity due to the slow removal of adsorbed O and OH species; whereas lower O binding energies lead to low O_2 dissociation rates and protonation of absorbed O_2, which also decreases the catalytic activity [26], [29]–[31].

In a different work, it has been shown that the ORR activity of Pt alloys can be increased by 2-10 times relative to that of pure Pt by developing Pt-rich surfaces via acid leaching of less noble alloying elements and high temperature annealing [27], [32]–[37]. Recently, Patrick et al. used aberration corrected scanning transmission electron microscopy (STEM) to analyze the atomic structure of acid leached and high temperature annealed Pt_3Co nanoparticles [36] They showed that acid leached particles exhibited a solid solution structure with heterogeneous composition, while annealed Pt_3Co particles showed three atomic layers rich in Pt on the surface.

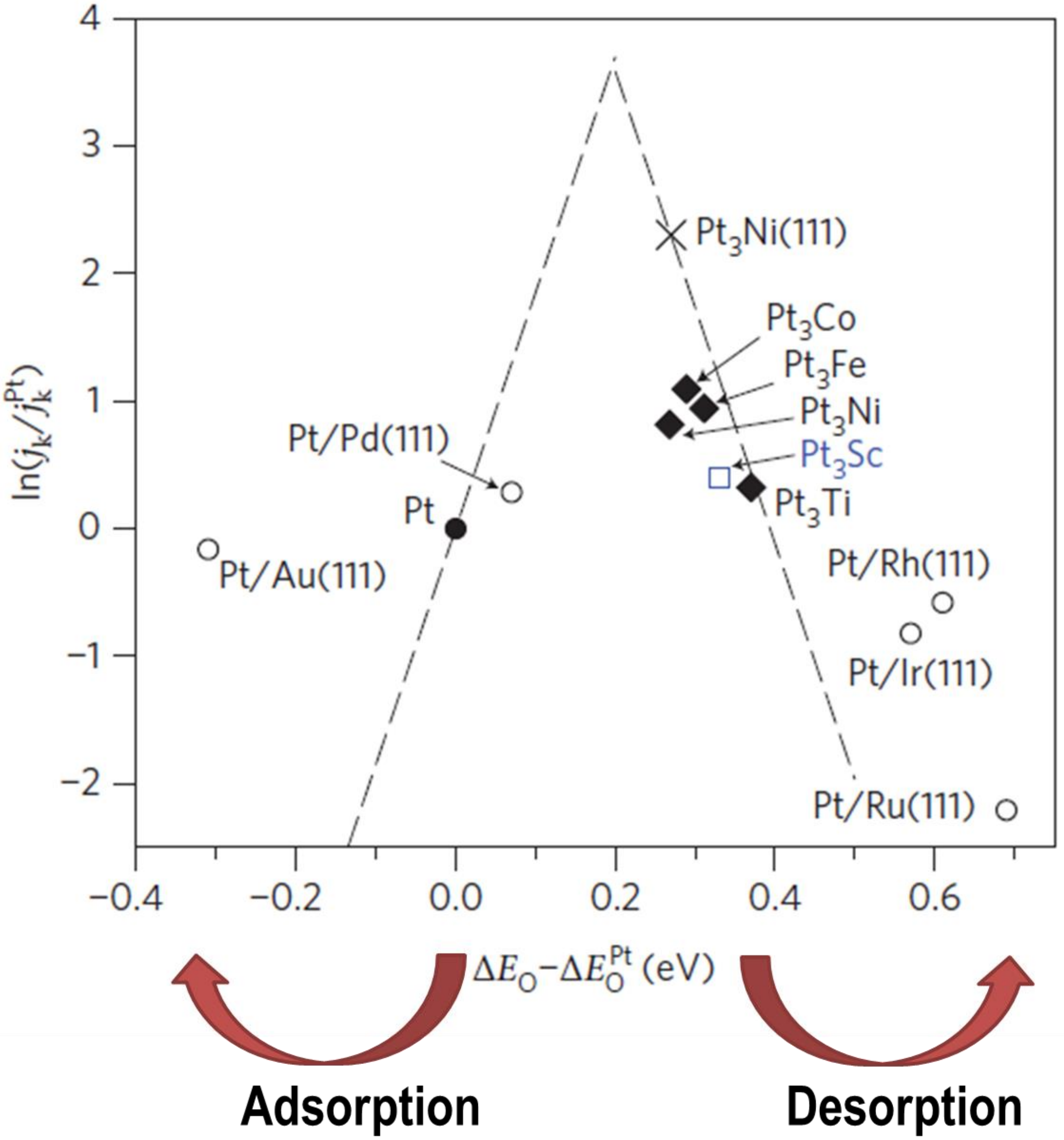

Figure 2-3 Trends in oxygen reduction activity of bulk Pt and Pt3M as a function of oxygen binding energy

2.4.2 Pt Core-Shell Catalysts

As discussed above, the increased activity of Pt alloy is related to changes in the Pt–Pt bond distance at the surface of the catalysts and the ligand effect of the near surface structure, which results in a shift in the d-band center of Pt. The significant effect of the surface composition and the near surface structure on the catalytic performance lead to a large interest in developing a heterogeneous core-shell structure for the catalyst materials. Alloying Pt with less noble elements in a core-shell structure, not only increase the ORR activity due to the electronic interaction of the Pt surface atoms with the underlying elements, but also reduce the cost considerably by the use of a low cost element in the core. In addition, the less noble metal in the core will be protected from dissolution, by the Pt shell on the surface of the catalyst.

Different approaches have been used to achieve this unique structure. One of these approaches that has been pioneered by the group of Adzic at Brookhaven National Laboratory is the galvanic displacement of the surface element [30], [31], [38], [39]. This approach argues that Pt only needs to be at the surface because only surfaces of nanoparticles actually participate in the catalysis. Following this strategy, Pt monolayers were deposited onto non-Pt substrates using galvanic displacement of copper electrodeposits with platinum (Figure 2-4a). The resulting catalysts have shown very high intrinsic surface electrocatalytic activity for ORR, with a double-digit Pt-mass based activity gain.

Koh and Strasser [40], [41] and Srivastava et al. [42] have reported an alternative approach to achieve core-shell structures. They prepared a series of carbon supported Pt

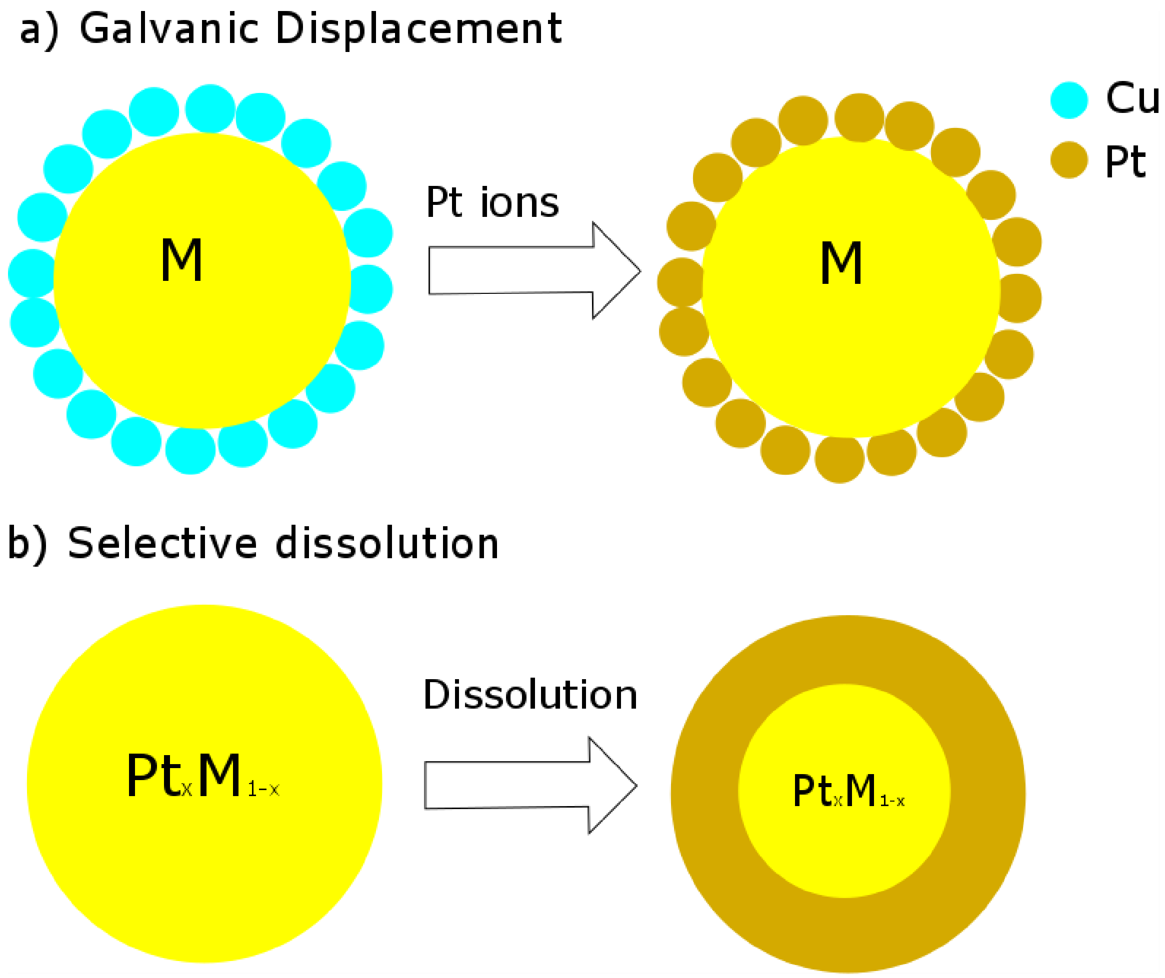

Figure 2-4 Surface modification through a) galvanic displacement, and b) selective dissolution

alloys with high concentration of transition metal (>> 50 atomic %) and then electrochemically leached out the transition metal from the surface by electrochemical cycling until 1.2 V vs RHE in an acid environment (Figure2-4b). Using this approach, the majority of the transition metal was dissolved into the electrolyte, presumably producing multilayer thick Pt-rich shell on the surface of an alloy cores with reduced transition-metal content. The leached catalysts were found to have oxygen reduction activities significantly higher than Pt. In particular, $Pt_{25}Cu_{75}$ catalysts exposed to leaching in an acid environment showed mass activities up to five times higher than that of of Pt. Characterization of the leached catalysts showed that much of the Cu was removed during the leaching, leaving a pseudo core-shell structure with a PtCu alloy core surrounded by a skeletal Pt shell.

2.5 Cathode degradation

The durability of the fuel cell remains a main challenge in fuel cell commercialization. Achieving the DOE lifetime goal of 5000 hours requires a fundamental understanding of the degradation mechanisms. Cathode degradation is the main contributor to the fuel cell performance degradation. Many studies in the past several years have related the cathode degradation to the morphological changes of nanocatalysts and claimed that the main cause of PEMFC degradation is the loss of electrochemically active surface area (ECA) of the nanocatalysts in the cathode.

2.5.1 Cathode Degradation Testing

In order to assess the degradation of fuel cell components including the electrocatalysts, several accelerated stress test (AST) protocols have been previously developed [14], [43], [44]. These ASTs can be performed either ex situ in a classical three-electrode electrochemical cell using liquid electrolytes (half-cell) [14], [43], [45], [46], or in situ in PEMFCs (single-cell). In the first technique, the electrocatalyst material is evaluated as a thin layer on a bulk electrode (e.g., glassy carbon) in dilute liquid electrolyte (e.g., H_2SO_4) either as a static electrode or an RDE. There has been a lot of discussion on the most appropriate electrolyte to use. In general, dilute perchloric acid (HClO4) is preferred, as it is the closest to the perfluorosulfonic acid ionomer (typically Nafion) used in the catalyst layer of a PEM fuel cell, due to its noncoordinating nature. Trifluoromethylsulfonic acid (CF_3SO_3H) can be used as an alternative as it mimics perfluorosulfonic acids closely, but there are relatively few studies with this acid [47].

The second approach is to test catalysts as layers in full MEA structures. This has the advantage of testing catalysts under realistic conditions and in realistic environments. Although the durability test in PEMFCs provides an invaluable insight into the degradation of the fuel cells, it is difficult to separate the contribution of other components such as membrane and gas diffusion layer. ASTs in three-electrode electrochemical cells have the advantage of being less expensive and allow the ability to provide controlled information on the degradation of the catalytic layer excluding any contribution from other parts of the PEMFC. In fact, several studies have shown a good agreement between the ECA loss mechanisms and half-cell durability tests [48], [49].

2.5.2 Mechanisms of Catalyst Surface Area Loss

Electrochemically active surface area (ECA) is defined as the total Pt surface area that electrochemically contributes to the ORR divided by the total mass of Pt, and has the units of m^2/gpt. Since the ORR reactions occurs on the surface of the nanocatalysts, larger ECA indicates more catalyst sites available for the reactions to happen. This consequently results in higher efficiency of the fuel cell. According to the definition of ECA, it has inverse proportionality with particle size. For example, considering a spherical particle with diameter d, the ratio of surface area to total mass leads to a scalar multiplied by 1/d. Moreover, the nanocatalysts are considered active in the electrochemical reactions only when they are in contact with the carbon support, which serves as the electronic conducting phase in the cathode. Therefore, the ECA loss could result from a loss in mass of the catalysts or an increase in particle size. Mass loss from the carbon support occurs through two mechanisms, namely detachment from the carbon support and dissolution and re-precipitation (D&R) in the ion conductive phase (either ionomer in the catalyst layer or membrane). Regarding particle growth, two mechanisms are known, namely particle migration and coalescence, as well as modified electrochemical Ostwald ripening (MEOR). These four abovementioned mechanisms are affected by various parameters such as initial particle size, operation conditions and synthesis process.

2.5.2.1 Detachment from the carbon support

Nanocatalyst detachment from carbon support could also lead to ECA loss due to the fact that Pt particles can only contribute to the ORR when they are in contact with the carbon support, as illustrated in Figure 2-5. The primary cause of detachment from the carbon support is carbon corrosion, which is commonly observed in a electrochemical system. Once this happens, particles may fall off the carbon and thus would not contribute to the ORR. The electrochemical oxidation of carbon is thermodynamically possible above 0.2 V, according to Eastwood et al. [50]. Moreover, Willsau et al. [51] have demonstrated that under the presence of Pt, the reaction between carbon and oxygen will lead to the formation of CO and vacancies on the carbon support when the potential is higher than 0.3V vs RHE, and the CO could be further oxidized to CO_2 at potentials between 0.6V to 0.8V vs RHE. These reactions results in the shrinkage of carbon support and lead the Pt particles to lose their contact with carbon support, which is the electron conductive phase. This in turn will decrease the ECA of the nanocatalysts in the cathode of the PEMFC. The rate of carbon corrosion is influenced by many factors, such as catalyst loading, potential and temperature. Stevens et al. [52] have demonstrated that under PEMFC conditions, the rate of carbon corrosion increases with increasing Pt loading in the cathode, which is due to an increase in interfacial area between Pt and the carbon support, as well as the fact that Pt nanoparticles also catalyzes carbon corrosion and ORR. Moreover, they also reported that the increasing temperature increases the rate of carbon corrosion [52]. Stevens et al. [53] have also shown that in addition to Pt loading and temperature, the carbon corrosion is also affected by the surface chemistry of carbon support. They reported that graphitized carbon support with the same surface area and Pt loadings showed better stability than ungraphitized carbon support.

2.5.2.2 Dissolution and re-precipitation (D&R) in the ion conductor

Particle dissolution and re-precipitation mechanism involves three steps: dissolution of Pt from the particles into Pt ions, diffusion of Pt ions in the ionomer and finally re-precipitation of Pt ions in the ionomer phase by crossover hydrogen from the anode side (Figure 2-6). The Pt particles can be precipitated either on the ionomer phase inside the cathode or on the membrane. Yasuda et al. [54] showed the formation of Pt single crystals ranging from 10nm-100nm inside the membrane after potential cycling of the PEMFC. Guilminot et al. [55] demonstrated that the mass distribution of the precipitated Pt particles in the membrane differs across the membrane based on the distance to the cathode, i.e. the particles closer to the cathode are larger than the ones far from the cathode. In order to investigate if the electron beam in SEM and TEM affect the electrochemical reduction of Pt ions to Pt single crystals, ultraviolet (UV) spectroscopy was used and confirmed that the precipitated particles were formed during potential cycling of the MEAs [56]. Moreover, according to Zhang et al. [57] hydrogen and oxygen partial pressures in the fuel cell indicate the position of the re-precipitated particles inside the membrane. They showed that the distance of the Pt band in the membrane decreases as the hydrogen partial pressure increases.

Ferreira et al. [9] have demonstrated that there are different morphologies of the particles precipitated in the membrane such as dendritic shapes, truncated octahedra, truncated cuboids and truncated tetrahedra, based on the homogeneity of the driving force. The driving force for re-precipitation is the supersaturation of Pt ions. The balance between the surface energy and interfacial kinetics of Pt ion reduction controls the shape of the

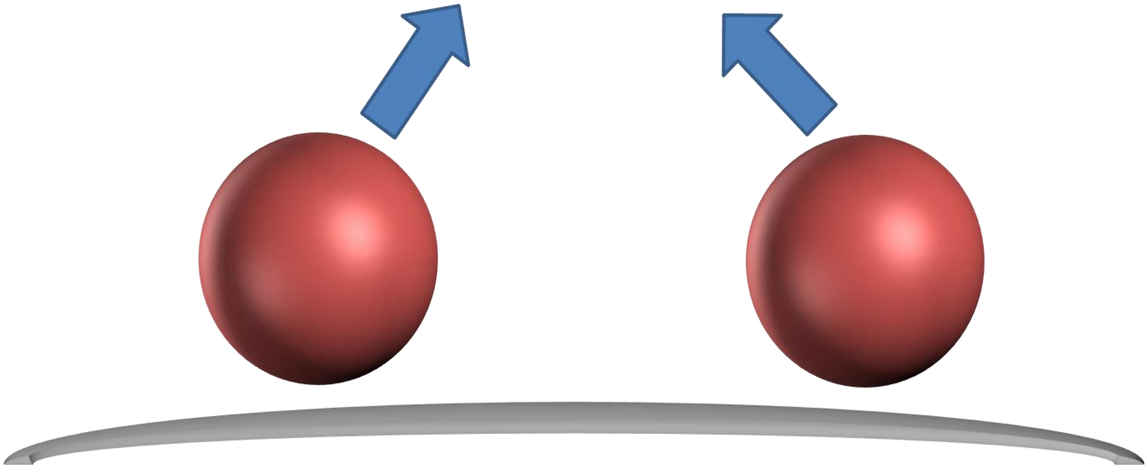

Figure 2-5 Schematic of particle detachment from carbon support

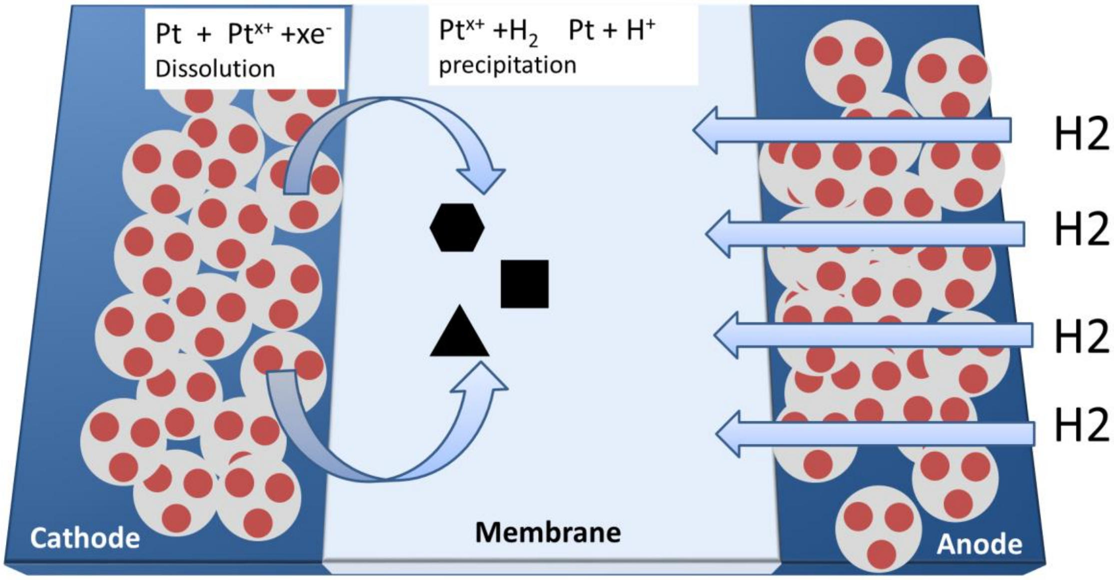

Figure 2-6 Schematic of particle dissolution and re-precipitation (D&R) mechanism.

precipitated particles. The formation of dendritic particles is due to the fact that the interfacial kinetics for reduction of Pt^{x+} ions on the growing surface is fast when comparing to the diffusion of Pt ions to the surface of the dendritic particles. On the other hand, the formation of faceted Pt particles in the cathode-membrane area is due to the fact that the diffusion of Pt ions is faster than the interfacial kinetics of Pt re-deposition. Shao-Horn et al. [6] showed that these particles not only appear in the membrane but also in the ionomer phase where no carbon was observed. The amount of precipitation inside the cathode increases in the areas closer to the cathode/membrane interface. This could be explained by the higher pressure of crossover hydrogen in the cathode/membrane interface than in the middle of the cathode area. The precipitated particles, both dendritic and faceted morphology either inside the cathode on the ionomer phase or in the membrane are single crystals, as confirmed by the TEM electron diffraction [6].

2.5.2.3 Modified Electrochemical Ostwald Ripening

According to Guilminot [55], the Ostwald Ripening process in fuel cells could be classified into two categories, namely 2D Ostwald Ripening and 3D Ostwald Ripening (modified electrochemical Ostwald Ripening (MEOR)). While 2D Ostwald ripening defines simply as the transport of single atoms from smaller particles to larger ones, 3D Ostwald ripening, as illustrated in Figure 2-7, involves three steps including 1- electrochemical oxidation of Pt in the small particles to form Pt ions, 2- diffusion of Pt ions into the ionomer phase, and 3- re-deposition of ions onto larger particles through electrochemical reduction. The modified Ostwald ripening is known to play a significant role in surface area loss and is thus more widely studied.

Different mechanisms have been proposed for Pt dissolution. According to Gasteiger et al.[58], increasing the potential to the Pt oxide region during anodic voltage sweep results in the formation of Pt oxide surface layers, which would in turn lead to the oxidation of Pt to Pt ions. While Darling et al. [59] proposed that a pure chemical reaction (2.4) results in the Pt dissolution, Johnson et al [60] believes that electrochemical reduction reaction of PtO_2 (2.5) will lead to the formation of Pt ions during the anodic potential sweep. PtO_2 in reaction (2.5) arises from the oxidation of Pt surface layers.

$$PtO + 2H^+ \longrightarrow Pt^{2+} + H_2O \tag{2.4}$$

$$PtO_2 + 4H^+ + 2e \longrightarrow Pt^{2+} + 2H_2O \tag{2.5}$$

As discussed above, the reason for the dissolution process is not fully understood. It could be a pure electrochemical process or a mix of chemical and electrochemical processes. If it is an electrochemical process, the dissolution rate should be significantly influenced by the potential. If it is a combination of chemical and electrochemical processes, the dissolution rate should be determined by conditions other than potential, such as temperature or humidity [61]. Uchimura et al. [62] have reported that the dissolution of Pt to Pt ions could be accelerated by increasing the upper potential limits or decreasing the lower potential limits, while Paik et al. [63] have reported that a higher frequency of potential cycling could also accelerate the dissolution of Pt into Pt ions.

Ferreira et al. [6] claimed that the significance of the MEOR in the degradation varies in different locations across the cathode using particle sizes distributions (PSDs) of Pt or Pt-alloy in the cathode as the evidence for Ostwald ripening. They showed that near the cathode-membrane interface, Ostwald ripening is more severe than in the areas far from membrane, due to the larger amount of crossover hydrogen from the anode side.

Previous to that, Granqvist et al. [64] illustrated the impact of Ostwald ripening on the PSDs and ECA loss by comparison between the results of the X-ray and TEM. They showed that if Ostwald ripening is the main mechanism of particle growth, the PSDs of the MEAs after potential cycling show a tail to smaller particles and a maximum particle size cut off as illustrated in Figure 2-8. Accordingly, this specific characterization of the PSDs has been widely used to analyze the surface area loss mechanisms in post mortem studies of PEMFCs. In this way, the degradation mechanism of the nanocatalysts is determined based on a comparison between the PSDs of the MEAs after potentials cycling and the theoretical models. However, there are still several challenges in utilizing this approach. First, there are usually more than one mechanism contributing simultaneously to the surface area loss during fuel cell potential cycling. Second, the determined PSDs of the nanocatalysts and the theoretical models might not reach the asymptotic limit. This is more sever when the PSDs are determined based on TEM data with a limited number of particles analyzed. Third, overlapping particles with unclear edges render a bias in the experimentally determined PSDs.

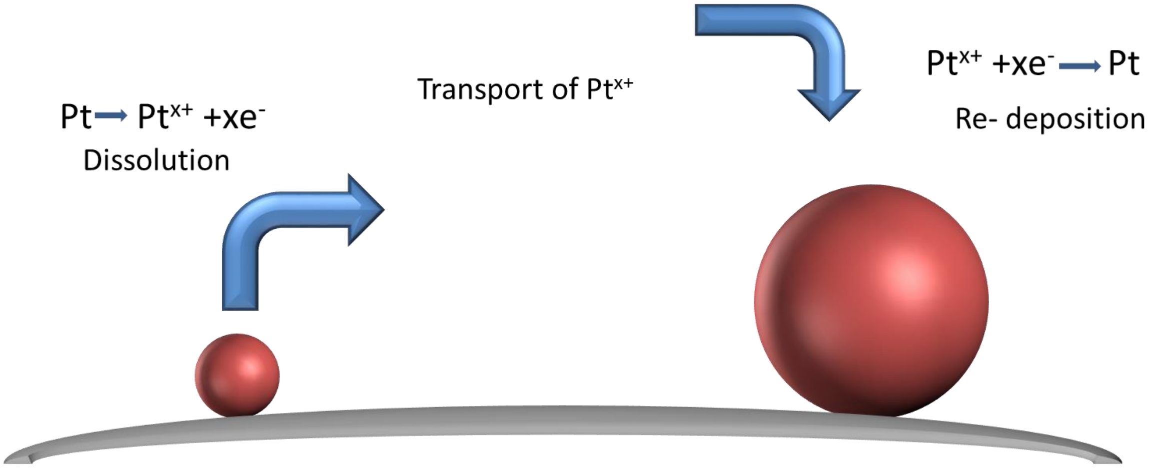

Figure 2-7 Schematic of modified electrochemical Ostwald ripening (MEOR).

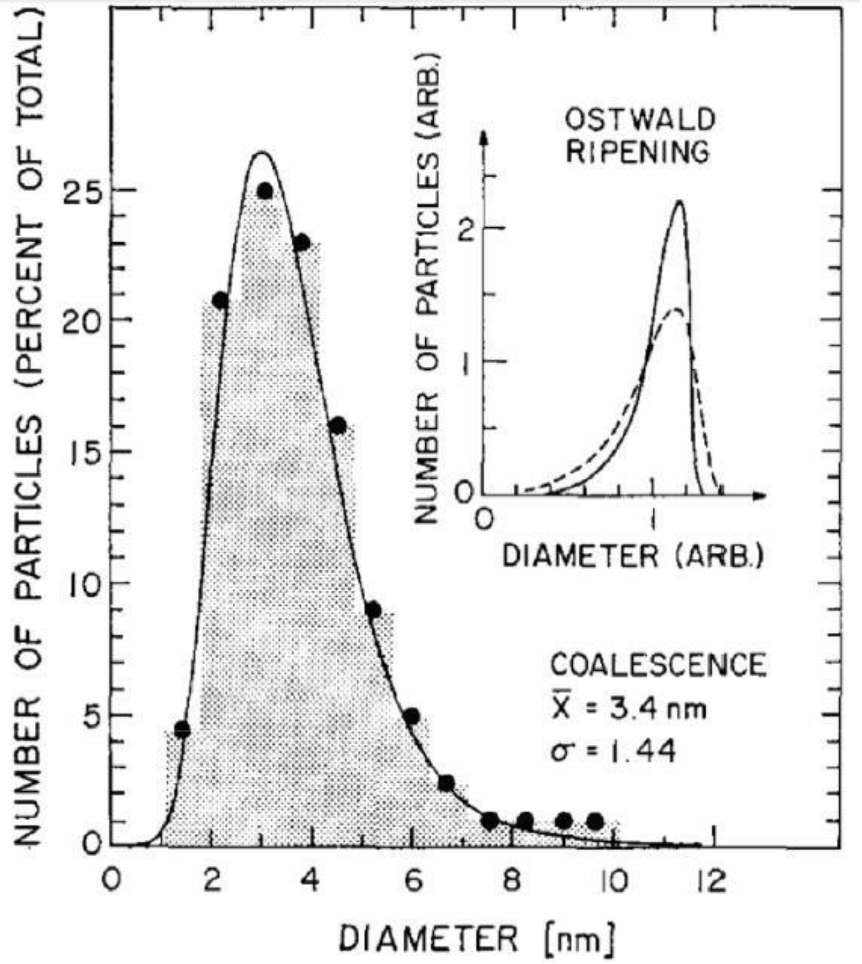

Figure 2-8 Theoretical model for the PSDs of single mode mechanism of particle migration and coalescence, and Ostwald ripening.

2.5.2.4 Particle Migration and Coalescence (PMC)

As illustrated in Figure 2-9, this mechanism involves moving of two or more particles on the carbon support, followed by contact onto each other and coalescence into one single particle.

According to classical theory, the diffusion of adatoms on the surface of a metal nanoparticle can lead to the movement of the mass center of the nanoparticle. Accordingly, the collective result from the diffusion of surface atoms over time can result in particle migration [65]. The theoretical models, which correlate the diffusion of surface atoms and particle movement, predict the possibility of movement of small particles. Increasing the size however, decreases the particle mobility significantly.

In situ electron microscopy has been extensively used to provide direct observation of particle mobility. Hansent et al, studied 3 nm Pt nanoparticles supported on SiO_2 with the average of 5 nm distance under 560 Pa of O_2 at 550 °C for up to 10 h in an environmental transmission electron microscope. During their observation for about 10 h, they did not observe significant change in the number of particles per unit area, ruling out PMC as being responsible. Simonsen et al. [66] performed similar experiments and they found coalescence merely happening at neighboring islands. So they found Ostwald ripening as a responsible mechanism for sintering of 2-5 nm size Pt nanoparticles. A similar conclusion was reached by Asoro et al. [67] using in situ heating transmission electron microscopy on Pt nanoparticles, observing no particle migration up to 800 C.

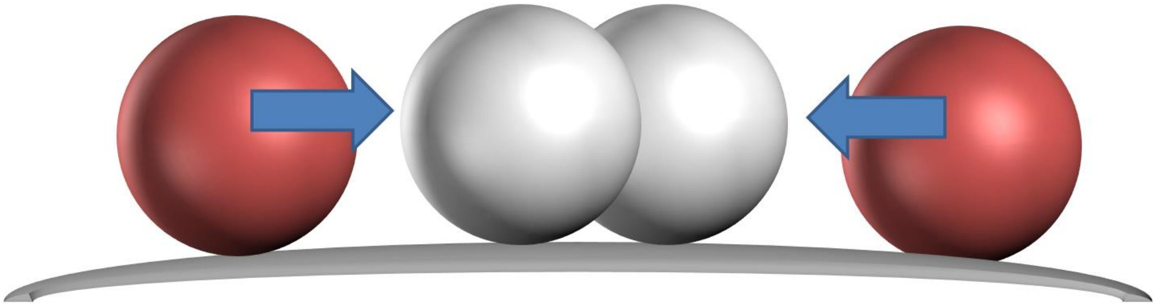

Figure 2-9 Schematic of particle migration and coalescence (PMC) mechanism

Shao-Horn et al. [61] claimed that PMC serves as the primary degradation mechanism at low upper potentials, since the kinetics for carbon corrosion and Pt dissolution are both slow. Schlogl et al. [68] observed the evidence for particle coalescence using identical location transmission electron microscopy to illustrate the PMC model in the PEMFC environment. Although they observed the presence of coalesced particles in the same area after potential cycling, they could not rule out the possibility that these coalesced particles may result from particle dissolution and re-deposition.

Granqvist et al. [64] used the PSDs of the nanoparticles in the MEAs to determine the particle growth mechanism. They predicted that the PSD of the catalysts after potential cycling illustrate a tale to larger particle size, if particle migration and coalescence is solely responsible for catalyst surface area loss. In contrast, Ferreira et al. [6] have shown that in the PSDs with tails to large particle sizes, most of the particles larger than 10nm were located off the carbon support area, indicating that these particles are formed by dissolution & re-precipitation. Shao-Horn et al. [61] demonstrated that the Brownian motion of Pt NPs under ideal PEMFC environment is too low to be responsible for particle growth.

In summary, although particle migration and coalescence should not be ruled out, direct evidence is needed to determine if it plays a significant role in the degradation of catalysts during potential cycling.

In order to explain the coalescence of nanoparticles, a simple model consisting of two spherical particles of the same size can be considered. This model, which is known as the two-particle sintering model is shown in Figure 2-10.

Reducing the chemical potential at the interface of two particles is the driving force for neck growth at the early stages of coalescence. Possible mass transport mechanisms for neck growth include grain boundary diffusion, surface diffusion, lattice diffusion, as well as deformation. Considering the large stress required for plastic flow in a face centered cubic nanoparticle, it is unlikely that plastic deformation will contribute significantly to the neck growth[69]. Thus, the diffusion mechanisms are more likely to dominate the sintering behavior of nanoparticles. According to Kuczynski et al. [70] the surface diffusion mechanism will be predominant at lower temperatures especially for small particles due to their larger surface atom-to-volume atom ratios. In addition, the surface diffusivity for FCC metals is at least many orders of magnitude larger than the other diffusivities at lower temperatures [71].

For surface diffusion, the change in neck radius, *x* with time, *t* for a given particle radius, *a* and temperature, *T* is given by the following expression [70], [72].

$$x^7 = \frac{56\Omega \mathrm{a}^3 \gamma_S D_S \delta_S t}{kT} \tag{2.6}$$

where Ω is the atomic volume, γ_s the surface energy, D_s the surface diffusivity, δ_s the surface diffusive width and *k* the Boltzmann’s constant.

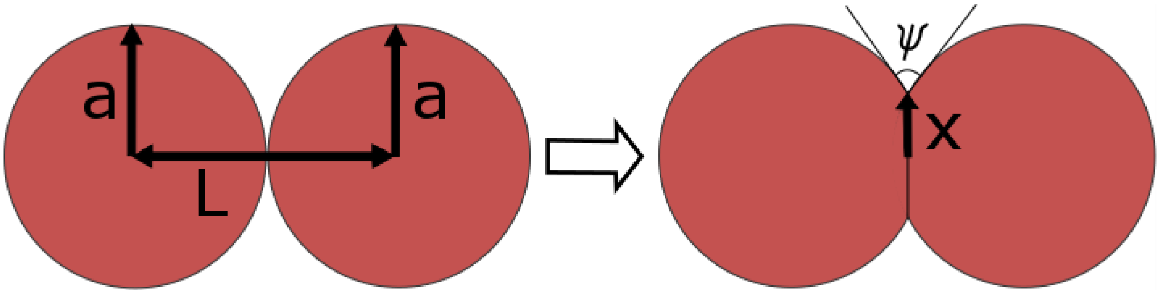

Figure 2-10 Two particle model of sintering between two spherical nanoparticles of radius a, with an interparticle distance, L. x is the neck radius and ψ is the dihedral angle.

Whereas surface diffusion dominates the early stages of low temperature sintering of FCC nanoparticles, the latter stages of sintering are dominated by grain boundary-driven coarsening [73]. The measurement of the dihedral angle, ψ allows us to determine the onset of particle coarsening. At equilibrium, the dihedral angle can be obtained from the following expression:

$$\gamma_{gb} = 2\gamma_s \cos\frac{\psi}{2} \tag{2.7}$$

where γ_{gb} is the grain boundary energy and γ_s is the surface energy. Neck growth is dominant when $\psi < \psi_{eq}$, whereas coarsening due to grain boundary motion is expected to dominate as the equilibrium dihedral angle is approached, which occurs during the latter stages of sintering. For curvature-driven grain boundary motion, the velocity of the grain boundary, v is given by the expression:

$$v = M\left(\frac{\Delta G}{V_m} - \frac{\gamma_{gb} \cdot dA}{V_m}\right) \tag{2.8}$$

where M is the mobility, $\Delta G/V_m$ is the driving force, V_m is the molar volume and ΔG is given by:

$$\Delta G = \frac{2\gamma_{gb} \cdot V_m}{a} \tag{2.9}$$

where γ_{gb} is the grain boundary energy and a is the radius of the nanoparticle. The additional term ($\gamma_{gb}\cdot dA/V_m$) in equation (2.8) is due to the increase in grain boundary area, d*A*, as the boundary moves from point A to point B (Figure 2-11). On this basis, equation (2.8) can be rewritten as:

$$v = M\left(\frac{2\gamma_{gb}}{a} - \frac{\gamma_{gb}.dA}{V_m}\right) \tag{2.10}$$

Therefore, from measurements of the boundary velocity and the increase in grain boundary area, the grain boundary mobility, *M*, which is a measure of the ease with which atoms can transition from one grain to another, can be determined. The boundary velocity can be calculated from the ratio of distance traveled by the boundary to the time taken for the boundary motion. The increase in grain boundary area, *dA* is calculated from the difference in boundary area assuming a circular boundary. This is a reasonable assumption for spherical particles as the boundary between two spheres is a circle. Thus, *dA* is given by:

$$dA = \frac{\pi}{4}\left(G_f^2 - G_i^2\right) \tag{2.11}$$

where G_i and G_f are the initial and final grain boundary diameters.

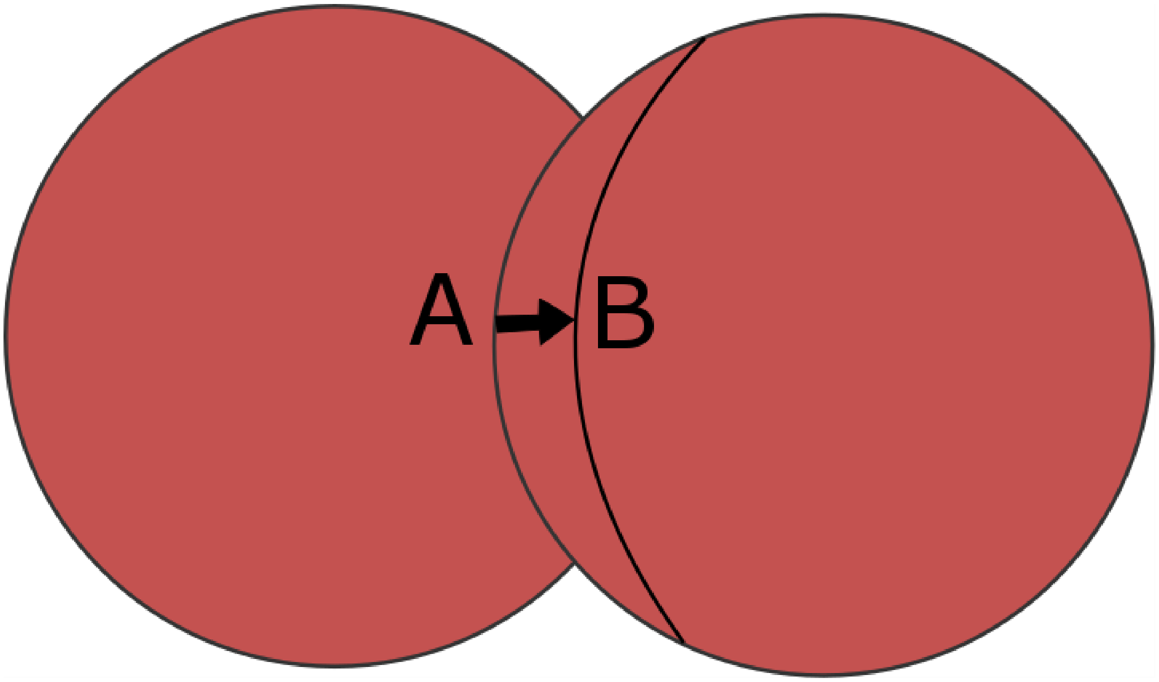

Figure 2-11 Schematic showing curvature-driven boundary motion during the later stages of sintering. Atoms move across the boundary from the particle on the right to the left particle, resulting in a boundary motion from point A to B.

2.5.3 Degradation of Pt Alloy nanocatalysts

Although Pt-alloy catalysts seems to offer a feasible route to enhance catalytic activity and lower the PEMFC cost, they create new challenges too. Achieving a small particle size distribution and high surface area dispersion of the catalysts on carbon support is a challenging process for Pt-alloys compared to pure Pt. moreover, Pt-alloy catalysts contain transition metals in their structure such as Co, Cr, Fe, Ni, and Ti, which are prone to leaching out the catalyst particles and thus can poison the PEMFC. The mixed-composition of Pt-alloy catalysts may make them more susceptible to accelerated degradation, corrosion, and deactivation.

In order to restrict transition metal leaching, researchers have introduced a de-alloying process, designed to remove the less noble metal which is poorly alloyed to the Pt prior to MEA preparation [74]. De-alloying of Pt-alloy catalysts not only reduce poisoning rate in the fuel cell, but in some cases, the de-alloyed catalysts show higher ORR activities. It has been shown in the literature that a superior activity can be achieved when carbon supported Pt-alloys with transition metal content of more than 50 at% are electrochemically de-alloyed [41]. This can be done by using fast voltammetric cycling up to 1.2 V vs RHE. Using this method, most of the transition metal is dissolved to the electrolyte preferentially from the surface of the nanocatalysts, producing a core shell structure with lower concentration of transition metal. As it was explained before, the ligand effect from the transition metal in the core induce a lattice strain to the surface and results in a shift in the d-band center of Pt surface atoms. This effect would be reduced considerably if the thickness of the Pt-rich surface is more than four monolayer. In this case, the activity will reduce to that of pure Pt. Therefore, the solubility of transition metal is the main challenge in Pt alloy durability.

In contrast to Pt, transition metals on the surface of Pt alloys can easily dissolve when exposed to dilute acidic electrolytes. For instance, in case of Pt-Co, increasing Co loss during acid leaching with decreasing the particle size has been shown as indicative of Co solubility from the surface of the particles [75]–[78]. This was also demonstrated directly via low energy ion scattering on polycrystalline Pt– Co, Pt–Fe, and Pt–Ni bulk alloy surfaces before and after exposure to 0.1 M HClO4 [79]. Leaching of the transition metal from the surface of nanocrystalline $Pt_{1-x}Fe{x}$ and $Pt_{1-x}Ni_x$ alloys (x = 0–1) after either acid or fuel cell operation was also found by X-ray photoelectron spectroscopy analysis in a PEMFC [80]. In another study on $Pt_{1-x}Co_x$ and $Pt_{1-x}Mn_x$ alloys (x = 0–1), it was demonstrated that in bulk concentration of more than 60 at%, the dissolution of transition metal is constrained to the top surface layers, otherwise the dissolution proceeds into the bulk of the nanoparticles [80]–[82]. Recently, Patrick et al. used aberration corrected scanning transmission electron microscopy (STEM) to analyze the atomic structure of acid leached and high temperature annealed Pt_3Co nanoparticles [36]. They showed that acid leached particles exhibited a solid solution structure with heterogeneous composition, while annealed Pt_3Co particles showed three atomic layers rich in Pt on the surface. The percolated structure of acid-leached Pt–Co nanoparticles were also recently imaged by HRTEM [83]. Since transition-metal ions reduce PEMFC performance [4] by poisoning the membrane and disturbing the proton transport, Pt alloys are often exposed to acid leaching to remove the soluble transition metal. Dubau et al. have studied the decay characteristic of Pt_3Co alloy in a 16 cells –stack, showing a continuous dissolution of Co in the ionomer phase during operation, which resulted in a core-shell structure with a Pt-enriched surface [13]. Chen et al. identified the increased thickness of Pt-rich surface layers as the main factor responsible for the degradation of acid-treated Pt_xCo catalyst after potential cycling [83]

2.6 Effect of Operating Conditions on the Degradation

The operating conditions for a fuel cell are highly dependent on the application and have a significant impact on the performance and durability. They will also have a significant impact on contamination effects. The conditions used in fuel cells today are typically those required by the fuel cells, but system developers desire different conditions to enhance system simplicity and reduce costs. The key drivers today are toward higher temperature and lower humidity conditions.

2.6.1 Temperature

The temperature at which a fuel cell operates has a strong influence on the performance and durability of the fuel cell. Typical fuel cell operation is in the range of 60 to 80°C, but increasing the operation temperature is advantageous as running at higher temperatures reduces the system cooling requirements and catalyst contamination issues. The relationship between temperature and performance is complex. An increased temperature drives increased kinetic activity for the oxygen reduction reaction (ORR); however, the reversible cell voltage decreases with increasing temperature [[16]. While the exchange current density increases at higher temperatures [84], the water loss in the membrane and catalyst layer will also increase at higher temperature, which results in decreased ionomer conductivity and decreased performance. The fuel cell may need to operate over a wide temperature range, from subzero to close to or over 100°C. The low temperatures also lead to reduced proton conductivity and consequently increased ohmic losses, which impact performance. On the other hand, increased temperature generally results in reduced adsorption of contaminants and, therefore, increased tolerance to the presence of contaminants [84] However, increased temperatures can significantly reduce durability. Many of the components degrade according to mechanisms exhibiting Arrhenius behavior, in particular, the membrane and cathode materials [16]. Bi et al [85] studied the effect of temperature on the Pt/C catalyst degradation. They quantified the performance decay, loss of catalyst active surface area, and Pt deposition in the membrane at 40, 60, and 80 ℃ under squarewave potential cycling. They showed that the performance decay and ECA loss are accelerated at high temperature. Moreover, the amount of Pt loss to the membrane and consequently particle precipitation in the membrane increased by increasing the temperature.

2.6.2 Humidity

Water content is an essential requirement i the fuel cell to maintain the proton conductivity inside the membrane and catalyst layer ionomer. Thus, water management is one of the most critical challenge in fuel cell operation. However, the presence of liquid water restricts the oxygen transport to the catalyst layer which is detrimental to performance. In addition, water droplets might disturb the gas flow, and consequently lead-to oxygen starvation and low cell voltage in the fuel cell. Moreover, Water provides a critical transport path for the contaminants as it solubilize the impurities [86]. Once a cell is contaminated, operating with high water content can help the removal of the contaminants through a flushing behavior. While the membrane is typically negatively impacted by low humidity conditions, the catalyst layer durability is generally higher under low humidity conditions. Both particle dissolution and carbon corrosion are both accelerated under wetter conditions. Both carbon corrosion and particle dissolution and re-deposition are accelerated under high humidity. The effect of the humidity particle dissolution and ion transport in the ionomer has been studied by Bi et al [87]. Under high humidity conditions, the polymer electrolyte exhibits large and abundant water channel networks. This is analogous to the effect of humidity on the proton conductivity of the Nafion electrolyte, as the higher water content in the Nafion electrolyte results in higher mobility of protons in the membrane.

Chapter 3: Experimental Methods

This chapter focuses on the basics of the experimental methods, whereas a detailed description of the various experimental procedures are given in the corresponding chapters. In particular, first, single cell evaluation, cyclic voltammetry, and methods to determine the electrochemical active surface area (ECA) are presented. Then scanning/transmission electron microscopy (S/TEM), TEM sample preparation and finally identical location S/TEM are described.

3.1 Single cell evaluation test

The single cell test is a direct and effective method for the evaluation of catalyst layers and MEAs. The single cell evaluation requires a test station to measure and control various parameters during the test, such as temperature, pressure, humidity, and flow rates of the reactant gasses and coolant, in addition to the current and voltage of the fuel cell. As shown in Figure 3-1, a test station typically consists of a gas control station, fuel cell, load bank, data acquisition/control unit, and finally a control software. Regulation of the temperature, humidity, backpressure, and gas flowing rate is performed in the gas control station which is consist of gas meter and humidifier. The explosive gas leaking is detected and removed from the gas station by a safety unit. The humidifying the reactant gases are performed by directing the fuel gas to bubble through water until the desired humidity level is acquired. The load bank can apply several load mode for the test such as constant current, voltage, and power. The control unit which is also called the data acquisition unit is used to monitor and collect all date from the test station and fuel cell system [88].

Figure 3-2 shows a schematic illustration of a fuel cell single cell which is the most important component of the test station [89]. A plastic plate is used to isolate the carbon plate/current collector and the end plate. Gaskets are used to seal the MEA. In order to seal the cell assembly, a pressure bladder which is controlled with nitrogen gas, is used. The cell heating is accomplished with a pair of heat tapes. The inner heat tapes which are glued onto the copper current collector plates, allow the cell to operate at the desired temperature [88].

3.2 Cyclic Voltammetry

Cyclic voltammetry is the method for the initial investigation of an electrochemical system and has also been proven to be useful in obtaining information about complicated electrode reactions [90]. This electroanalytical technique is also referred to as “electrochemical spectroscopy” due to the fact that the potentials of occurring processes are determined. In this respect, faradaic processes involving charge transfer across the metal-solution interface, as well as nonfaradaic processes like adsorption and desorption can be observed. This technique is based on varying the applied potential at a working electrode (WE) by a specific scan rate, while the current is monitoring. During cyclic voltammetry, the potential E(t) of the working electrode is periodically sweep between a lower limit E_{min} and an upper limit E_{max} , through a triangular or square waveform. For the triangle waveform the potential is changing according to equation (2-1):

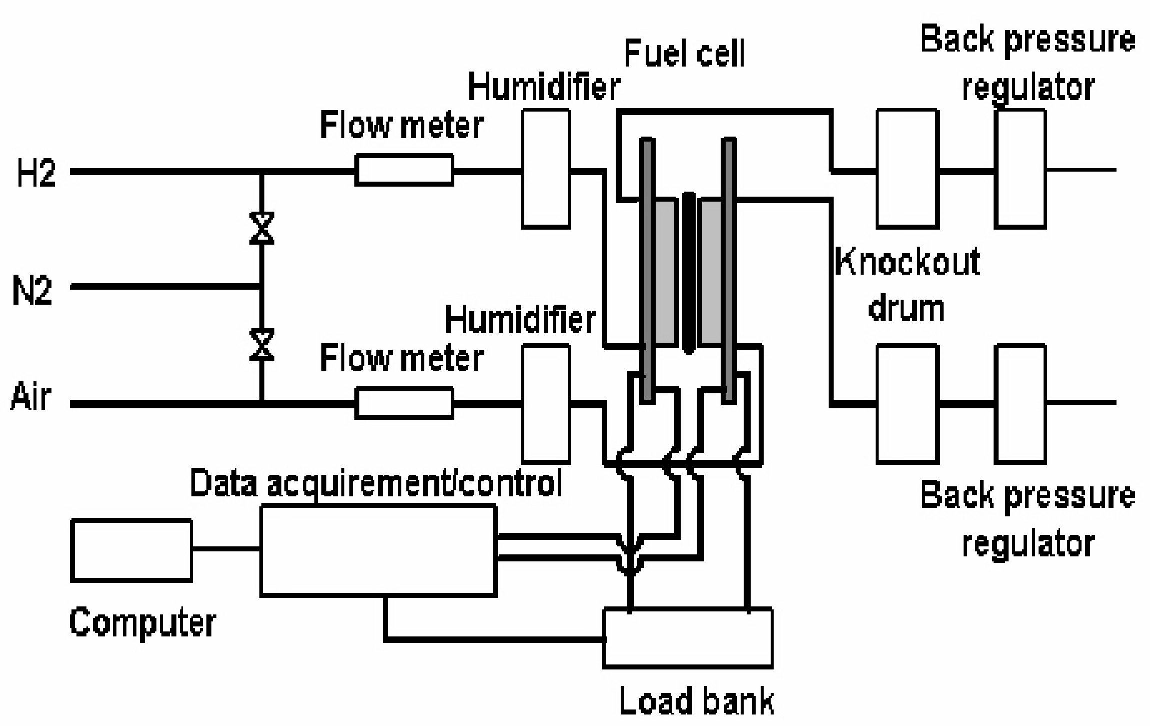

Figure 3-1 Schematic of a fuel cell test station [103]

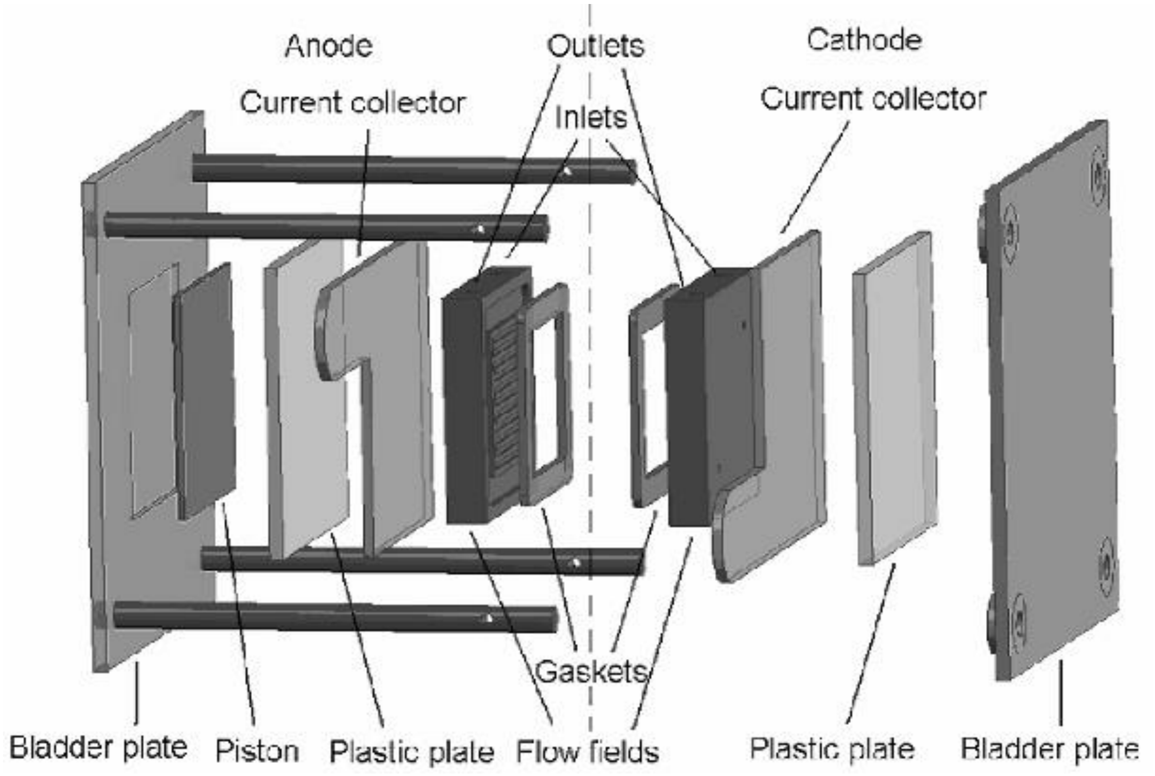

Figure 3-2 Schematic of a single cell [89]

$$E(t) = \frac{E_{min}}{EE_{max}} \pm vt \tag{2-1}$$

The scan rate ν is the rate of change of the potential with time (Figure 3-3a). For the square-wave form the potential is kept at the low and high potential limit for a specific amount of time (Figure 3-3b). The responding current passing the WE is recorded as a function of the respective potential resulting in a current-potential plot, called cyclovoltammogram (CV).

Typically, cyclic voltammetry is conducted in a three-electrode-setup in order to guarantee an exact control of the potential at the WE, which is determined relative to a reference electrode (RE). The RE is an electrode with a stable and well known electrode potential, arising from a redox system with constant concentrations of each reactant. The reference electrode should provide a reversible half-reaction with Nernstian behavior, be constant over time, and be easy to assemble and maintain. The most commonly used reference electrodes for aqueous solutions are the calomel electrode, with potential determined by the reaction:

$$Hg_2Cl_2\,(s) + 2e^- = 2Hg(l) + 2Cl^- \tag{2-2}$$

and the silver/silver chloride electrode (Ag/AgCl), with potential determined by the reaction:

$$AgCl(s) + e^- = Ag(s) + Cl^-$$

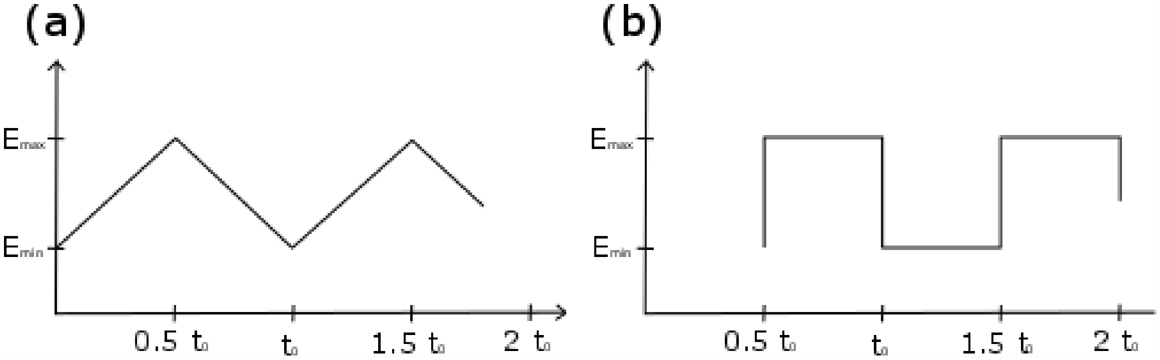

Figure 3-3 Potential vs time for a) triangular wave, b) square-wave potential cycling

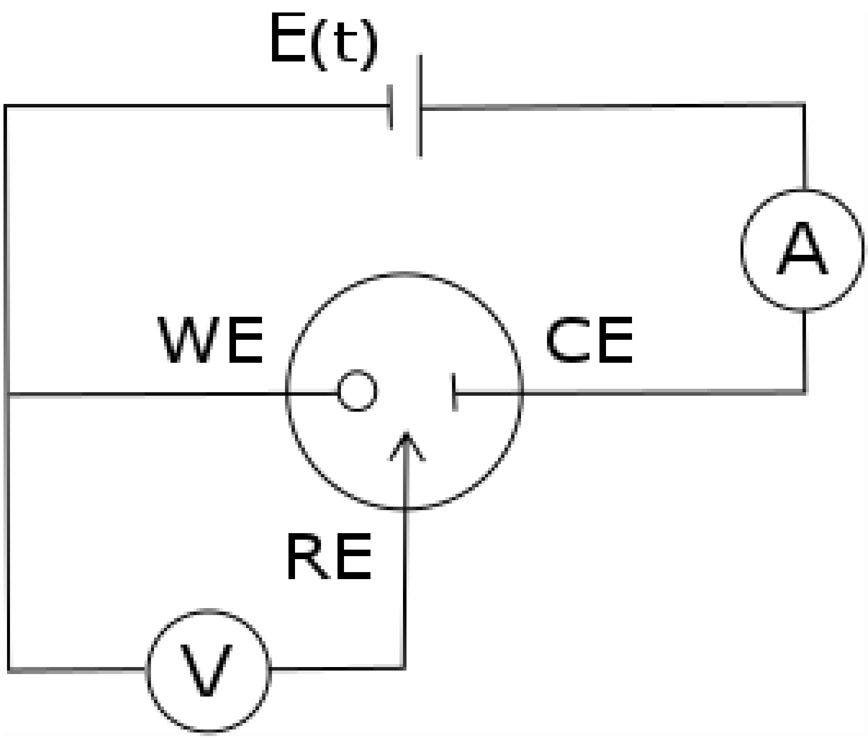

Figure 3-4 The circuit in a three-electrode set-up

The counter electrode (CE) is an auxiliary electrode through which the current from and to the WE flows (see Figure 3-4). The pathway between WE and RE remains practically free of current, the RE represents an ideal nonpolarizable electrode. Consequently, the measured change in potential between the working and the reference electrode is equal to the actual change in potential at the working electrode. The potential at WE (vs RE) is adjusted by the potentiostat through an adequate current flow in the circuit between the WE and the CE [90], [91].

3.3 Electrochemically Active Surface Area (ECA) Measurement

Since the catalytic reactions during fuel cell operation happen at the surface of the catalysts, the number of active sites is one of the most important properties of the catalyst. Typically, adsorption techniques are used to determine the electrochemically active surface are (ECA) of the catalyst. Thereby, suitable probe molecules, which adsorb exclusively on the active surface sites are adsorbed and quantified. For the ECA measurement of platinum, hydrogen atoms and carbon monoxide molecules are commonly used as adsorbates. Both are assumed to bind as single atoms and molecules, respectively, on top of each surface platinum atom [92], [93]. The ECA is then quantified by measuring the current during desorption or oxidation of one monolayer. Hence, it can be either calculated from the charge it takes to either adsorb/desorb a layer hydrogen in the so called H_{upd} region in a CV, or to oxidize a monolayer of CO, which was already adsorbed on the surface, in a potentiodynamic stripping experiment. Although, the H_{upd} area is traditionally used for ECA measurements, due to the accessibility of the CVs. In this method, the electro-adsorption of H_{upd} is referred to as under-potential deposition because the process takes place at a potential that is lower than the potential required to generate H_2(g) [94]. For this method, a usual CV is recorded and the ECA is calculated by integrating the hydrogen adsorption/desorption charge in the voltammogram, dividing by cell active area (cm^2), 210 $\mu C/cm^2$ (theoretical hydrogen monolayer adsorption on Pt) and the cathode initial Pt loading (mg-Pt/cm^2).

3.4 Scanning/Transmission Electron Microscopy

Due to the development of nanoscience, microscopic imaging with atomic resolution has become essential. In transmission electron microscopy (TEM), a thin specimen is irradiated with an electron beam of uniform current density. From the transmitted electrons, after interaction with the specimen, an image is formed, giving an insight into the microscopic nature of the sample. An electron source at the top of the microscope emits the electrons, which are accelerated with 60-300 kV. In the condenser system consisting of electromagnetic lenses and apertures, the electrons are focused into a thin colliminated beam. Then, the beam passes the specimen where the electrons interact with the material. In this regard, the electrons can be transmitted, diffracted, backscattered or they induce the emission of photoelectrons, x-ray fluorescence or Auger electrons. The electron intensity distribution behind the specimen is imaged and magnified.

TEM image contrast arises due to the scattering of the incident beam by the specimen. As the electron wave traverses the specimen, both the amplitude and the phase of its wave can change, which in turn gives rise to image contrast. Schematic of atomic-resolution phase contrast and Z-contrast imaging is illustrated in Figure 3-5. An atomic Phase contrast image is formed by interference between direct and diffracted waves while a parallel beam is illuminating the specimen. In other word, contrast in TEM images can arise due to the differences in the phase of the electron waves scattered through the specimen. This contrast mechanism can be difficult to interpret because the appearance of the image varies with small changes in the thickness, orientation, or scattering factor of the specimen, and variations in the focus or astigmatism of the objective lens. However, its sensitivity is the reason phase contrast can be exploited to image the atomic structure of this specimens. A phase-contrast image requires the selection of more than one beam. In general, the more beams collected, the higher the resolution of the image. Phase-contrast imaging is often thought to be synonymous with high-resolution TEM.

Unlike conventional TEM, where the simultaneous interaction of the electron beam with a large area of the sample will generate the magnified image, in a scanning transmission electron microscope, the convergent electron beam is scanned across a thin sample, and the transmitted beam collected by a detector located below the sample will produce the image. High angle annular dark-field imaging (HAADF) is a method of imaging samples in STEM, in which images are formed by collecting high angle incoherently scattered electrons with an annular dark-field detector. STEM combined with an annular-detector provides atomic-resolution images by effectively illuminating each atomic column one-by-one as a finely focused electron probe scans across the specimen, generating an intensity map at the annular detector [95] (Figure 3-5, right). As opposed to phase contrast images, HAADF images are highly sensitive to the variations in the atomic

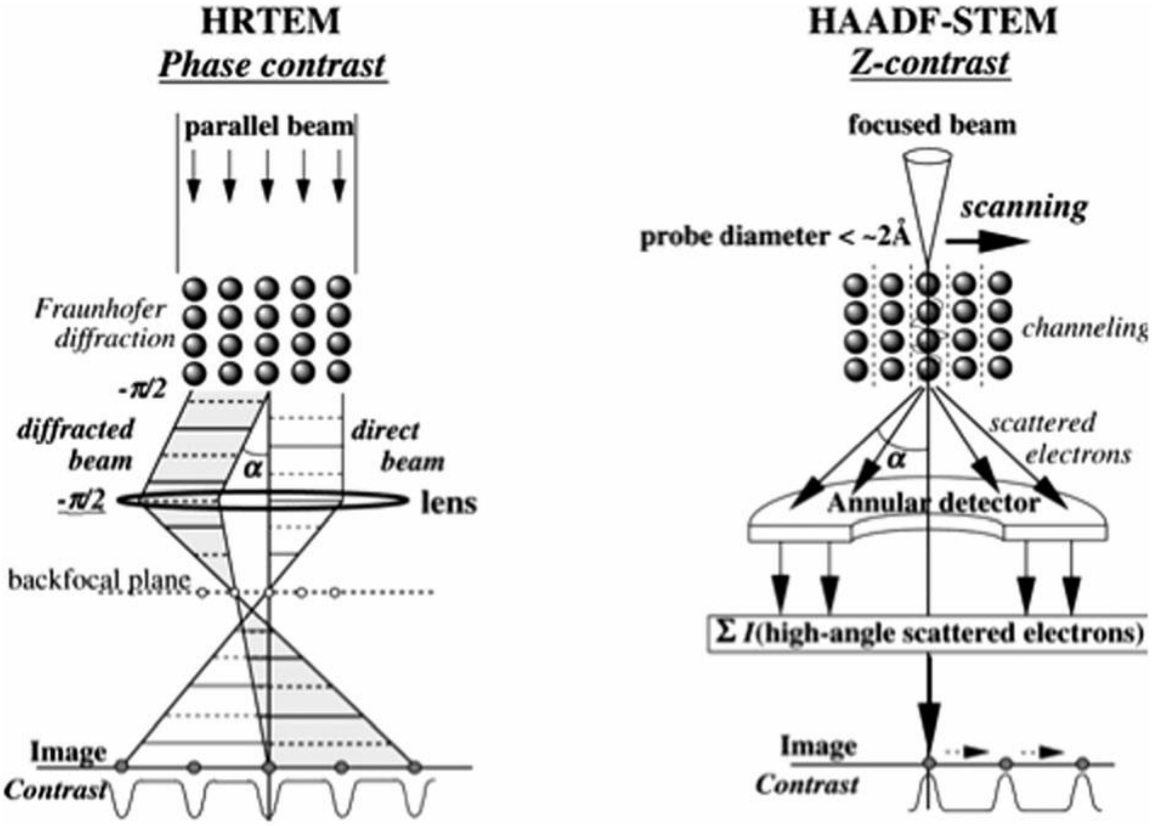

Figure 3-5 Imaging principle of atomic resolution phase contrast TEM and Z-contrast STEM [96]

number of atoms and the thickness of the sample. At high-angle scattering, the Bragg intensities are significantly weakened, and instead the background diffuse scattering becomes dominant Thus, STEM images are mass thickness contrast with negligible diffraction contrast and the intensity of the HAADF image is approximately proportional to the square of the atomic number (Z^2) and linearly proportional to thickness (t) [96].

3.5 Energy Dispersive Spectroscopy

Energy dispersive spectroscopy (EDS) is an analytical technique used for elemental analysis and chemical characterization. This technique is based on high-energy electron beam penetrating through the outer conduction/valence bands which interact with the inner-shell (or core) electrons. This electron is ejected if it receives more than a critical amount of energy; i.e. it escapes the attractive field of the nucleus to an unfilled state above the Fermi level, leaving a hole in the inner shell. The atom is then left in an excited state, which is described as ionized state. An electron from an outer shell will fill the hole to reduce the energy of the excited atom to its ground state. This transition is accompanied by the emission of either an X-ray or an Auger electron. In both the X-ray and Auger cases, the energy of the emission is equal to the difference in energy between the two electron shells involved. Since this energy difference is unique to the atom, the emitted x-ray is called characteristic x-ray and can be used to identify the element. The process of X-ray emission is shown schematically in Figure 3-6.

To make use of the characteristic X-rays generated when the beam strikes the specimen, semiconductor detectors such as Si and Ge are used to collect them and identify from which element they originated. When X-rays deposit energy in a semiconductor, electrons are transferred from the valence band to the conduction band, creating electron-hole pairs. Since characteristic X-rays typically have energies well above 1 keV, thousands of electron-hole pairs can be generated by a single X-ray. The number of electrons or holes created is directly proportional to the energy of the X-ray photon. Thus, enough electron-hole pairs are created to collect sufficient signal to distinguish most elements in the periodic table, with good statistical precision.

3.6 TEM Sample Preparation

In this work we used ultra-microtomy with diamond knife to prepare the cross sections of MEAs for TEM observation. For this purpose, a strip of MEA is embedded in a hard resin such as epoxy and then is cut by a diamond knife in the mictrotome to the required thickness (less than 70 nm). Finally, the cross section of the MEA will be placed on the TEM grid and is ready for TEM observation. Figure 3-7 shows different steps of the microtomy technique for MEA cross section preparation. Figure 3-8 illustrates a TEM image of an MEA cross section which was prepared using microtomy technique.

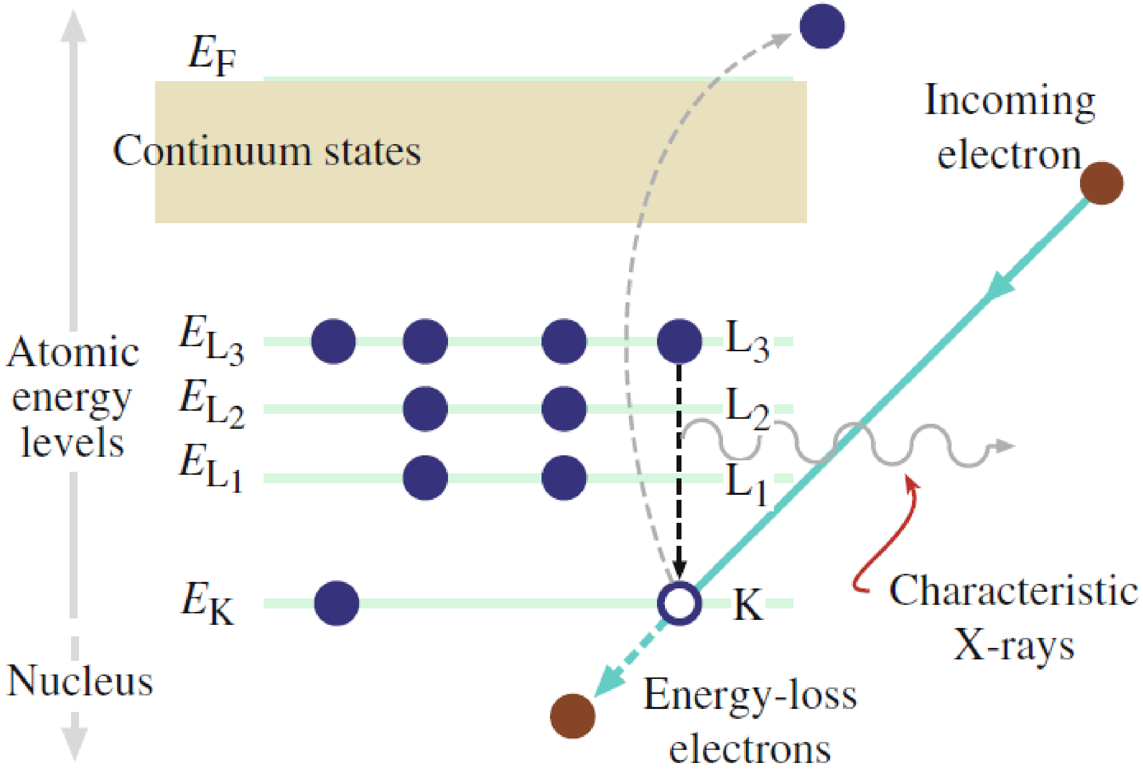

Figure 3-6 Schematic of the emission of characteristic X-ray emission

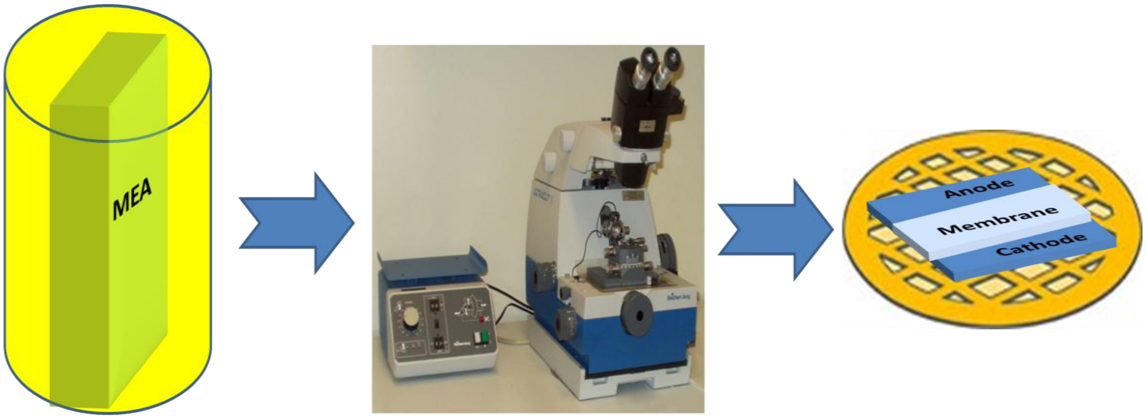

Embedding in epoxy

Microtomy

Cross section

Figure 3-7 MEA cross section preparation method using microtomy technique.

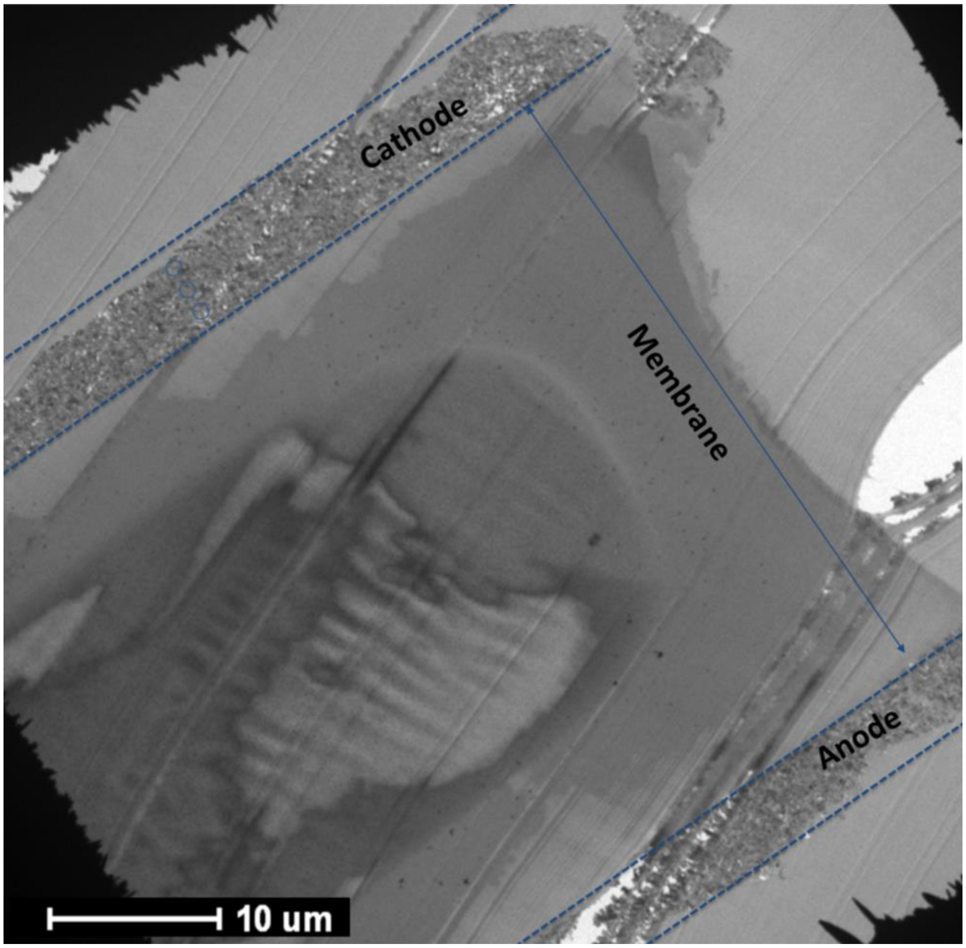

Figure 3-8 Low magnification TEM image of an MEA cross section prepared by microtomy

3.7 Identical Location TEM

This method is based on the ex-situ electrocatalyst accelerated stress test in a classical three-electrode electrochemical cell using liquid electrolytes (half-cell). For this method, the TEM grid itself is used as a working electrode for the accelerated stress tests to replicate on a TEM grid the effect of potential cycling on the cathode side of the fuel cell outside of the microscope. In order to be able to find the same location before and after the stress test, specific features on the grid and a series of TEM images at different magnification is used to provide the map of the area of interest. TEM grid is made of gold, because it has to be stable in the electrolyte at the voltage range during potential cycling. The TEM grid used in this work is coated with a quantifoil holy carbon.

The identical location TEM procedure is schematically shown in Figure 3-9. It consists of the following steps:

1. Deposition of the catalyst on the TEM grid
2. Preliminary TEM observation to find the area of interest (R.O.I) on the TEM grid
3. Potential cycling of the TEM grid in the electrochemical cell
4. Re-characterize the R.O.I

The catalyst powder supported on carbon is sonicated in ethanol to disperse homogenously. Thereafter, a drop of the dilute suspension is deposited on the grid. The grid is rinsed then with deionized water to remove the material which is loosely attached to the grid and then

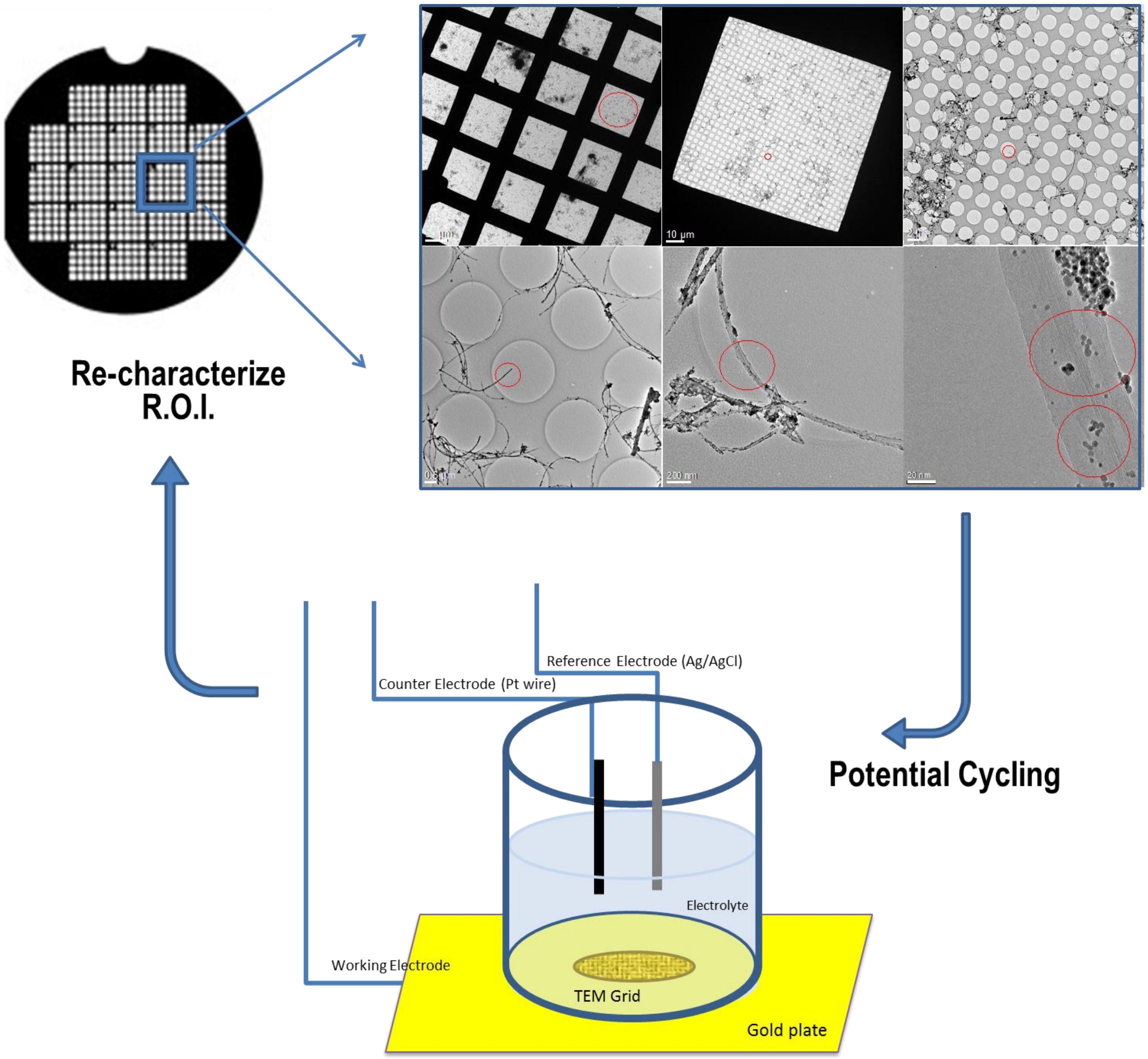

Figure 3-9 Schematic of identical location procedure

dried under ultraviolet lamp. The grid is then fixed on a gold plate and is placed on the electrochemical cell. The electrochemical cell used in this work is called plate material evaluating cell from ASL, Japan (product number 011951). Figure 3-10shows the electrochemical cell and the steps required to prepare the set-up. After fixing the TEM grid on the gold plate, the Teflon plates should be placed on top of each other and fixed by the screws. The cell is then filled with liquid electrolyte, and the reference and counter electrode is placed inside the cell, in contact with the electrolyte. At the final stage, the working, counter and reference electrode are connected to the potentiostat. After performing the potential cycling, the grid is rinsed and dried and re-characterized inside the microscope.

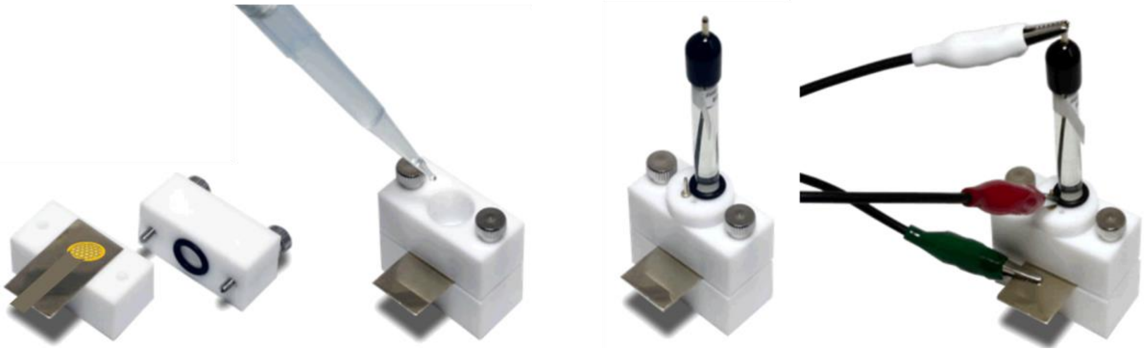

Figure 3-10 preparing the electrochemical cell for identical location experiment

Chapter 4: TEM study on the Degradation Mechanisms of Nanocatalysts

4.1 Introduction

It has been demonstrated in the literature that potential, temperature, and humidity affect the catalyst degradation during fuel cell operation [14]. Higher upper potential limit of cycling can occur at high fuel utilization conditions and/or during start up or shut down. Darling and Meyers used a simple model to describe the rate of platinum dissolution as a function of potential [97], [98]. They showed that platinum can dissolve at rapid rates by increasing the cathode potential, until a passivating oxide layer is formed. Humidity, on the other hand, does not have a significant effect on solubility but on the ion mobility according to Bi et al [87]. Accordingly, high potential and low humidity conditions are extreme conditions that impact the Pt dissolution kinetics and migration to the membrane, while high temperature will affect the Brownian motion and thus particle mobility on the carbon support. Thus, each of these parameters during operation affects the catalyst degradation in a different way. Therefore, the parametric gives us an insight into the mechanisms of electrochemical active surface area loss in the fuel cell and helps us find out how we can mitigate the degradation of the catalyst on the cathode of the MEA. The focus of this part is to understand the mechanism of surface area loss in Pt_3Co nanocatalysts by analyzing the cathode of the PEMFC membrane-electrode assembly (MEA) at different distances to the membrane, during potential cycling under different operating conditions. The operating conditions include 1) baseline condition, 2) high upper potential limit (1.05 V), 3) high temperature (9℃) and 4) low humidity (30% RH). The reason for performing this study on Pt_3Co alloy NPs instead of Pt is the changes in composition which occur in Pt_3Co particles after voltage cycling. This allows us to track the mechanisms responsible for particle growth. For example, if the mechanism of Pt dissolution and re-deposition is operating, both Pt and Co are known to dissolve, but only Pt redeposits on the surface of other particles, which leads to a decrease of the Co/Pt ratio. This change in composition enables us to differentiate between particles growing via particle dissolution and re-deposition and the ones resulting from particle migration and coalescence.

4.2 Experimental

4.2.1 Materials

Catalyst Preparation and Membrane Electrode Assembly (MEA): The catalysts for the cathode were prepared by deposition of 40 wt % Pt and Co (3:1 atomic ratio) onto Akzo Nobel Ketjen EC300J via proprietary methods, then annealed to achieve alloying and produce Pt_3Co catalysts of specific particle size. MEAs were fabricated via a developmental process, with 35.6 wt% Pt/C (2 nm Pt particle size) on the anode and a 25μm thickness perfluorosulfonic acid (PFSA) membrane. All the cathode electrodes had the same Pt loading of $0.2mg\pm0.02mgPt/cm^2$, while the anode electrodes had a similar loading of $0.22mg\pm0.05mgPt/cm^2$.

4.2.2 Decay protocol for parametric studies

The accelerated cell degradation test conditions (Table 1), were carried out by potential cycling using a potentiostat (EG&G 273A, Princeton Applied Re- search Inc., Oak Ridge, TN). A square-wave potential cycle with 20s/cycle was imposed on cells with different temperature, RH, and voltage window conditions for 10K cycles. A fixed gas flow of 0.5 SLPM 4% H_2 balanced with N_2 on the anode and 0.5 SLPM N_2 on the cathode were used. A new MEA with 4.9 nm Pt_3Co particle size in the cathode was used for each test to evaluate the impact of various parametric conditions, namely high temperature, low RH, and high upper potential limit on cell decay behavior. During the potential cycling, the cathode served as the working electrode, while the anode served as both the reference and counter electrodes. The electrochemically active surface area (ECA) of Pt and Pt_3Co cathode catalysts at different stages of potential cycling was measured using a cyclic voltammogram at 10 mV/s between 0.03 and 1.0 V (vs anode) with nitrogen flowing on the cathode, 4% hydrogen (balance nitrogen) on the anode. The ECA values (m^2/g-Pt) were calculated by integrating the hydrogen adsorption charge in the cathodic-going sweep of the voltammogram, multiplying by the cell area, and dividing by 210 $\mu C/cm^2$ (theoretical hydrogen monolayer adsorption on Pt) and the cathode Pt loading.

4.2.3 Transmission electron microscopy

First, the Pt_3Co powder was dispersed in ethanol, ultrasonicated and deposited on a carbon/copper grid for TEM characterization. Subsequently, MEA samples for TEM analysis were prepared by cutting a 1mm wide strip of the cycled MEAs. Previously heated

Hard Plus Resin 812 epoxy is poured into a mold containing the MEA sections, which is cured in a vacuum oven at 60 C for a minimum time of 72 hours. The cured molds were microtomed at room temperature, and subsequently, electron transparent MEA sections of about 70 nm thick were obtained. The morphology and size of nanoparticles present on the cathode side of the membranes were observed using a JEOL 2010F transmission electron

Table 4-1 Operating conditions used for testing the electrochemical stability of the 4.9 nm Pt_3Co catalysts.

Cell	Potential cycle
Baseline	Square wave potential cycle: 10s at 0.4V, 10s at 0.95V (20s/cycle) Cell Temperature: 80℃ Humidity: Anode = Cathode = 100% RH Fuel/Oxidant : 0.5 SPLM 4% H2/0.5 SPLM N2 Pressure: Atmospheric pressure
Low RH	Humidity: Anode = Cathode = 30%RH All other parameters as baseline
High Upper Potential	Square wave potential cycle: 10s at 0.4V, 10s at 1.05V (20s/cycle) All other parameters as baseline
High Temperature	Cell Temperature: 90℃ All other parameters as baseline

microscope operated at 200kV. For this study, the cathode region was divided into three areas, each approximately 3µm wide and thereby covering the cathode width of approximately 10µm. Two hundred particles were analyzed from each of the regions to give a total of six hundred particles for a cathode section in a used MEA. Energy dispersive X-ray spectroscopy (EDS) coupled to the TEM was used to analyze the composition of the cathode. The Pt/Co composition ratio of different particles was determined from the intensity ratio of the Pt L-line and the Co K-line, using the EDS spectra.

4.3 Results

The electrochemically active surface area of the cathode, measured through hydrogen adsorption in a cyclic voltamogram, is illustrated in Figure 4-1 ECA loss of Pt3Co cathode nanocatalysts as a function of number of potential cycles under different operating conditions. According to ECA decay rates, the degradation of the MEAs as a function of number of cycles is substantially higher for the MEAs operated at higher upper potential limit compared to the ones operated at low humidity. The ECA losses under high temperature and baseline conditions occur at lower rates than high voltage but higher rates than low humidity conditions. As shown in Figure 4-1 ECA loss of Pt3Co cathode nanocatalysts as a function of number of potential cycles under different operating conditions. , the cathode of the MEA operated at low humidity exhibited very good stability with only 5% loss of surface area within 10K cycles while the ECA of the high potential sample decreased by 65% up to 10K cycles.

4.3.1 Particle Size Distribution

AThe particle size distribution (PSD) of the powder sample used to fabricate the MEAs is shown in Figure 4-2. The mean equivalent diameter d_{eq} is 4.9±0.2 nm with sizes ranging from 2 to 11 nm, while the majority of particles lie between 3 to 7 nm. Figure 4-3-Figure 4-5 contain the results of the TEM analysis of the cycled cathodes operated at different conditions, namely baseline, 30% RH, high upper potential limit, and high temperature. Images from three separate regions, 3µm in length, were acquired across the 10µm width of the cathode. As illustrated in Figure 4-3-Figure 4-5, Regions A, B, and C represent regions of the cathode located at distances 0-3µm, 3-6µm and 6-9µm from the cathode/membrane interface, respectively. A sample size of 200 nanoparticles was chosen for each region of the cathode, leading to a total 600 nanoparticles for each sample. the cathode area grow from 4.9 nm to about 8.3 nm (mean particle size in Regions A, B, and C, combined) after 10K cycles (Figure 4-3) and the distribution has broadened significantly. The PSDs exhibit a tail to larger sizes of up to 33 nm. There is no significant difference in the mean particle size of regions A, B and C to 95% confidence.

In the case of the 30% RH sample (Figure 4-4), a mean particle size of approximately 7.1 nm was obtained after 10K cycles. In comparison with the PSD of the powder sample (Figure 4-2), it can be seen that the particle size distribution did not change significantly after 10K cycles of operation under 30% RH. Compared to the baseline sample, no tail toward larger particles is seen in the PSDs of the low humidity sample. The difference in the mean particle size of the three different regions is negligible to 95%

Particle size distributions of the baseline sample show that the Pt_3Co nanoparticles in

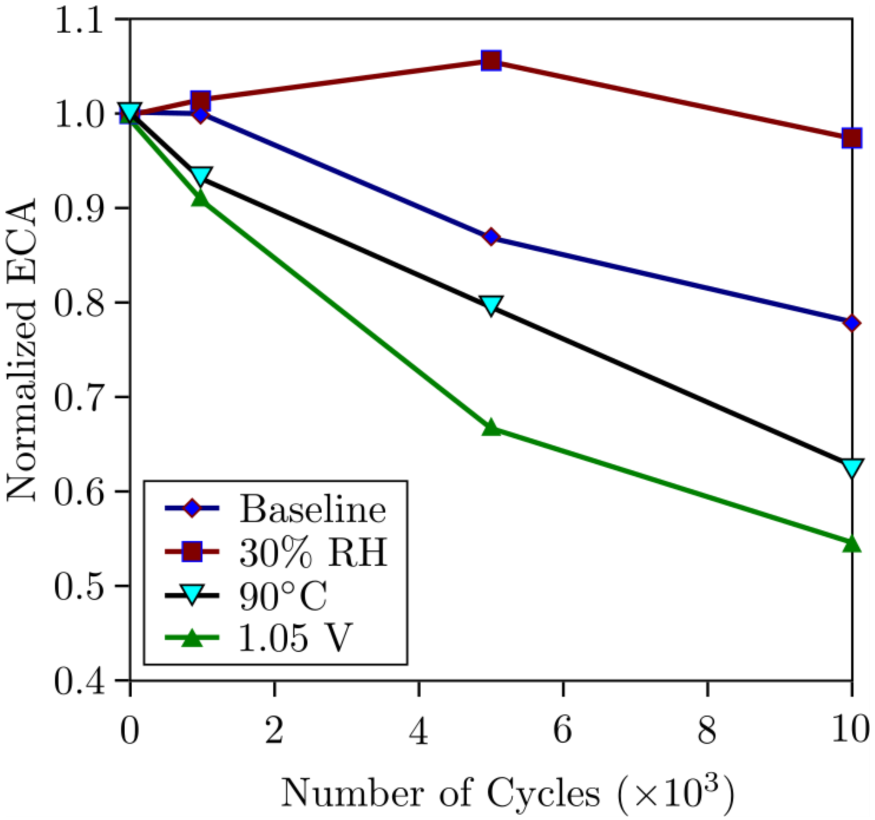

Figure 4-1 ECA loss of Pt3Co cathode nanocatalysts as a function of number of potential cycles under different operating conditions.

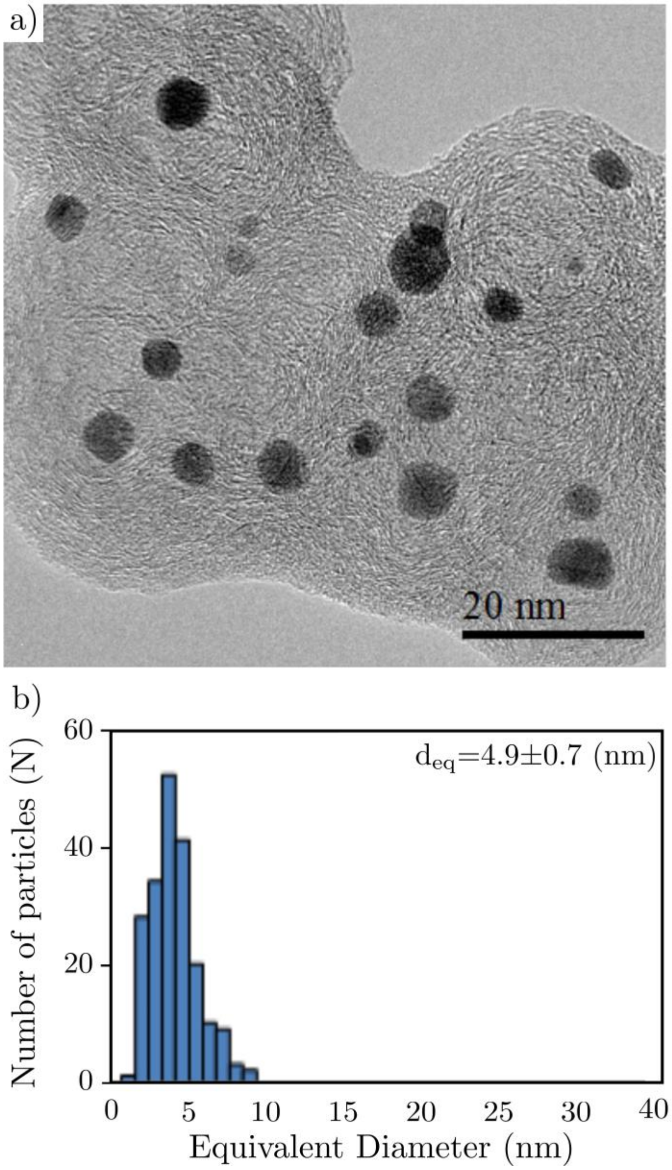

Figure 4-2 a) Bright field TEM image, and b) particle size distribution of the Pt_3Co noparticles.

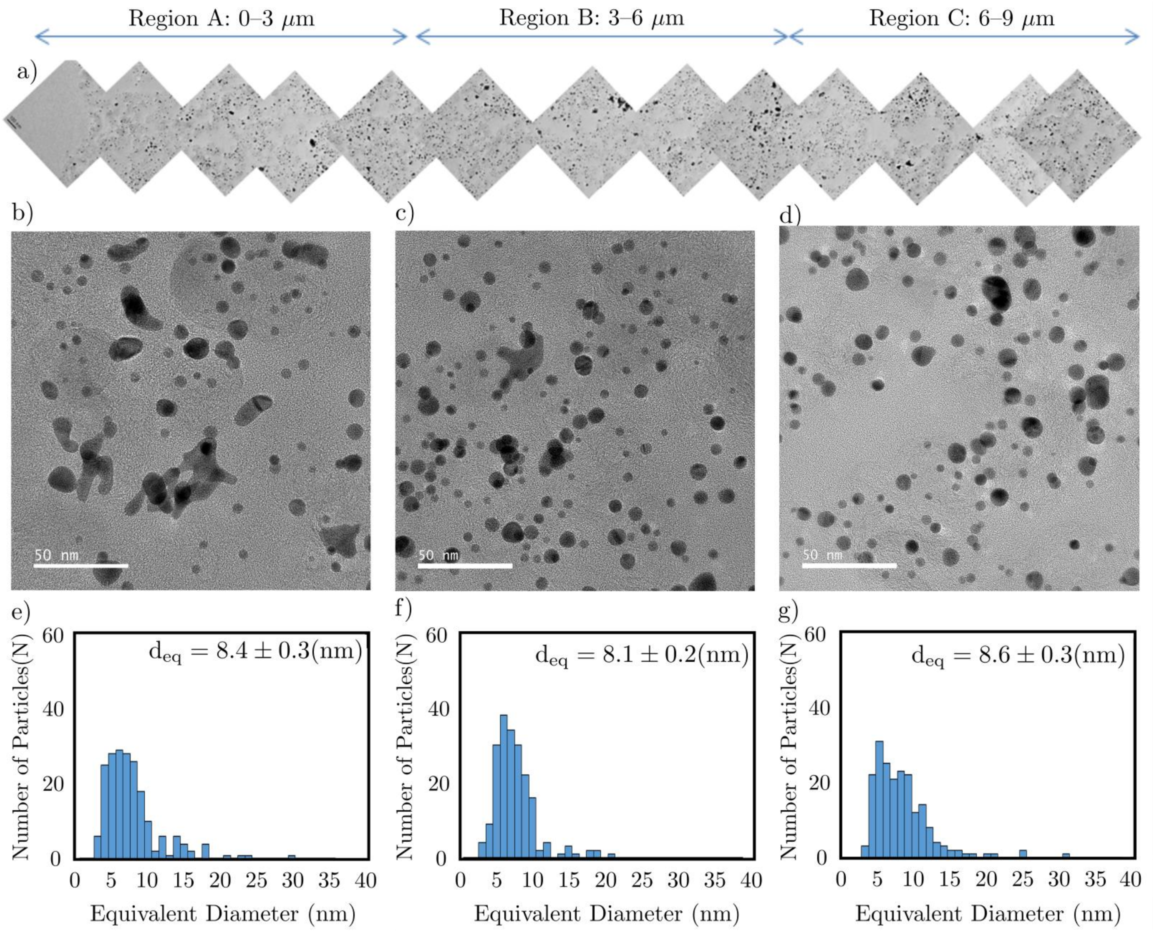

Figure 4-3 TEM Characterization of the cathode area of the baseline MEA after 10K cycling.

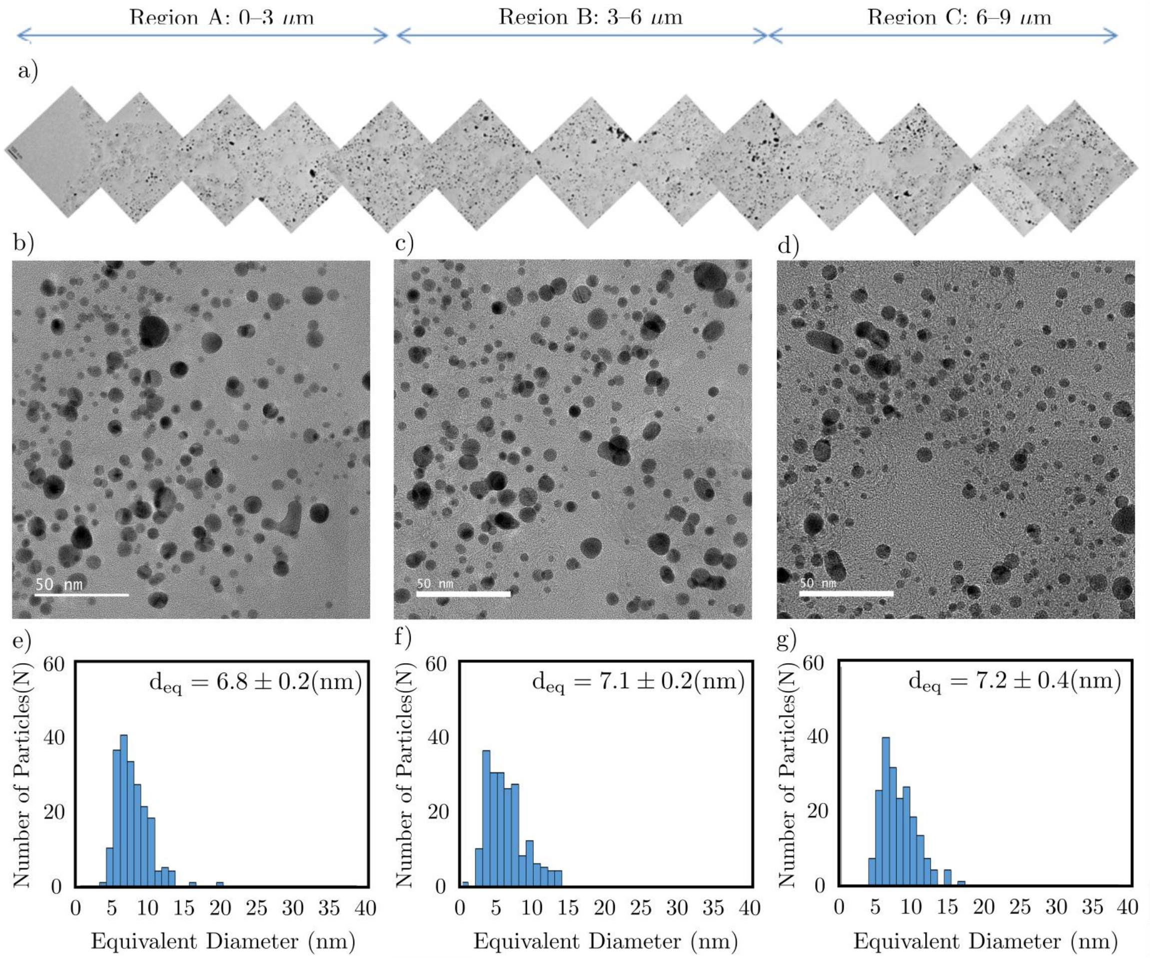

Figure 4-4 TEM Characterization of the cathode area of the low humidity MEA after 10K cycling.

Compared to the powder sample, the PSD of the MEA operated at high potential PSDs at the three different regions within the cathode area illustrate that the high potential sample reaches a mean particle size of approximately 10.5 nm after 10K cycles. has broadened significantly with the majority of particles having sizes greater than 7 nm. Large particles of up to 40 nm were observed in the TEM images of the cathode area after cycling under high potential. Unlike baseline and low humidity samples, there is a significant difference between the mean particle size of region A, B, and C. In region A, which is the closest part in the cathode to the membrane, the particles' diameter grew to 11.8 nm while the ones in regions B and C increased their size to 10.5 and 9.1 nm respectively.

As for the case of the baseline and high potential samples, the MEAs subjected to high temperature also resulted in the growth of particles after cycling. The PSDs in Figure 4-6 illustrate that for this sample a mean particle size of 8.2 nm was achieved. Beyond approximately 10 nm, the PSDs exhibit a tail to larger sizes. Similar to the high potential sample but to a smaller degree the mean particle size is larger in regions closer to the membrane. Regions A, B, and C have particles with the average size of about 9.5, 8.6, and 7.5 nm, respectively.

Figure 4-7 compares the mean particle size in the cycled cathodes (Regions A, B and C combined) operated at different conditions to that of the catalyst powders from which they were fabricated. The change in the mean particle size is found to be more significant for the samples cycled in the higher upper potential limit than the baseline and high temperature, whereas operating at low humidity does not have a significant impact. Cycling

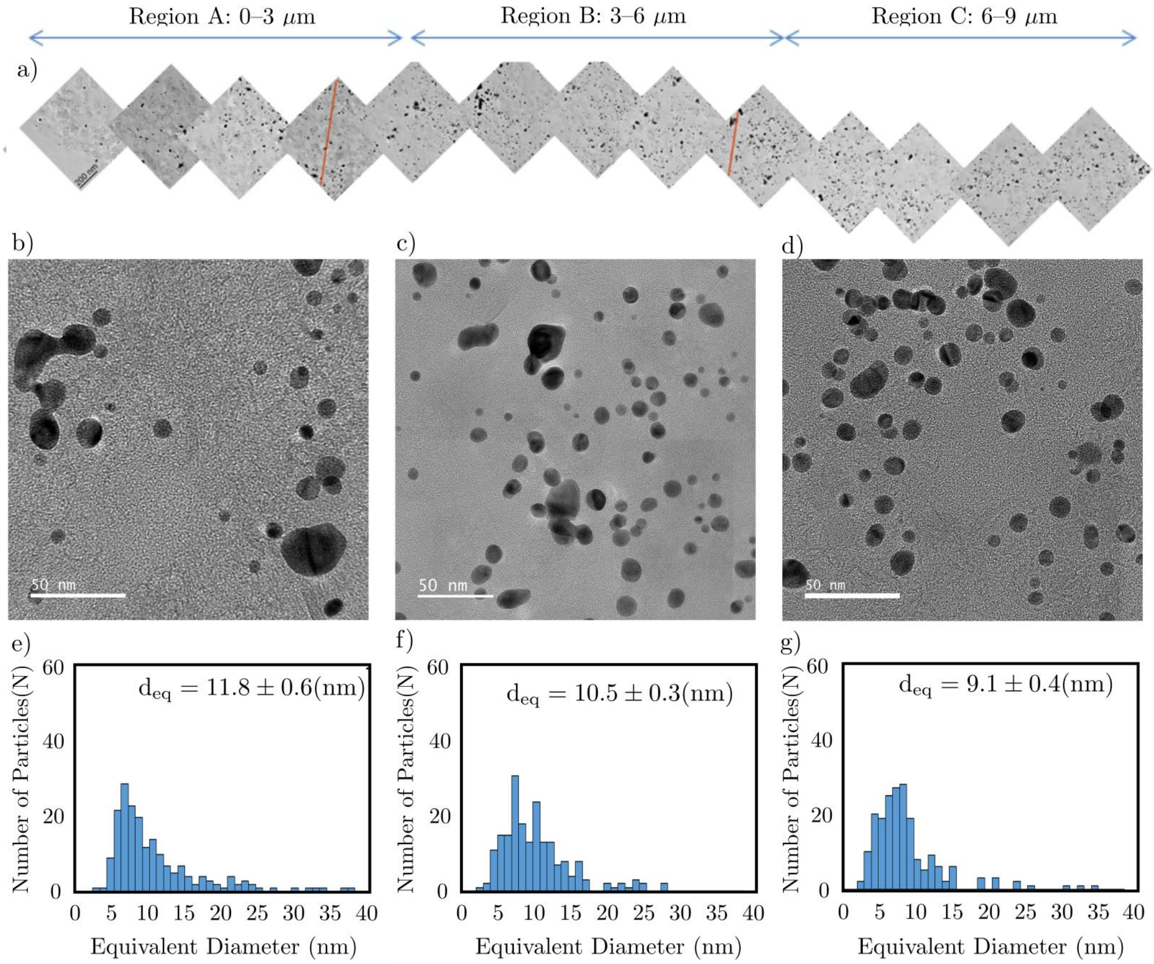

Figure 4-5 TEM Characterization of the cathode area of the high potential MEA after 10K cycling.

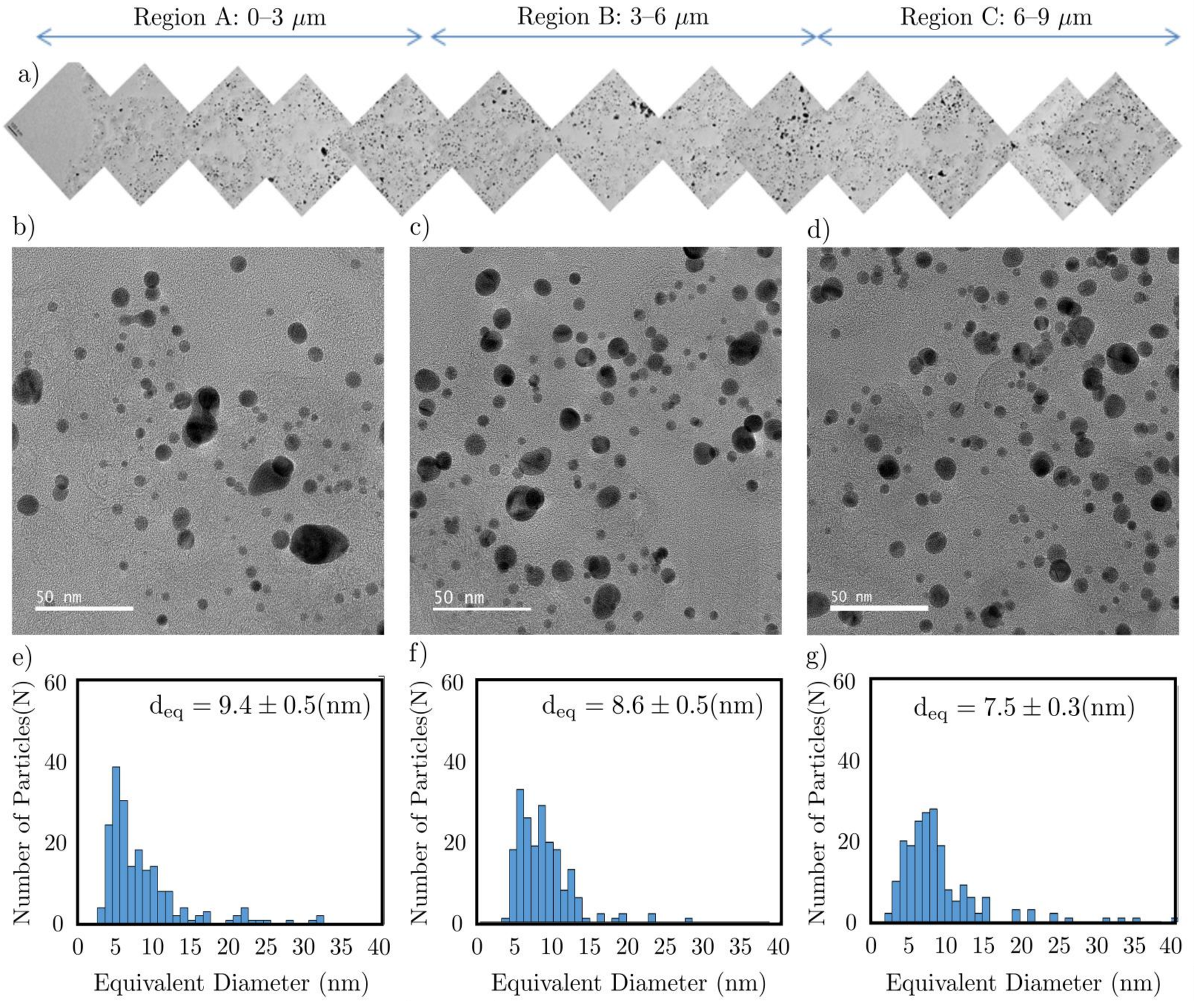

Figure 4-6 TEM Characterization of the cathode area of the high temperature MEA after 10K cycling.

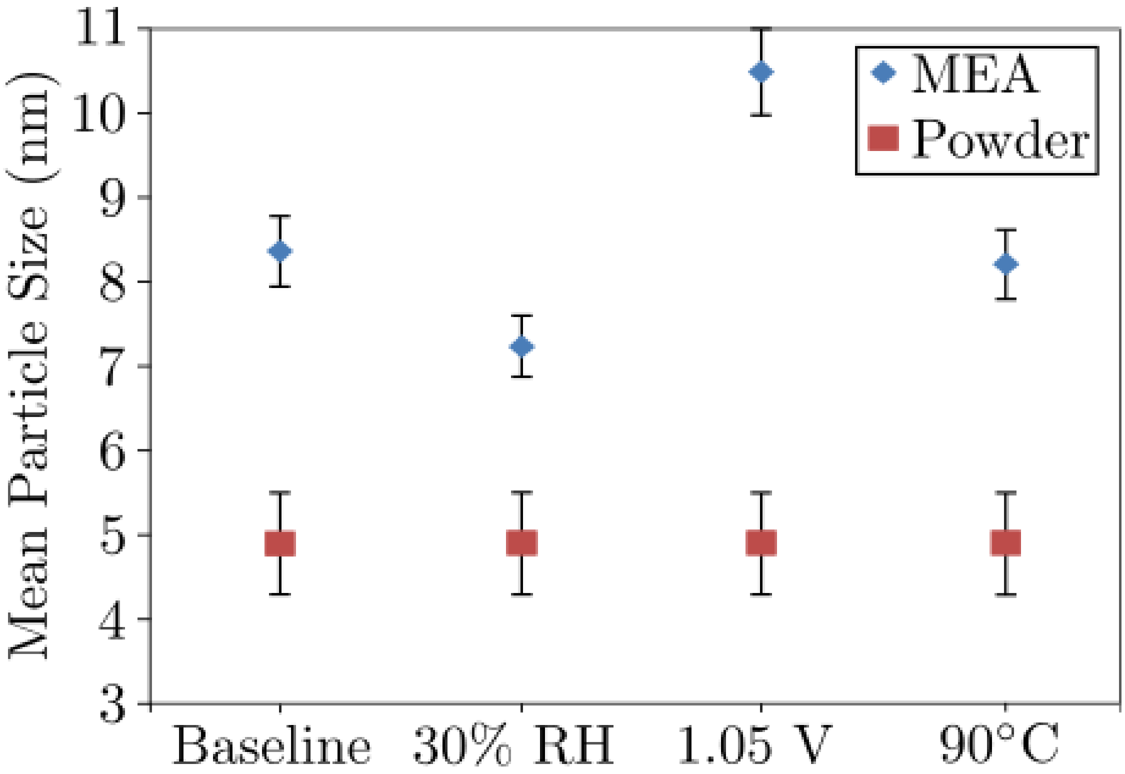

Figure 4-7 Mean particle size after 10K cycling under varied operating conditions.

to a higher upper potential limit results in about 100% increase in mean particle size, whereas cycling under low humidity conditions leads to only 15% increase in mean particle size. The high temperature and baseline samples show a 65% increase in their mean particle sizes.

4.3.2 Particle loss to the membrane

The area percentage of the particles, which is the projected area of the Pt_3Co nanoparticles divided by the total area of the substrate multiplied by 100 is shown in Figure 4-8. It is clear that the high potential sample results in higher particle loss from the cathode than the baseline and high temperature, while the least amount of particle loss occurs in the low humidity MEA. A decrease in the area density of particles represents particle loss from the cathode to the mem- brane which is confirmed by the TEM images of the cathode-membrane interface of the MEAs exposed to deferent operating conditions (Figure 4-9). As for particle loss from the cathode, the precipitation of new particles in the membrane is more severe in the high potential sample than the baseline and high temperature samples, while no significant particle precipitation in the membrane can be observed in the low humidity sample. This is confirmed by the SEM analysis performed by Gummalla et al [12]. Please note that the particle precipitation occurs across the membrane up to 10 µm away from the cathode/membrane interface.

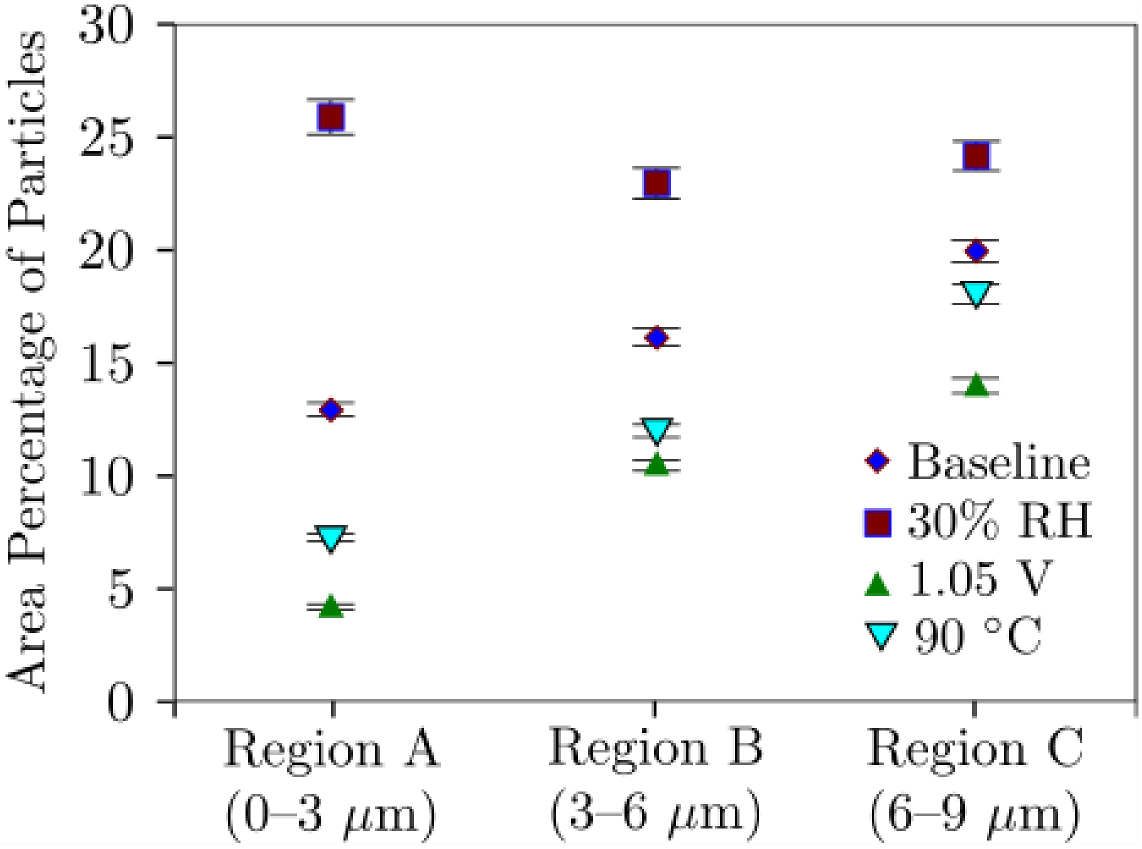

Figure 4-8 Area percentage of the particles in three different regions in the cathode after 10K cycles.

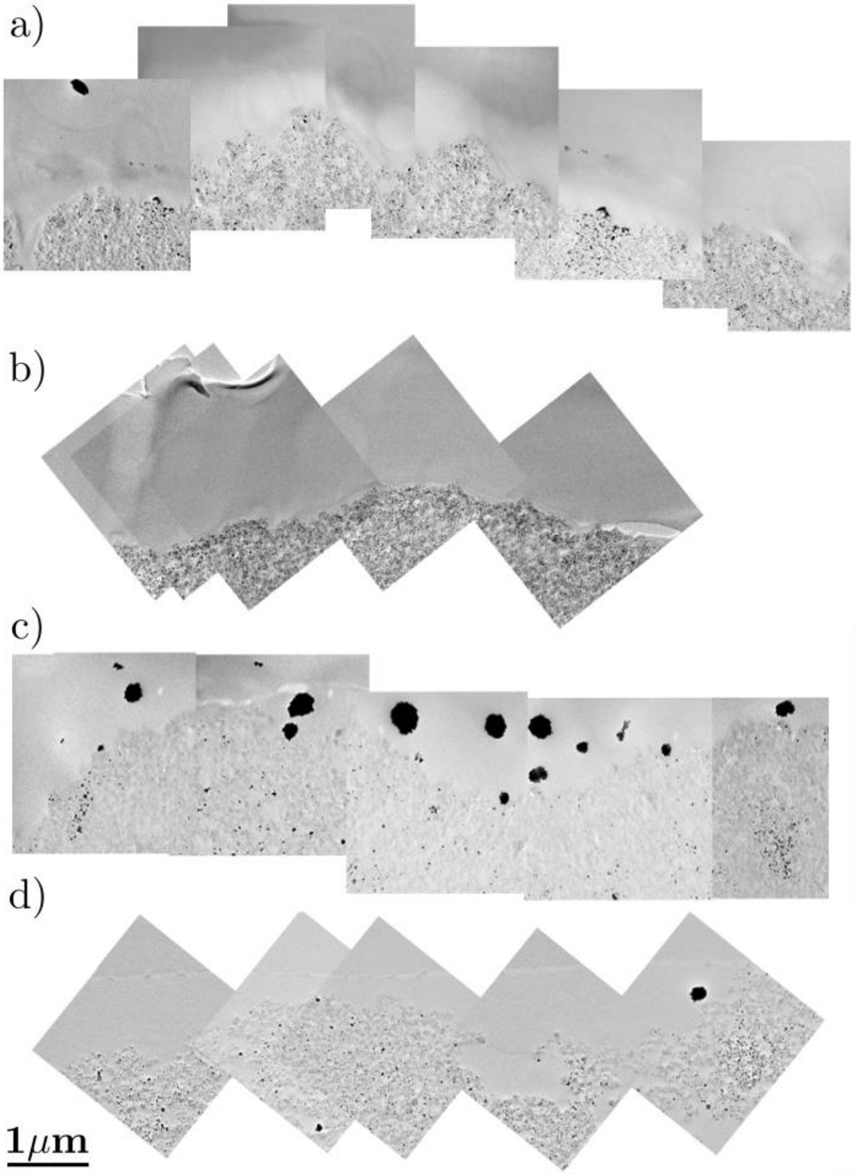

Figure 4-9 TEM bright field images of the nanoparticles in the cathode, and the cathode-membrane interface after 10K cycling under a) baseline; b) 30% RH; c) 1.05 V d) 90 C.

4.4 Discussion

Let us now discuss the trends in mean particle size, particle loss from the cathode, and particle precipitation in the membrane under different operating condition. The largest particle size, the highest amount of particle loss from the cathode and the largest particle precipitation in the membrane occur under high potential operating condition, while the contrary is true for the low humidity condition. The baseline and high temperature operating conditions remain somewhere in the middle. Since both high potential and humidity affect particle dissolution and/or ion diffusion, the fact that potential and humidity have the highest impact on the mean particle size and particle loss from the cathode to the membrane indicates the critical role of particle dissolution and ion mobility on the surface area loss mechanisms of the NPs. Indeed, large particles in the membrane are indicative of Pt_3Co dissolution and re-precipitation in the membrane by chemical reduction of dissoluble Pt due to hydrogen crossover molecules, which results in Pt loss from the cathode area. The fact that Pt loss to the membrane is more severe in the high upper potential limit than for the other conditions is explained by the accelerated dissolution rate at potentials higher than 0.95 V [7], [59], [98]. The effect of the humidity on Pt dissolution and Pt ion transport in the ionomer has been studied by Bi et al [87]. Under high humidity conditions, the polymer electrolyte exhibits large and abundant water channel networks. This is analogous to the effect of humidity on the proton conductivity of the Nafion electrolyte, as the higher water content in the Nafion electrolyte results in higher mobility of protons in the membrane. Accordingly, low humidity conditions limit the Pt and Co ion diffusion, which consequently restricts Ostwald ripening in the cathode area, as well as re-precipitation of Pt crystals in the membrane. On this basis, we can conclude that to restrict the degradation of catalysts on the cathode of the MEAs, it is critical to control the Pt dissolution and Pt ion diffusion to minimize Ostwald ripening, as this is a critical mechanism of particle growth and surface area loss inside the cathode.

Another important observation is the inhomogeneity inside the cathode in terms of particle size and particle loss from the cathode. In the case of particle size, although the differences in the mean particle size of regions A, B, and C are negligible for the baseline and low humidity samples, the situation is different for the high potential and high temperature samples. In the last two cases, the increase in particle size is greater in regions closer to the cathode-membrane interface than that of areas far from the interface. Specifically, the mean particle size in region A is about 2.7-0.7 and 1.9-0.5 nm larger than that of region C for the high potential and high temperature samples, respectively. Since particle mobility should be the same in each region of the cathode [7], particle migration and coalescence should not be responsible for the larger particle size in the areas closer to the cathode-membrane interface. This inhomogeneity can be explained by considering the particle dissolution and re-deposition as the dominant mechanism for the nanocatalysts growth inside the cathode. The Pt ion concentration gradient and potential difference between the cathode and anode results in Pt ion transport in the cathode toward the membrane [99]. Among these Pt ions, a fraction will deposit on nearby particles, while the remainder will move longer distances toward the membrane and re-deposit on particles in regions near the membrane.

This inhomogeneity is also observed in the amount of particle loss from different regions of the cathode toward the membrane. Under all operating conditions, the amount of particles remaining in the cathode decreases as the distance to the membrane-cathode interface decreases (Figure 4-8). As shown in the SEM analysis of these samples [12], the particles precipitated at the center part of the membrane show that the soluble Pt species move half way through the membrane, where they are reduced by the hydrogen crossover permeated through the membrane from the anode to the cathode. The concentration of soluble Pt in the cathode decreases from the cathode/DM interface to the center part of the membrane where the crossover hydrogen chemically reduces Pt soluble ions to platinum particles. Fickian diffusion law can explain the reason why the amount of particle loss increases in regions closer to the membrane. By assuming that there are no Pt2+ ions at the center part of the membrane, next to the Pt band, the flux of soluble Pt species from the cathode toward the anode (N_{Pt}) can be estimated by means of a Fickian semi-infinite one dimensional diffusion, according to the expression:

$$N_{Pt} = D_{eff}\frac{C_{Pt}}{L} \tag{4.1}$$

where D_{eff} is the effective diffusivity of Pt ions in the membrane, C_{Pt} is the equilibrium Pt ion concentration in the cathode and L is the distance from each region in the cathode to the last Pt band in the membrane. The Pt flux from different regions in the cathode to the membrane at the micrometer scale is inversely proportional to the distance between the region and the last Pt band in the center of the membrane. Thus, the Pt loss is more severe in the regions closer to the cathode-membrane interface in the cathode.

4.4.1 Compositional and morphological analysis in the cathode

To study the composition changes in the cathode, two types of EDS measurements were performed. First, we measured the variation of Co across the cathode in nine different areas of 1µm diameter each. For this purpose, the electron beam was spread to 1µm diameter to cover a wide area of the sample. Second, a more detailed compositional analysis of individual and coalesced particles was performed with the electron beam matching the size of each particle to cover the entire particle. Figure 4-10 shows the Co atomic percentage along the different areas in the cathode of the Low RH, high upper potential and high temperature MEAs, as a function of distance from the cathode-membrane interface. The atomic percentage of Co in all MEAs is below the Pt:Co 3:1 ratio of the initial Pt_3Co particles. The Co concentration in Low RH and baseline MEAs is almost constant throughout the cathode with small variations. However, a higher variation of Co concentration is identified in the MEAs subjected to high voltage and high temperature operating conditions. In the last two cases, The highest amount of Co loss is seen in the areas very close to the membrane (Region A), while away from the membrane (Region B), the amount of Co in the cathode is increased. Moving farther toward the cathode-DM interface (Region C), results in a decrease in the amount of remaining Co in the cathode. To understand this Co variation, we should consider the two types of particles, based on their morphology, present in the cathode, namely individual spherical particles and aggregated non-spherical particles.

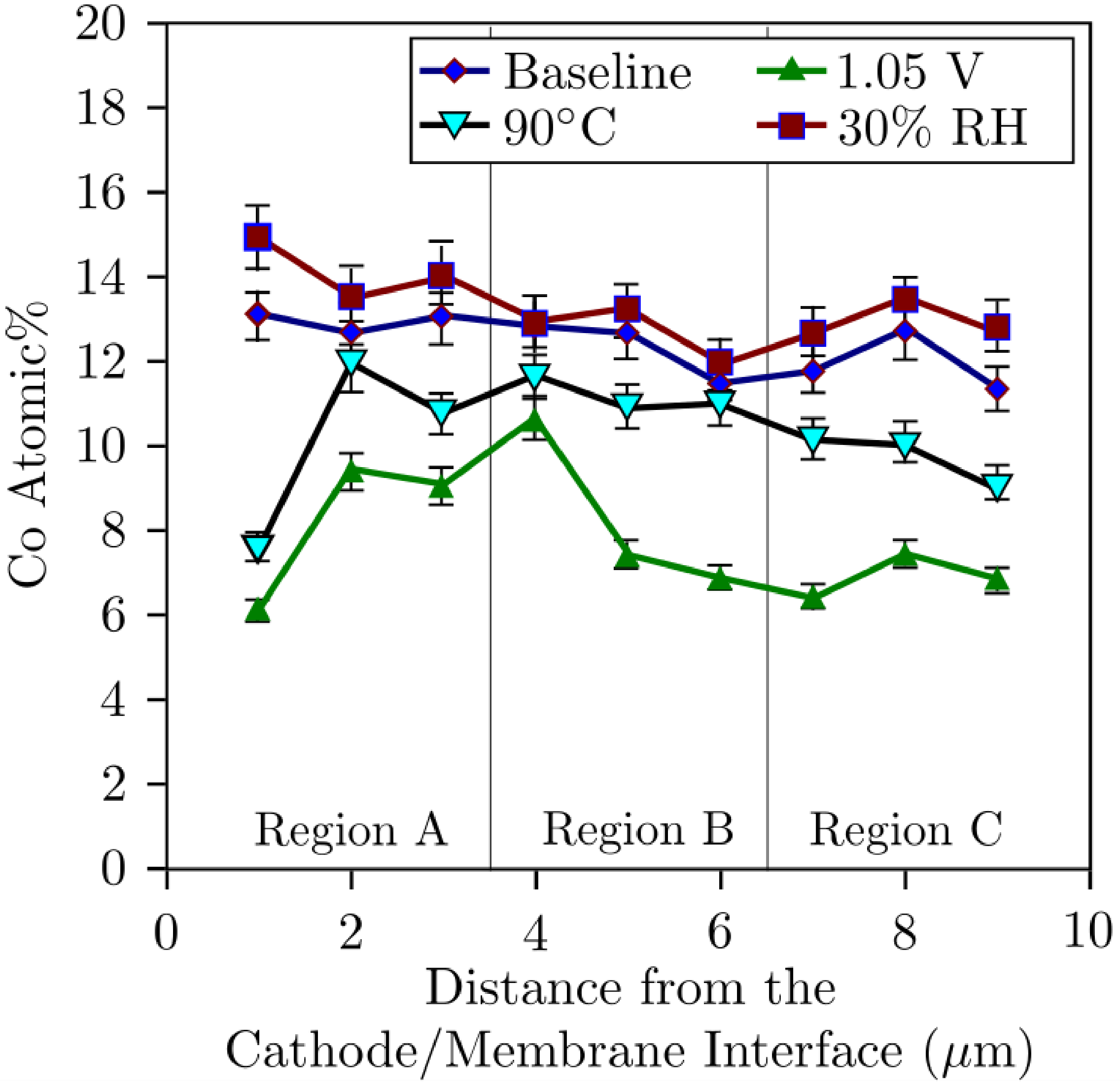

Figure 4-10 Cobalt atomic percentage in different areas of the cathode of the MEAs.

In terms of individual spherical particles, this morphology is the result of either growth via electrochemical Ostwald ripening or shrinkage due to the dissolution of Pt and Co into the ionomer phase, as both are isotropic processes. Figure 4-11 shows the Co concentration of individual spherical particles vs particle size in the powder sample as well as low humidity, high temperature, and high voltage MEAs obtained from EDS. All of the cycled MEAs show lower Co contents than the starting powder sample at any given particle diameter. For the Co at% we can observe a clear trend in the experimental conditions, with 1.05 V >90℃ > baseline ~ 30% RH. This is a result of the particle dissolution rate, which follows the same trend. Even though this is not measured directly, we can infer this from the observations of the particle loss and particle precipitation in the membrane, which is Zalso supported by the literature. The effect of particle size on the Co concentration is similar for all the operating conditions. The Co atomic percentage of the spherical particles increases with increasing the particle equivalent diameter. As it has been observed in previous studies, Co leaching from the Pt_3Co particles occurs preferentially from the outermost layers of the particles, resulting in the formation of Pt enriched surfaces [11], [75], [83]. Thus, decreasing the fraction of atoms present on the surface for the larger particle sizes results in less Co leaching for these particles. In addition, re-deposition of Pt atoms on the surface of larger particles through Ostwald ripening during voltage cycling is expected to increase the thickness of the Pt enriched surface thus reducing the Co leaching to the ionomer. However, in high potential sample, the lower fitting (R-square value) especially for the particles with intermediate sizes might be related to the severe dissolution

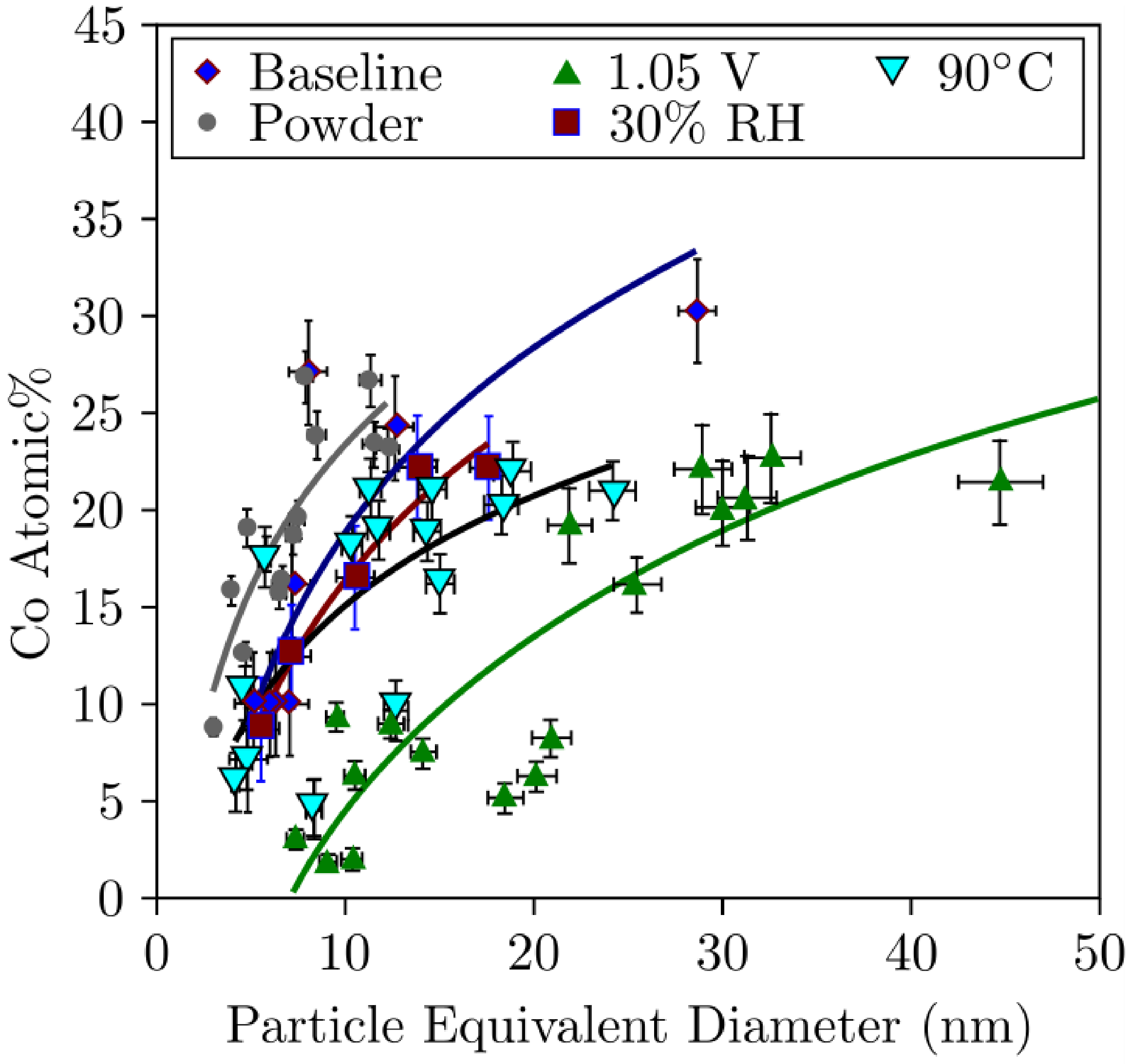

Figure 4-11 Co atomic percentage of individual spherical particles vs particle size after 10K voltage cycles under different operation condition.

of Co and Pt which occurs under potentials higher than 0.95 V. This, in turn, might prevent the passivating Pt rich layer on these particles from protecting the particles from Co leaching.

Regarding the non-spherical particles, these arise from the aggregation and coalescence of various particles. The particles are considered to be non-spherical aggregated coalesced if their roundness, R, are smaller than 0.8. The parameter R is defined in terms of its projected area A and the major axis (a) of an ellipse fitted to the particle outline, according to the expression

$$R = 4Aa^2 \tag{4.2}$$

The projected area percentage of non-spherical aggregated-coalesced particles was calculated from the ratio of the projected area of non-spherical coalesced particles ($A_{\text{coalesced}}$) to the total projected area of all particles ($A_{\text{individual}}$ + $A_{\text{coalesced}}$) in the cathode.

The data set used in the particle size analysis, i.e. 200 particles from each region and a total of 600 particles for each MEA, was also used for the quantification of the amount of coalescence. Note, that we cannot simply count the number of coalesced particles, as this approach ignores the amount of particles participating in coalescence. Thus, even though there is a small bias towards large particles, the introduced error is much smaller than the error we would get by considering the number fraction of particles. The trend in this value is almost the same as the trend in particle size growth (1.05V > 90°C > baseline > 30% humidity). Operating under the high upper potential limit results in the most severe surface area loss due to aggregation-coalescence with about 38% coalesced particles in the cathode. Coalescence also occurs in the cathode operated at high temperature with about 31% of coalesced particles, compared to the baseline with 23%. However, the low humidity sample contains only 8% of aggregated coalesced particles. Under all operating conditions, the coalescence of particles inside the cathode happens more severely in the regions closer to the membrane, except for the low humidity sample which shows a constant trend across the cathode (see Figure 4-12).

The highest and lowest percentage of coalesced particles in the high potential and low humidity samples, respectively, in addition to an increased amount of coalescence inside the cathode closer to the membrane, shows the critical role of particle dissolution and diffusion in the formation of such morphology. Accordingly, besides particle migration, which might also occur, two mechanisms can be suggested for particle coalescence:

Deposition of dissoluble Pt between two particles with consequent bridging

This mechanism is supported by the work of Carlton et al. who observed some evidences of preferential deposition of Pt on the particles surface close to nearby particles [100]. This preferential deposition can finally lead to bridging between two particles and coalescence of those particles. Moreover, Asoro et al. [67], [101] provided some evidences of coalescence via deposition of Pt clusters between two or more adjacent particles in their in-situ heating TEM experiments. Figure 4-13a-d shows bright-field TEM images of coalesced particles in the baseline, low RH, high voltage, and high-temperature cathode samples showing Co concentrations of less than 3 at%. Due to the low Co/Co^{2+} redox potential and low enthalpy of mixing of Pt-Co, re-deposition of Co ions on the particles is not thermodynamically favorable [11], [102]. Accordingly, the low Co concentration in the particles shown in Figure 4-13a-d seems to confirm the proposed mechanism of coalescence by preferential deposition of Pt between two or more adjacent particles. As shown in the TEM images, the low Co concentration (less than 3 at%) is characteristic of this mechanism.

2-Modified electrochemical Ostwald ripening until adjacent particles make contact with each other and coalesce

These particles are formed by necking between spherical particles, which had already grown by Ostwald ripening. Hence, the Co concentration in these particles is the average of the particles before necking. For example, consider the coalesced particle in Figure 4-13f, which is the result of necking between two spherical particles of about 27 nm and 23 nm under baseline operating condition. According to Figure 4-11 the average Co at% of particles of that size is roughly between 30% and 35%. This is remarkably close to the composition of the coalesced particle shown in Figure 4-13f, which is 30.1 Co at%. In other words, the fact that the Co concentration in these particles is similar to the Co concentration of individual spherical particles with the same size validates this proposed mechanism. Note, that the argument about Co at% does not hold true for particles formed through the former proposed mechanism (preferential deposition and particle bridging), so we can use the Co concentration to differentiate between these two mechanisms. Figure 4-13e-h are examples of coalescence via this mechanism.

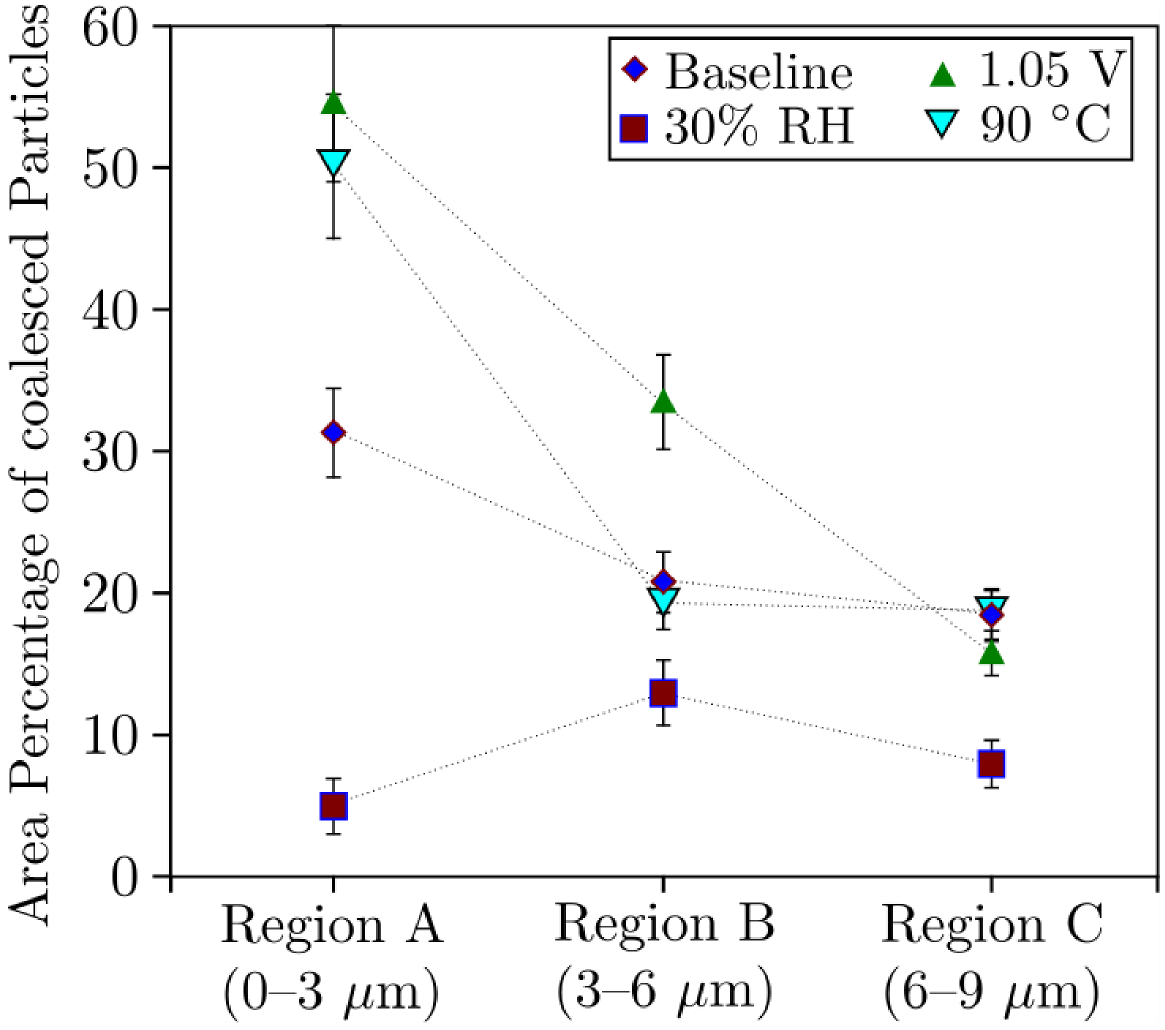

Figure 4-12 the Area percentage of coalesced particles in regions A, B and C of the MEAs after 10K voltage cycles under different operation conditions.

With this information we can now explain the reason for the variations of Co through the cathode from the cathode/membrane to the cathode/DM interface in the high potential and high temperature samples (Figure 4-10). The amount of Co in the cathode is associated with the Co present in individual spherical particles, as well as the Co in aggregated particles, which results from the aforementioned mechanisms. As we discussed before, for these two conditions, the mean particle size as well as the amount of coalesced particles inside the cathode increase as the distance to the membrane decreases. In order to understand if an increase in the mean particle size is merely due to the increase in the amount of coalesced particles, which are typically larger particles, the mean diameter of the spherical particles (with R> 0.8) in regions A, B and C of the high potential and high temperature samples were quantified. This figure for the high potential sample is 9.4, 10.0 and 8.1 nm, and for the high temperature sample is 7.8, 8.1, and 7.1 nm in regions A, B, and C, respectively. Thus, the reason for the increase in the Co at% from region C to region B seems to be due to the presence of larger spherical particles which contain more Co according to Figure 4-11. Inside region A however, the amount of Co declines significantly due to the proximity of the membrane. Since the mean diameter of the individual spherical particles in region A is not statistically different from that of region B, and considering the fact that more than 50% of the particles in this region are non-spherical coalesced ones (Figure 4-12), the coalesced particles seem to be responsible for the decline in Co at% inside region A. One can infer that most the coalesced particles in this region result from deposition of dissoluble Pt between two or more particles and consequent bridging (the

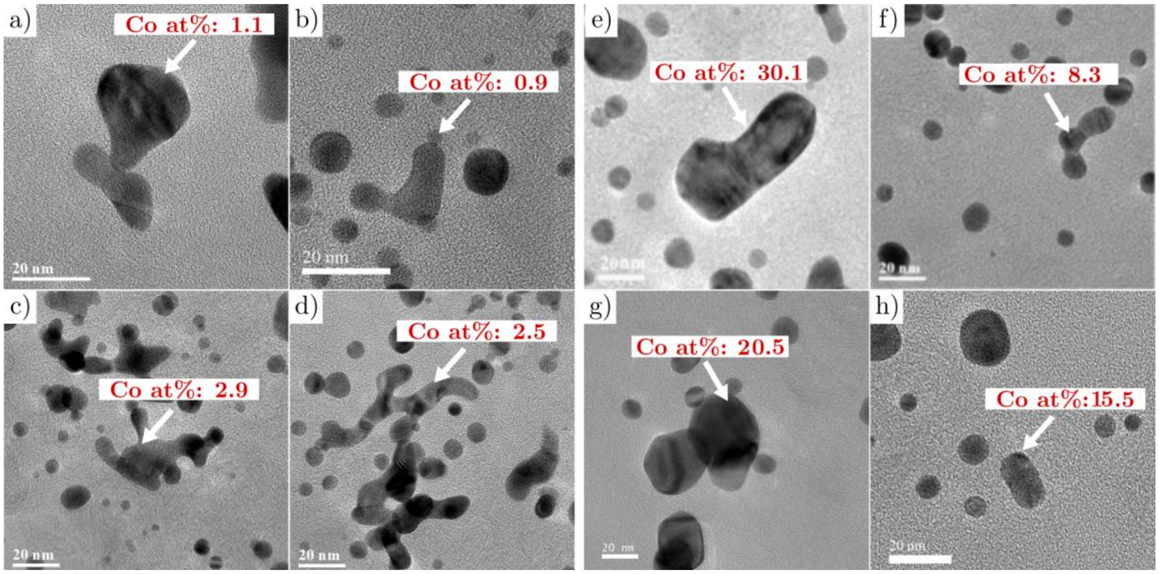

Figure 4-13 TEM images and corresponding Co at% of the coalesced particles formed by deposition of Pt between particles with consequent bridging after 10K voltage cycles under a) baseline, b) low humidity c) high voltage and d) high temperature, as well as TEM images and corresponding Co at% of the coalesced particles formed by necking of the spherical particles after 10 K voltage cycles under e) baseline, f) low humidity g) high voltage and h) high temperature.

second proposed mechanism), which contain considerably low amount of Co. Considering the fact that the highest amount of particle loss occurs in this region (Figure 4-8), it seems that Co and Pt diffuse to the membrane, but only Pt species, coming from regions B and C, deposit between particles. This, in turn, results in the dramatic decline in Co concentration inside region A.

4.4.2 Compositional and morphological analysis in the membrane

To better understand the precipitation of particles in the membrane, a more careful TEM observation of those particle was made in the high potential MEAs. Figure 4-14 in the supporting information illustrates the particles precipitated in the membrane which includes larger particles close to the cathode-membrane interface and smaller ones far from the interface. It Seems that the larger particles, located in the areas close to the cathode/membrane interface, are dendritic and polycrystalline in nature (Figure 8a), while the smaller ones formed far from the interface are single crystals (Figure 8b). This can be explained by the inhomogeneity in driving force (supersaturation). In the region nearby the cathode/membrane interface, the concentration of Pt ions is relatively high and non-uniform along the growing surfaces. In this case, interfacial kinetics of Pt reduction and re-deposition of Pt atoms onto an atomically rough surface is faster than the diffusion of Pt species on the surface of the particles [99]. On the other hand, far from the cathode-membrane interface, but still in the membrane, faceted type Pt shapes are dominant because diffusion of Pt ions in the ionomer to the faceted Pt nanoparticles is fast, relative to interfacial kinetics of Pt addition on the growing faceted surfaces. Additional EDS analysis of both types of particles show that they are pure Pt and do not contain Co (Figure 8a and b). Co remains in cationic form after Pt_3Co dissolution, while Pt^{2+} is reduced to metallic Pt by crossover H_2 within the membrane ionomer. Dissolved Co ions cannot be reduced by crossover hydrogen because the reduction potential of Co/Co^{++} is less than that of H_2/H^+ and the enthalpy of mixing of Pt and Co is too small, therefore Co ions remain in the ionic form in the membrane.

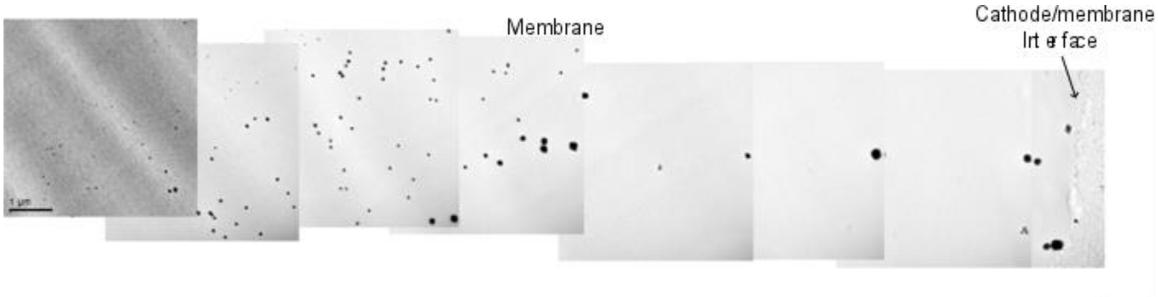

Figure 4-14 TEM images of the particles precipitated in the membrane after 10 K cycles under high potential operating condition.

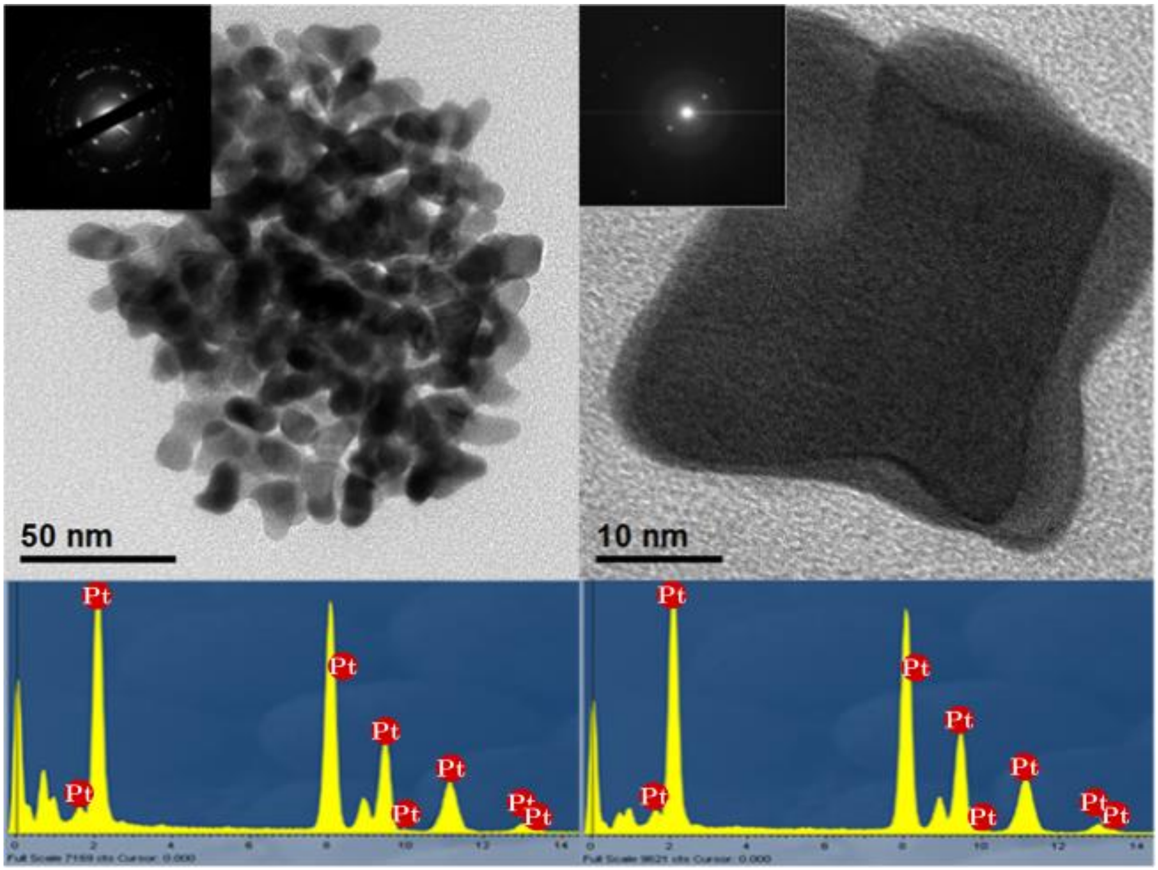

Figure 4. Figure 4.15 Particles precipitated in the membrane: TEM images, diffraction pattern (insets) and EDS analysis a) close to the interface and b) far from the interface after 10K cycles under high potential operating condition.

Chapter 5: Identical location TEM on PT Nanocatalysts

5.1 Introduction

To better understand and obtain direct evidence about each of the degradation mechanisms discussed previously, the focus of this chapter is to determine the behavior of Pt NPs at different stages of fuel cell potential cycling. Ideally, voltage cycling of the MEAs would be performed in-situ inside a TEM, but these experiments are extremely challenging due to the need for simultaneous but separate presence of the gas phase reactants. Hence, the closest approach to an in-situ experiment is to perform identical location TEM experiments. For this purpose, a set-up was developed to replicate on a TEM grid the effect of voltage cycling on the cathode side of the fuel cell outside of the microscope. Using this approach, it was possible to track the behavior of single NPs at different stages of potential cycling at the nano/atomic scale. These identical location TEM experiments provide a unique insight into the mechanisms of degradation in PEMFCs.

In this chapter, the degradation mechanisms of Pt nanoparticle catalysts supported on carbon nanotubes, as well as Pt NPs supported on amorphous carbon are investigated by aberration corrected TEM, before and after voltage cycling. The reason why carbon nanotubes are used for the first part of this work is due to their simpler morphology, compared to the complicated 3-D morphology of carbon black. The convoluted 3-D structure of carbon black makes it difficult to interpret the actual location of the NPs on the carbon support from the 2D projected TEM images.

Performing these experiments on Pt NPs supported on carbon black and carbon nanotubes (CNTs) may verify if and how an applied voltage results in particle movement and how single atoms and atomic clusters play a role on the coalescence of NPs.

5.2 Experimental

Pt NPs on poly(vinylphosphonic) acid-doped polybenzimidazole (PVPA-PBI) wrapped on carbon nanotube was synthesized by Nakashima group at Kyushu University. The synthesis method is explained in reference [102]. Briefly, poly[2,2′-(2,6-pyridine)-5,5′-bibenzimidazole] (PyPBI) non-covalently wrapped the surfaces of multi-walled carbon nanotubes (MWNTs) through a strong physical interaction, then Pt particles with a diameter of 3.2 ± 0.62 nm were immobilized onto the PyPBI layer. The obtained composite (MWNT/PyPBI/Pt) was doped with PVPA through a simple mixing of the MWNT/PyPBI/Pt with PVPA in an aqueous solution, and the PVPA doped composite (MWNT/PVPA-PyPBI/Pt) was obtained after removing the unbound PVPA by vigorous water rinsing [102]. PVPA wraps the electrocatalysts and serves as the ionomer or ion conducting phase. Figure 5-1 shows a schematic of the different steps of the synthesis method.

For Pt NPs supported on amorphous carbon, catalysts were prepared by Johnson Matthey, at 40%wt Pt loading on Akzo Nobel Ketjen EC300J via proprietary methods, with a subsequent annealing to produce the NPs with 3.2 nm mean particle size.

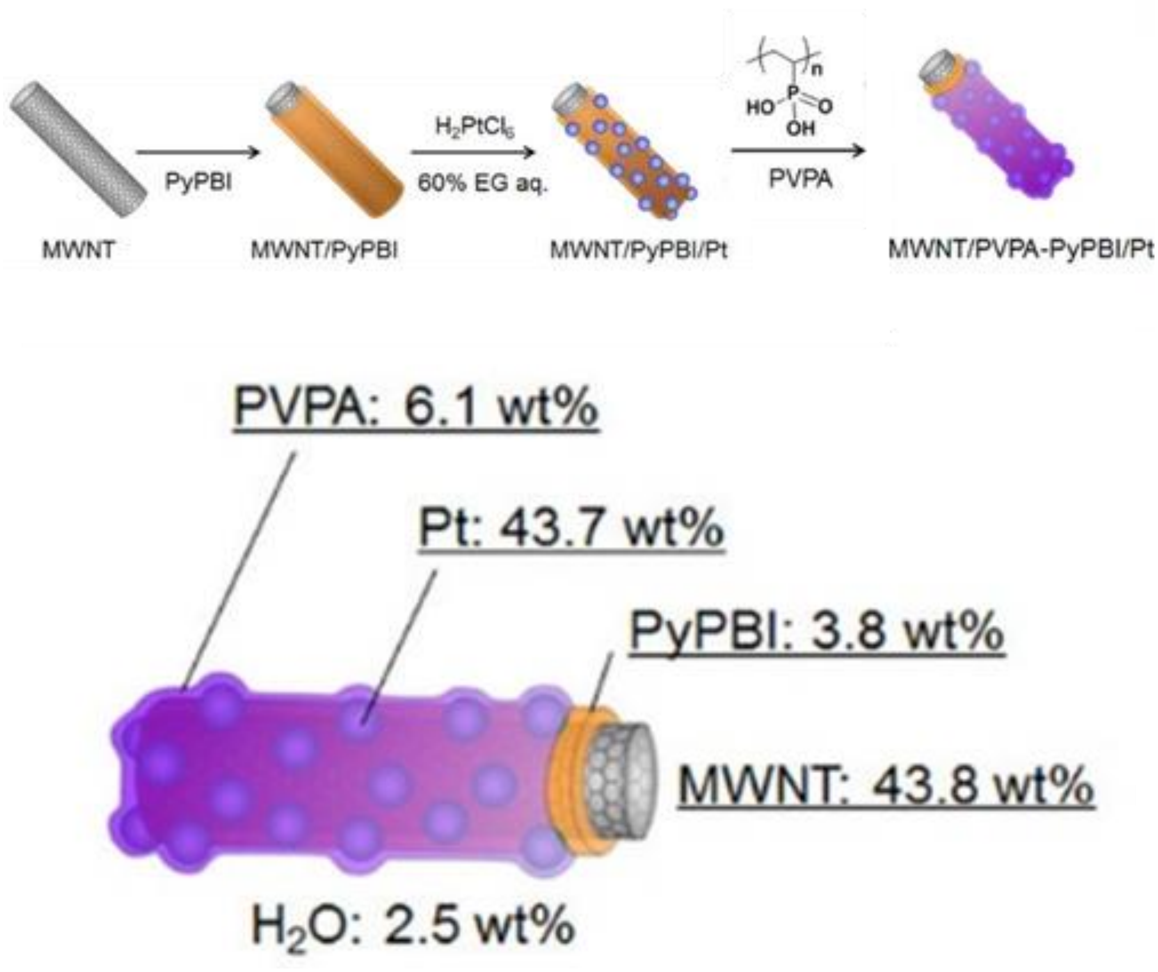

Figure 5-1 Schematic illustration of the preparation technique of the MWNT/PyPBI-PVPA/Pt.

In order to assess the degradation of fuel cell components including the catalyst NPs several accelerated stress test (AST) protocols have been previously developed [14], [43], [44]. These ASTs can be performed either in situ in PEMFCs (single-cell) or ex situ in a classical three-electrode electrochemical cell using liquid electrolytes (half-cell) [14], [43], [45], [46]. Although the durability test in PEMFCs provides an invaluable insight into the degradation of the fuel cells, it is difficult to separate the contribution of other components such as membrane and gas diffusion layer. ASTs in three-electrode electrochemical cells have the advantage of being less expensive and allow the ability to provide controlled information on the degradation of the catalytic layer excluding any contribution from other parts of the PEMFC. In fact, several studies have shown a good agreement between the ECA loss mechanisms and half-cell durability tests [10], [48], [49]. On this basis, the voltage cycling of the catalysts NPs in this work was performed in a half-cell in the presence of liquid electrolyte, instead of a single cell (MEA) with solid electrolyte.

More specifically, to investigate the effect of voltage cycling on the NPs, the electrocatalyst materials (Pt supported on ionomer wrapped CNT and Pt supported on CB) are first dispersed in ethanol, ultrasonicated and deposited on a quantifoil holy carbon gold TEM grid. The location of the ROI was recorded by taking several images at different magnifications. In the next stage, the TEM grid attached to a gold plate was used as a working electrode in a three electrode electrochemical compartment cell. A Pt wire and saturated Ag/AgCl electrodes were used as the counter and reference, respectively. All potentials shown in this paper are given with respect to the reversible hydrogen electrode

(RHE) potential. The TEM grid was cycled between 1 and 1.5 V vs. RHE in N_2-saturated 0.1M $HClO_4$ liquid electrolyte with the sweep rate of 0.5 V/sec. After voltage cycling, the TEM grid was rinsed and dried, and then transferred to the microscope. Using the recorded location of the ROI, aberration-corrected TEM images of the same NPs in the ROI were taken and compared with the images obtained before potential cycling. Aberration corrected JEOL JEM-ARM 200f operated at 200 kv and and FEI Titan operated at 80 kv were used for TEM observation.

5.3 Results and Discussion

5.3.1 Pt NPs supported on Carbon Nanotubes

During the first 1000 voltage cycles we found that the main mechanism for the loss of electrochemical active surface area is particle motion, followed by coalescence. This is clearly shown in Figure 5-2a where two well separated NPs on the surface of a CNT (yellow square 1), move until they contact each other and finally coalesce (Figure 5-2b). Changes in orientation of individual NPs were also observed after voltage cycling (compare the NP in yellow square 2 in Figure 5-2a and b), as confirmed by the FFTs shown in the insets. Figure 5-2c depicts another region of the CNTs, where six individual particles (yellow square 3) with different orientations (FFTs show in insets) are close to each other. During voltage cycling, the particles moved towards each other until they impinge on each other and coalesce. In order to lower their total interfacial energy, particle rotation occurred (FFT in the inset of Figure 5-2d), leading to the formation of a larger single crystal particle.

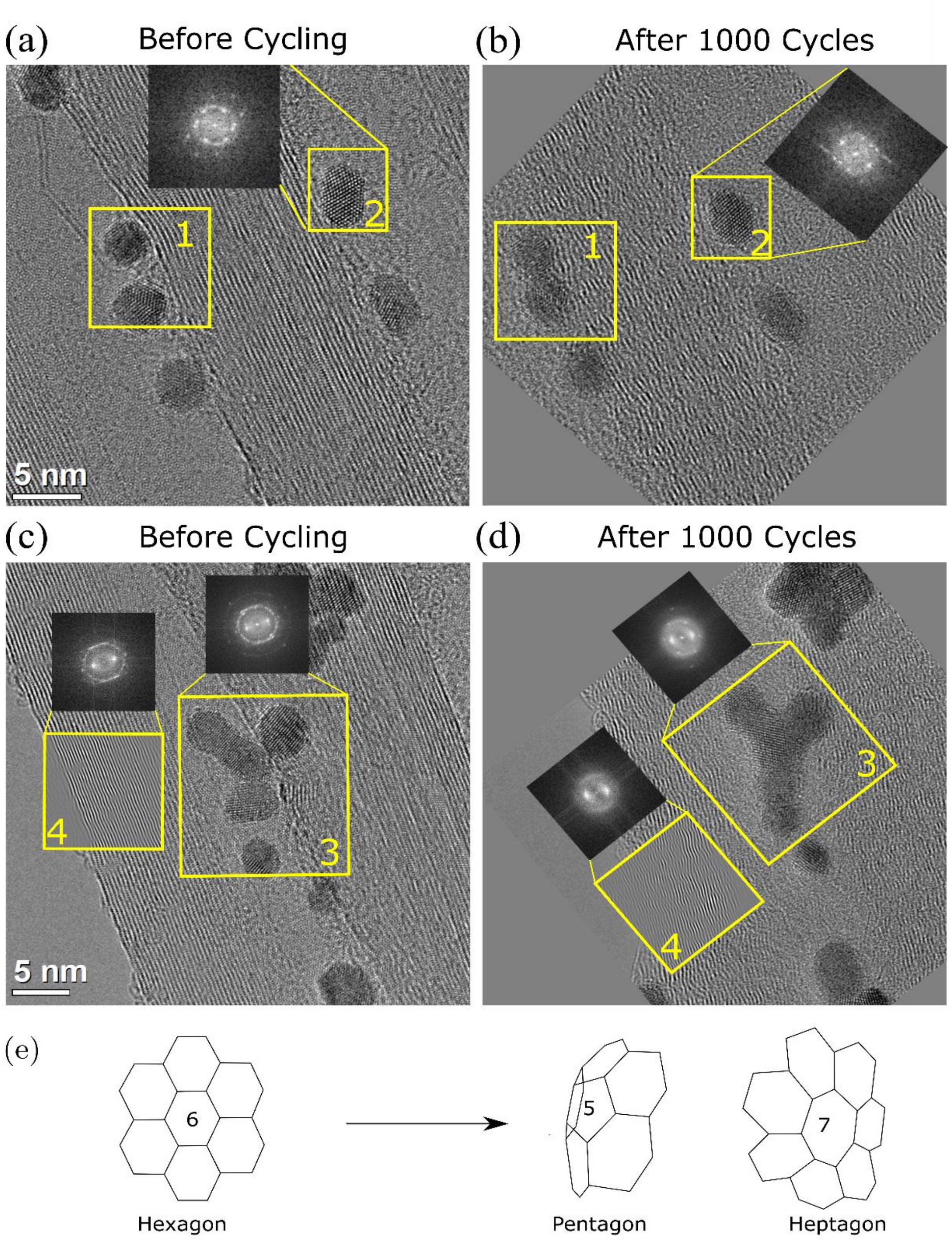

Figure 5-2 Aberration corrected TEM images of the Pt nanoparticles on carbon nanotubes a) and c) before, b) and d) after 1000 potential cycling, e) schematic of the change in the structure of carbon ring.

Another important observation upon cycling is the severe structural deformation of the CNTs. As shown by the inverse filtered FFTs of the phase contrast TEM images displayed in square 4 of Figure 5-2c and d, the typical layered structure of the multi-walled CNTs became wavy-like after voltage cycling, due to the formation of point defects in the CNTs. Specifically, carbon atoms were removed from the lattice, which converts their hexagonal arrangement to heptagon and pentagon carbon rings, thus bending the atomic planes (Figure 5-2e) [103].

In order to understand the structural damage of CNTs, as well as particle motion under voltage cycling, we need to look into the mechanism of carbon corrosion. Figure 5-3 shows the schematic of a Pt NP supported on a CNT, wrapped in ionomer. Three interfaces are noted, namely the carbon/ionomer, ionomer/particle, and carbon/particle interfaces. As a consequence, three sets of reactions may occur at these interfaces.

First, consider the carbon/ionomer interface where the carbon surface consists of defect sites (C*) that are prone to reversible electrochemical oxidation, leading to unstable C-OH groups at a potential of E =0.2 V. This reaction can be written as

$$C^* + H_2O \leftrightarrow C - OH + H^+ + e^- \qquad E = 0.2\,V\,RHE \tag{5-1}$$

The unstable C-OH group can be further oxidized to form a stable double-bonded C=O group at a potential of E =0.8 V, through the following reversible reaction:

$$C - OH \leftrightarrow C = O + H^+ + e^- \qquad E = 0.8\,V\,RHE \tag{5-2}$$

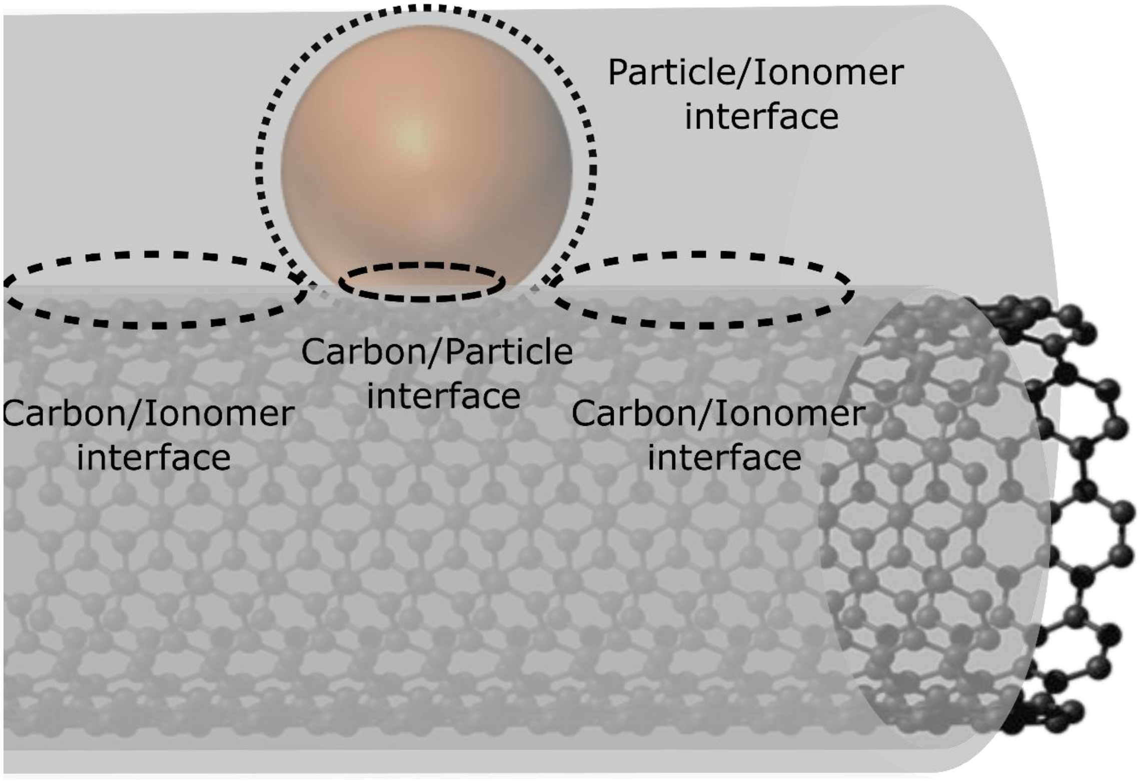

Figure 5-3 Schematic of carbon/particle/ionomer interfaces

At a higher potential of E= 0.95 V, the unstable C-OH group is oxidized to form carbon dioxide, leaving behind a defect site. This reaction can be described as:

$$C - OH + H_2O \leftrightarrow C^* + CO + 3H^+ + 3e^- \qquad E = 0.95\, V\, RHE \qquad (5\text{-}3)$$

Next, we should consider the platinum oxidation reactions, which occur at the particle/ionomer interface, with $Pt(OH)_{ads}$ acting as an intermediate. Specifically, we have the following two reactions

$$Pt + H_2O \leftrightarrow Pt(OH) + H^+ + e^- \qquad E = 0.7\, V\, RHE \qquad (5\text{-}4)$$

$$Pt(OH)_{ads} \leftrightarrow PtO + H^+ + e^- \qquad E = 0.8\, V\, RHE \qquad (5\text{-}5)$$

Finally, we consider the interface between the Pt NPs and carbon. Here C-OH, which is the unstable surface oxide of carbon, reacts with $Pt(OH)_{ads}$ to form carbon dioxide. As a result, a carbon vacancy (V_C) is created due to the following reaction [104]:

$$C - OH + Pt(OH)_{ads} \leftrightarrow V_C + CO_2Pt + 2H^+ + 2e^- \qquad E = 0.65\, RHE \qquad (5\text{-}6)$$

In order to understand a possible correlation between carbon degradation and NPs motion, we irradiated the CNTs with 200 keV electrons at a dose rate in the order of 10^3 e/Å^{2}sec to knock-out carbon atoms, while the NPs were observed. This situation is similar to the effect of carbon corrosion, where carbon vacancies are formed, according to equation

(5-6). As shown in Figure 5-4, as carbon atoms were removed from the carbon/particle interface (shown by yellow arrows) during irradiation, particle 1 started to move toward the larger particle. This particle keeps moving on the surface of the CNT as more carbon atoms are knocked-out at the carbon/particle interface by the electron beam. In particular, note the absence of carbon on the left side of particle 1. As a result, the distance between particles 1 and 3 decreased from 3 nm (at minute 12) to 1.8 nm (at minute 42). Particle 2 also moved and rotated towards the larger particle. In fact, a comparison between the FFTs of particle 2 in Figure 5-4b and c confirms the rotation of the particle, as the zone axis changed from [110] to [001].

This set of experiments seem to indicate that when carbon atoms are removed from the CNT at the carbon/particle interface, leaving carbon vacancies, the particle tends to make new bonds with the nearest carbon atoms to decrease its free surface energy, thus leading to particle motion. Similarly to electron beam irradiation, voltage cycling results in the formation of carbon vacancies at the carbon/particle interface due to the production of carbon dioxide, which consequently cause particle migration (Figure 5-5).

Upon particle migration, the NPs are likely to contact each other and subsequently coalesce into a single particle, driven by a reduction in surface energy. Figure 5-6 shows phase contrast TEM images of two adjacent particles in real time, going through the process of coalescence. First, atoms move towards the neck between the two adjacent particles through surface diffusion. In particular, the atoms on the {100} surface atomic layer (red arrow 1 in Figure 5-5a) diffuse to the top of the neck between the two particles, adding a

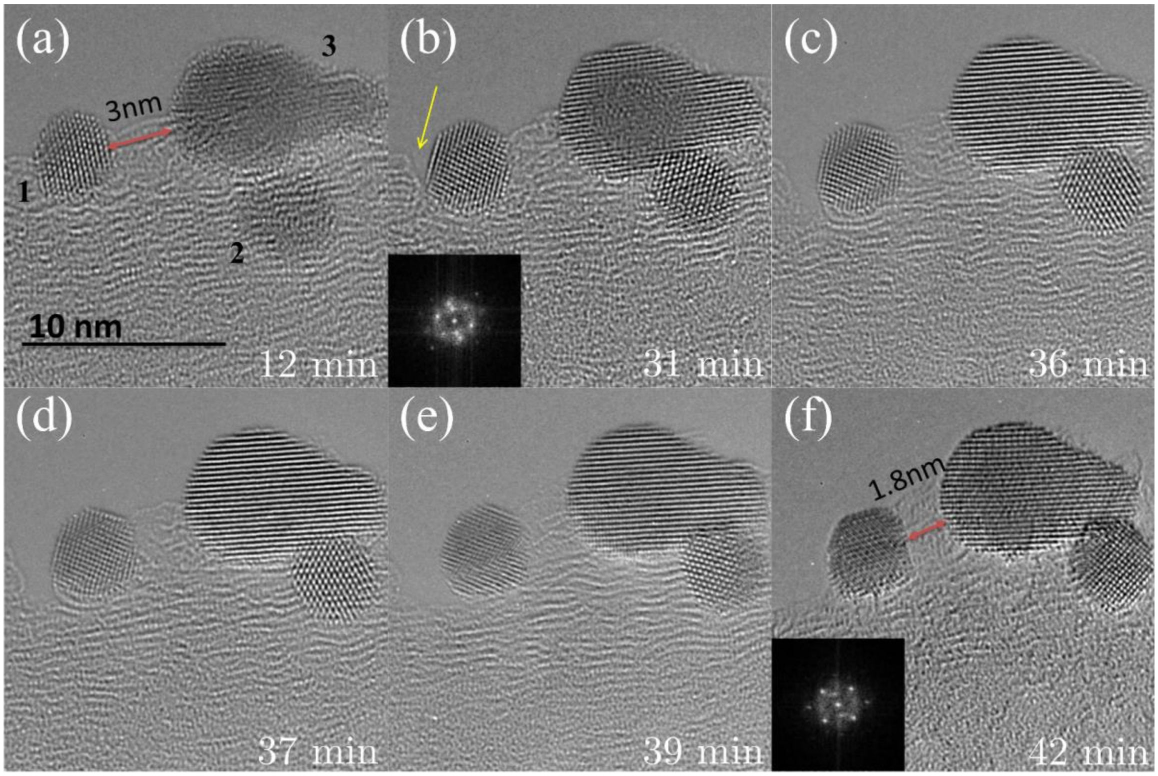

Figure 5-4 Aberration-corrected TEM images of the Pt nanoparticles movement on the carbon nanotube under the effect of electron beam

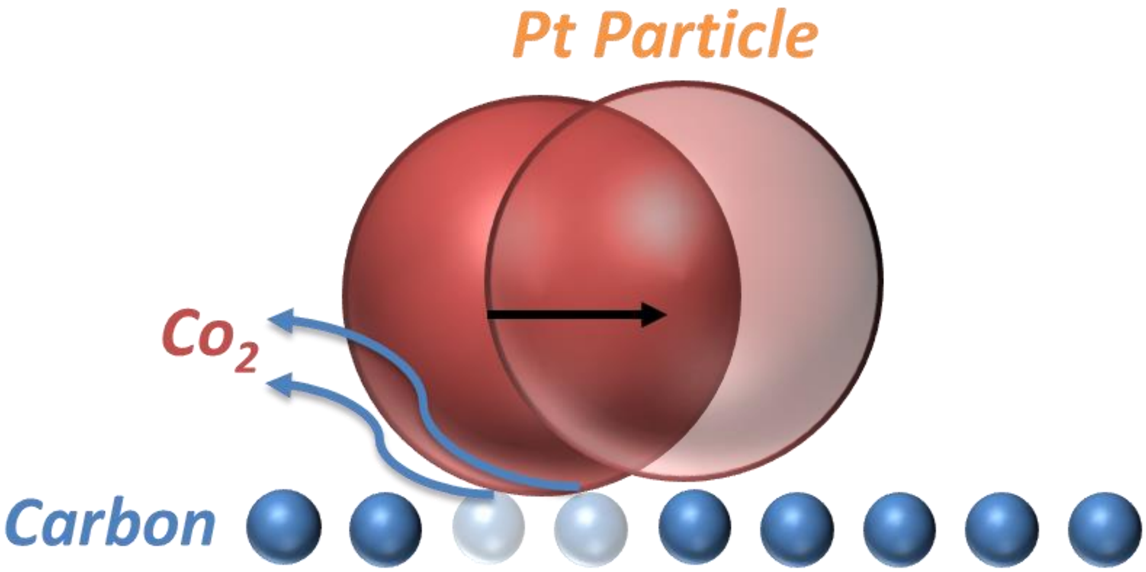

Figure 5-5 . Schematic of the proposed particle movement mechanism on the surface of carbon new {111} plane (red arrow 2 in Figure 5-6b) in the neck region. Thereafter, coalescence continues through surface or lattice diffusion. The three dash red lines in Figure 5-6c shows the disappearance of {111} planes on the right side of the image, as atoms on these planes move to form another set of {111} planes (the direction of diffusion is shown by the red arrow in Figure 5-6c) toward the neck area (compare the red ovals in Figure 5-6b and c). As diffusion towards the neck continues, the dihedral angle is reduced. However, in the current experiment, rotation of the NPs also occurs, which helps reducing the dihedral angle from 24° to 13° (Figure 5-6b and c) leaving a dislocation at the grain boundary. This is confirmed by the inverse filtered FFT of the neck area (inset of Figure 5-6c), where an extra half {111} plane is visible. Finally, the dislocation is eliminated during the late stages of coalescence leading to a defect-free single particle.

After the initial 1000 cycles, our identical-location experiments indicate a change in mechanism for the loss of electrochemical active surface area. In particular, due to the dissolution of Pt, which becomes significant, single atoms and atomic clusters appear on the ionomer phase at the surface of the CNT. Subsequently, these atoms move toward larger particles and deposit on their surfaces (Figure 5-7 and Figure 5-8). For example, cluster 1 in Figure 5-7c is first dissolved. These Pt atoms move toward the larger particle, where they re-deposit (arrows 1 in Figure 5-7c and d). Moreover, atomic clusters can deposit preferentially at the gap between two or more particles and consequently from a bridge, as it is shown within the red squares of Figure 5-8a and b.

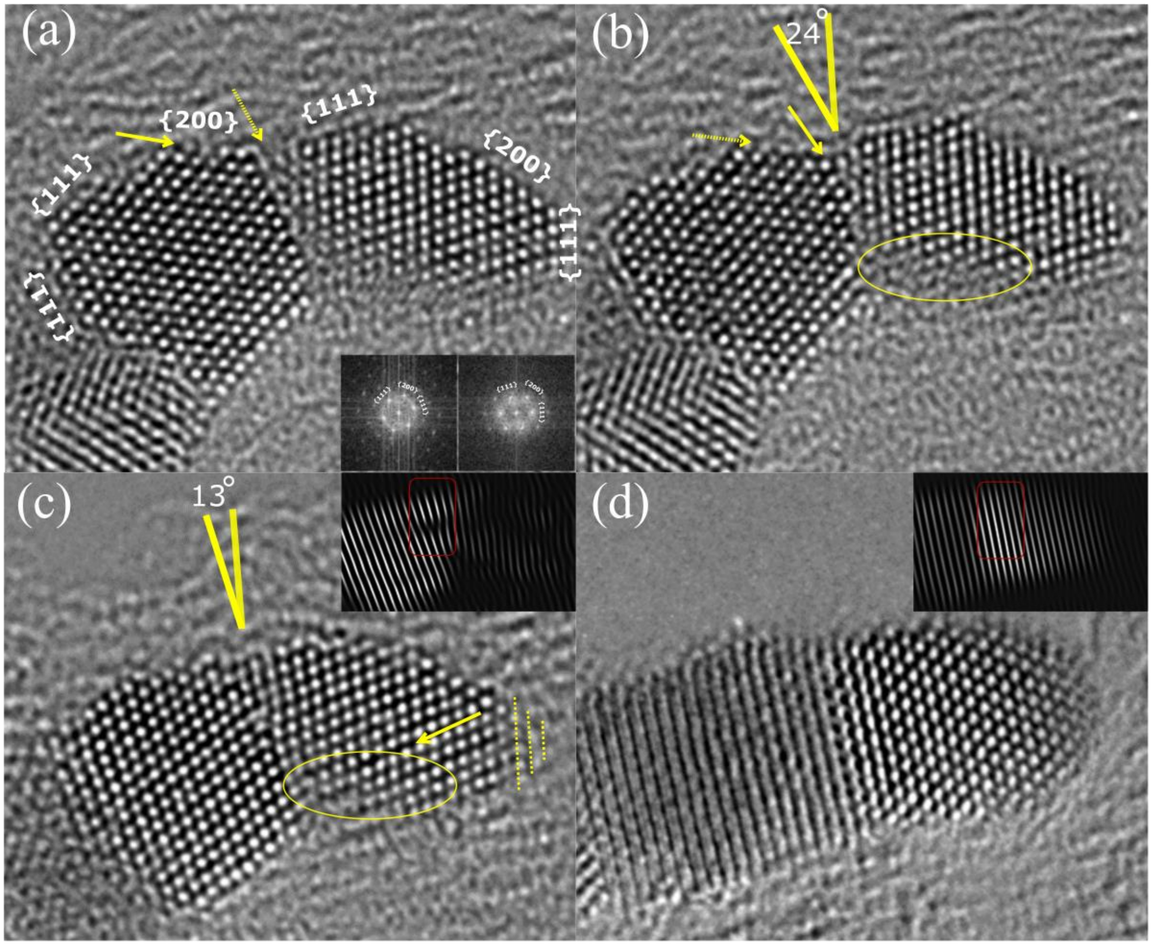

Figure 5-6 Real-time aberration corrected TEM images of the Pt nanoparticle coalescence under the effect of electro n beam at room temperature

In our previous work [REF], we proposed cluster bridging as a new mechanism for surface area loss of particles during voltage cycling based on a post-mortem TEM study of MEAs. In the current paper, we are thus able to confirm this mechanism through direct observation. As HAADF STEM imaging provides mass/thickness contrast, and no diffraction contrast, the clusters and single atoms on the surface of the CNT become very apparent. Figure 5-8d shows that many single atoms and clusters appear on the surface of the CNT after 2000 cycles, which plays an important role in the surface area loss of the nanoparticles through re-deposition of single atoms and/or cluster bridging.

In order to determine the effect of electron beam on the surface area loss mechanisms of NPs, and investigate if the observed mechanism is purely due to voltage cycling, the accelerating voltage and the electron dose rate were reduced to the range under which the CNTs are stable. For this purpose, an aberration corrected FEI Titan was operated at 80 kV using a dose rate of less than 100 e/Å^{2}sec, for TEM observations before and after 2000 and 5000 potential cycles. Under these conditions (Figure 5-9), the particles continue to be mobile on the CNT which lead to coalescence during potential cycling (red ovals 1-4 show examples of particle movement and coalescence). As before, the appearance of atomic clusters on the surface of the CNTs is also observed as a result of particle dissolution. For example NPs within the blue square 5 seem to be dissolving as they reduce their size after 2000 cycles, while atomic clusters appear on the CNT (blue arrows in Figure 5-9b and c). Even particles that exhibit an increase in size by the deposition of single atoms or atomic clusters may be subjected to dissolution. This is shown within the blue square labeled 6, where NPs increase their size after 2000 potential cycles,

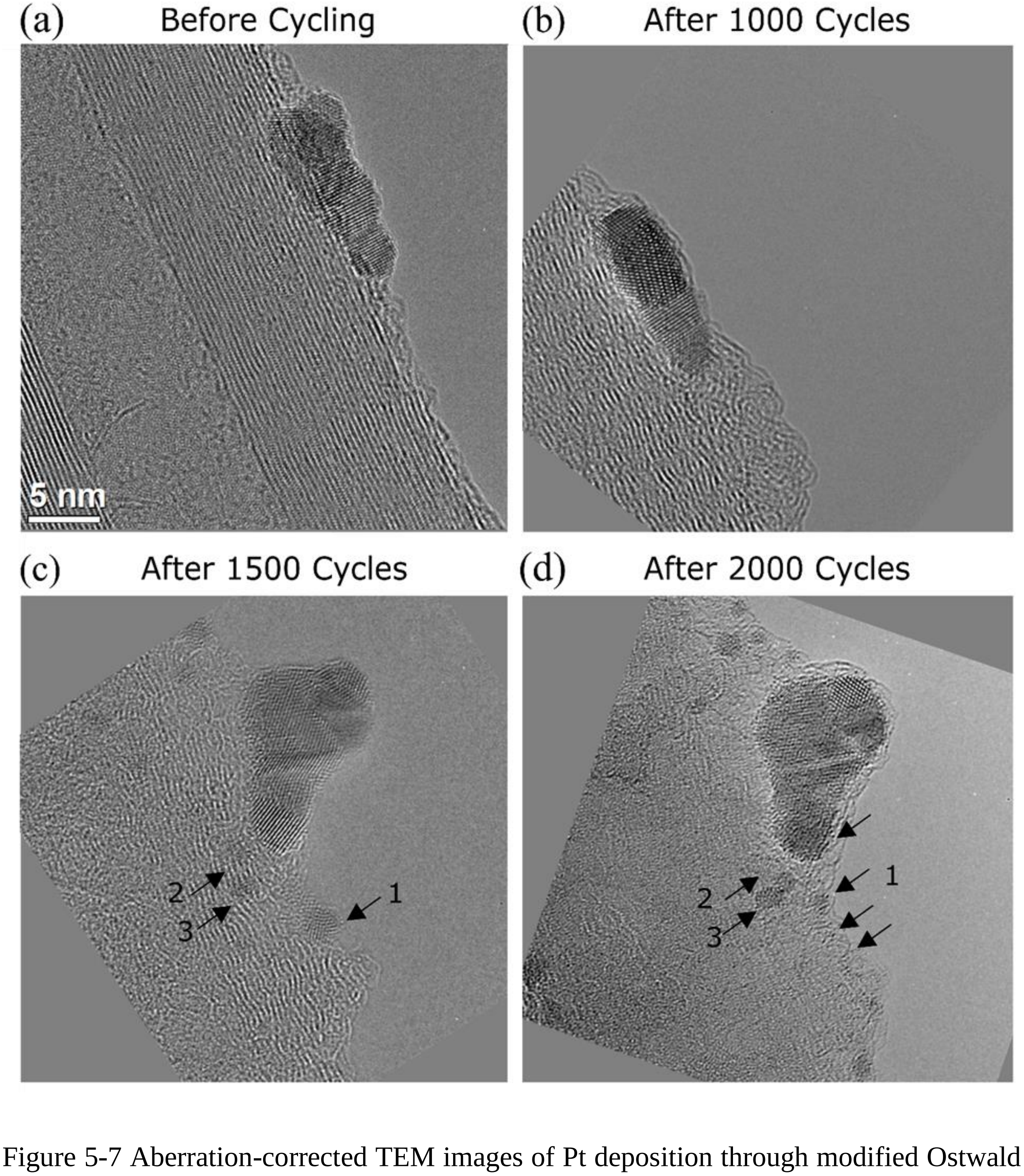

Figure 5-7 Aberration-corrected TEM images of Pt deposition through modified Ostwald ripening at different stages of voltage cycling.

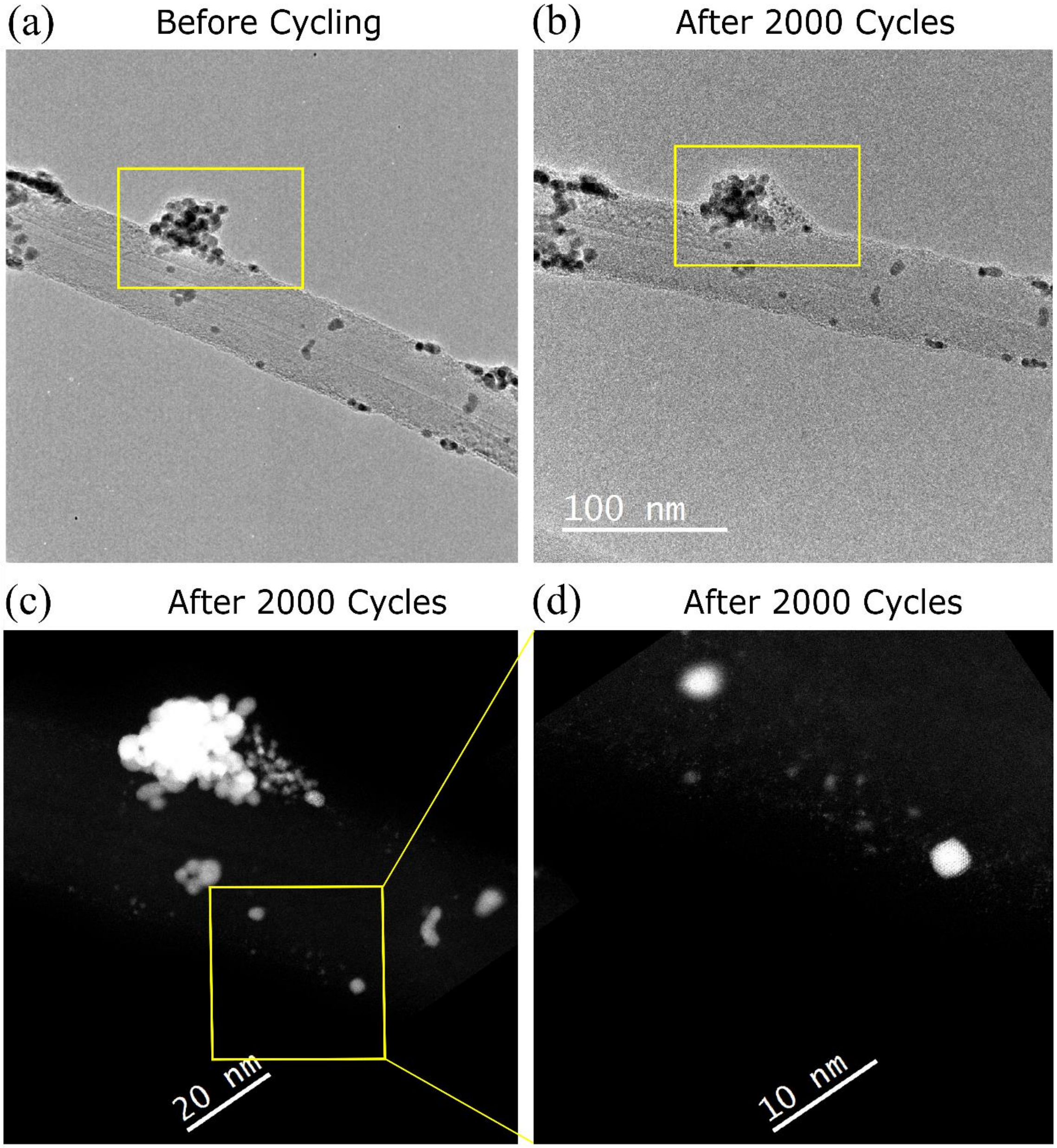

Figure 5-8 Aberration-corrected TEM images of Pt on carbon nanotubes a) before, and b) after 2000 voltage cycles, c) and d) Aberration-corrected STEM images of Pt on carbon nanotubes after 2000 voltage cycles.

due to the deposition of single atoms on their surfaces, while further cycling results in their shrinkage, most likely due to dissolution.

In general, it seems that the exposure to the electron beam during a short amount of time (exposure time of 1 sec) does not affect the surface area loss mechanisms, as both particle movement and coalescence, as well as particle dissolution and re-deposition were detected under low accelerating voltage and low electron dose. Another source of degradation, which is more obvious by increasing the potential cycling to 5000 cycles, is the appearance of a layer on the CNTs which covers the NPs. This layer, which might be either amorphous carbon or the PBI/PVPA ionomer phase, restricts the reactant gas to access the surface of the NPs and consequently results in the loss of electrochemically active surface area of the nanocatalysts. In order to investigate if this layer is caused by carbon contamination under the effect of the electron beam or caused by potential cycling, new areas on the TEM grid, which were not exposed to the electron beam before potential cycling were observed by TEM. The images of these areas (Figure 5-10) after 5000 potential cycles confirm that the appearance of this layer happens for all of the CNTs, independent of any exposure to the electron beam.

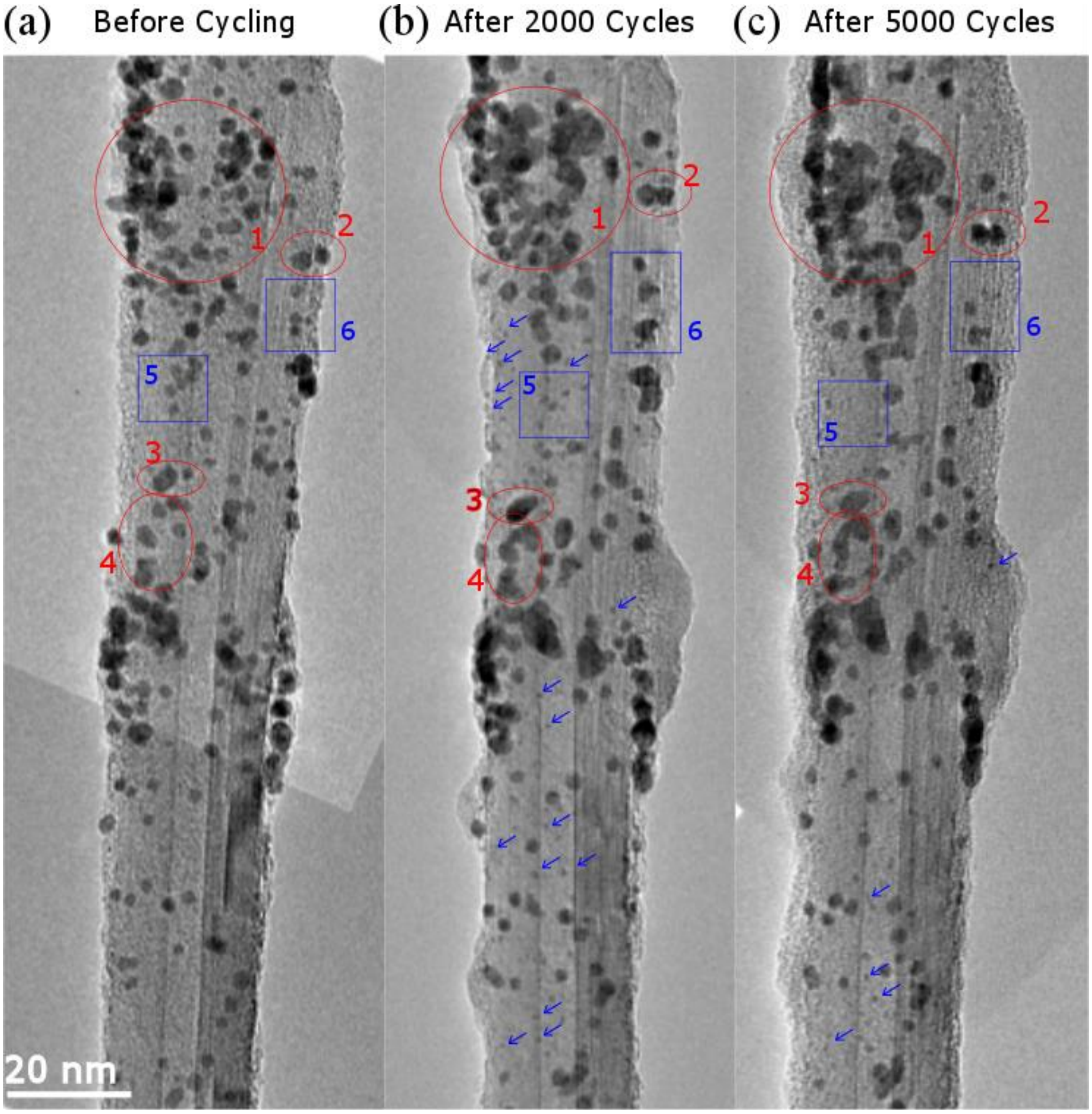

Figure 5-9 TEM images of Pt on carbon nanotubes a) before cycling, b) after 2000 potential cycles, c) after 5000 potential cycles using FEI Titan at 80 KV and the electron dose rate of < 100 e/A2sec.

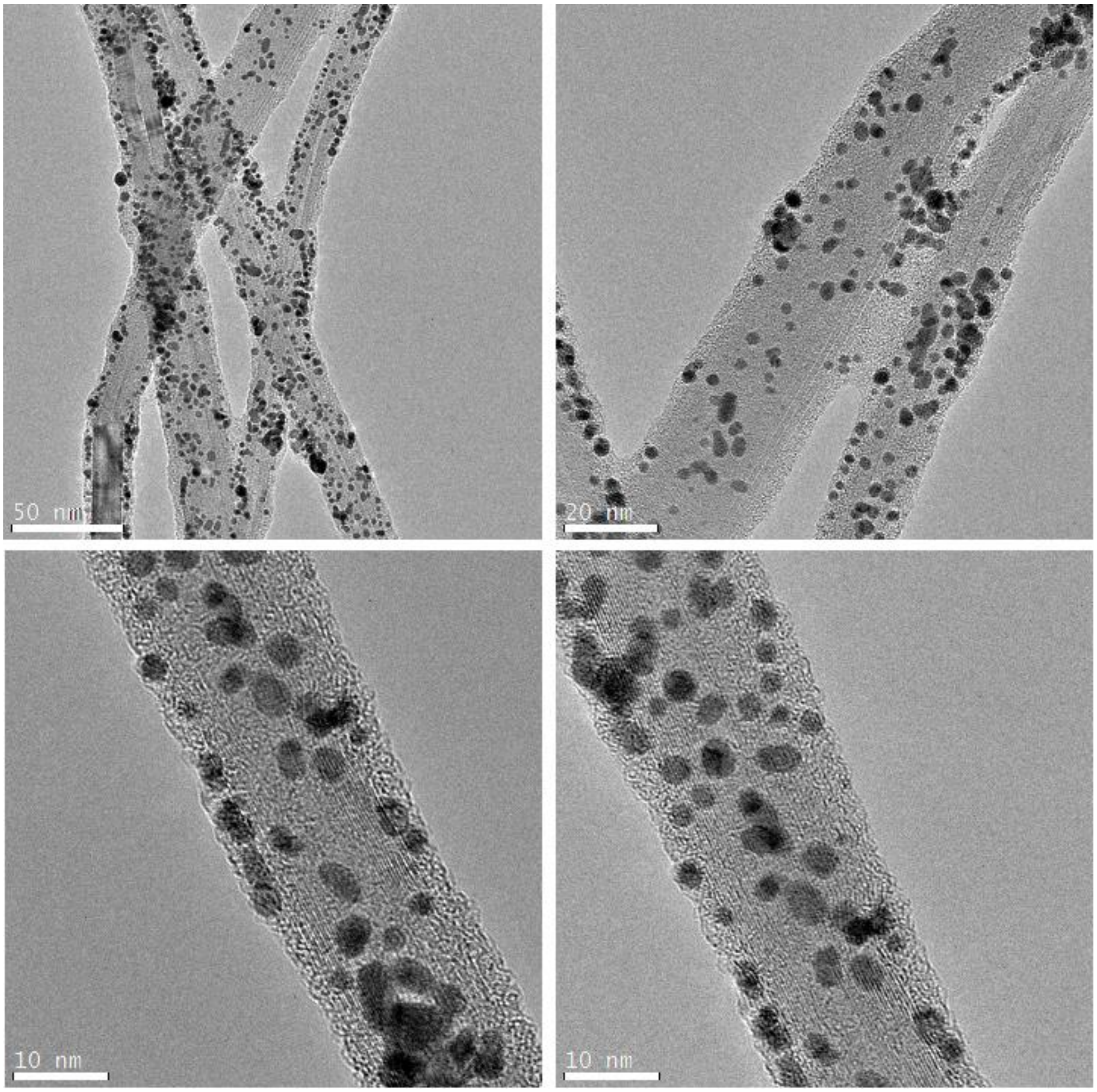

Figure 5-10 TEM images of the Pt on CNTs after 5000 potential cycles from areas which have not been exposed to the electron beam before cycling.

5.3.2 Pt NPs supported on Amorphous Carbon

In order to investigate the effect of potential cycling on Pt NPs supported on amorphous carbon, similar identical location experiments were performed on Akzo Nobel Ketjen EC300J carbon black (Pt/CB). As it is shown in the 3-D image of Pt/CB, reconstructed from a total of 60 TEM images over a tilt range of -60 to +60 degrees, with a 2° tilting (Figure 5-11), the carbon substrate is not flat and has a convoluted 3D structure. As the nanoparticles are actually within the 3-D carbon network, the movement of NPs in the direction perpendicular to the 2D images cannot be identified.

Figure 5-12 shows the TEM images of 3.2 nm Pt nanocatalysts supported on CB before and after 2000 and 5000 potential cycles. Similar to the NPs on carbon nanotubes, these particles are mobile on the surface of amorphous carbon. Almost all of the particles change their relative position after potential cycling. They either move toward or drift apart from each other. For example, particles 1 and 2 first move toward each other after 2000 cycles but then drift apart after 5000 cycles. In some cases, the particles move toward each other until they make contact and coalesce (boxes labeled 3 and 4). On the other hand, particles in box 5 seem to de-sinter after potential cycling. This type of behavior has been shown previously to occur in MgO particles [105]. However, we should point out that these nanoparticles are sitting on a carbon substrate that is not completely flat, as seen from the 3-D reconstructed image (Figure 5-11). Thus, it is possible that the nanoparticles that seem to de-sinter or move apart may actually not be in contact, but instead may be in different planes.

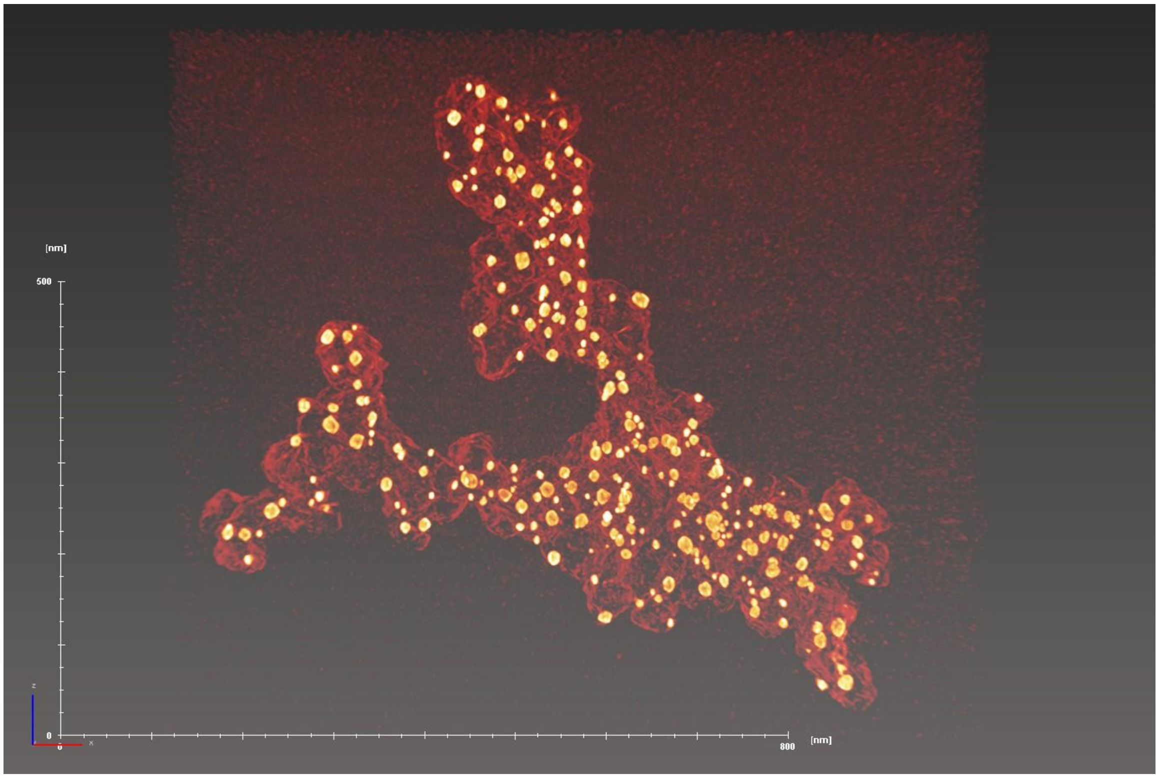

Figure 5-11 3D reconstructed image of Pt NPs supported on amorphous carbon

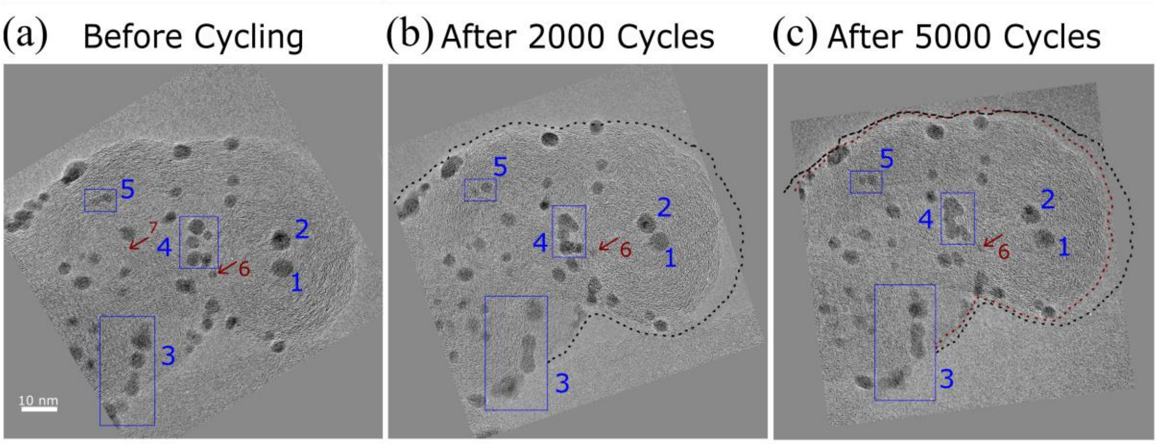

Figure 5-12 TEM images of Pt NPs supported on amorphous carbon a) before, b) after 2000, and c) after 5000 potential cycles.

In contrast to the NPs on carbon nanotubes, the appearance of atomic clusters are very difficult to observe on the surface of amorphous carbon. However, some particles (numbered 6 and 7 in Figure 5-12) disappear from the carbon support, most probably due to dissolution. The reason why no atomic clusters appear on the surface of amorphous carbon, in contrast to carbon nanotubes, can be due to the lack of ionomer phase on the surface of amorphous carbon. The CNTs in the previous experiment (Figure 5-9) were wrapped in ionomer during synthesis, while no ionomer was used in the synthesis of the Pt NPs on amorphous carbon. The ionomer phase serves as a medium for the atomic clusters to move on the surface of carbon. Thus, the lack of ionomer on amorphous carbon results in the release of Pt ions in the liquid electrolyte. This is likely why no atomic clusters can be observed on the surface of amorphous carbon, and no significant particle growth due to Ostwald ripening can be seen.

Another important observation is the change that occurs in the shape and structure of carbon. The shrinkage of carbon during potential cycling is also shown in Figure 5-12. For comparison, the outline of the carbon before cycling (Figure 5-12a) is indicated as a black dash line, overlapped on the image of carbon after 2000 cycles in Figure 5-12b. Similarly, the carbon after 5000 cycles is overlaid by both outlines from the images before cycling (black dash line) and after 2000 cycles (red dash line). Similar to the case of carbon nanotubes, the structure of carbon black changes after potential cycling. The comparison between the structure of carbon in Figure 5-12 a, b, and c illustrate the lower graphitic nature after 2000 and 5000 potential cycles as the curved graphene layers are less pronounced in Figure 5-12c than b and a.

Both the change in the size and structure of carbon can be responsible for particle movement through the mechanism explained in section 5-3-1 (Figure 5-5). Comparing Figure 5-12 and Figure 5-9, the particles seem to be more mobile on the surface of CNTs than amorphous carbon. As shown in the tomographic image of carbon black, amorphous carbon exhibits a convoluted 3D structure, in contrast to carbon nanotubes with a flat surface. As a result, the particles on the surface of carbon black are likely to have larger fraction of surface area in contact with carbon than particles supported on CNTs (Figure 5-13). Thus, more vacancies are needed at the carbon/particle interface for particles to start their motion, according to the proposed mechanism of particle movement (Figure 5-5).

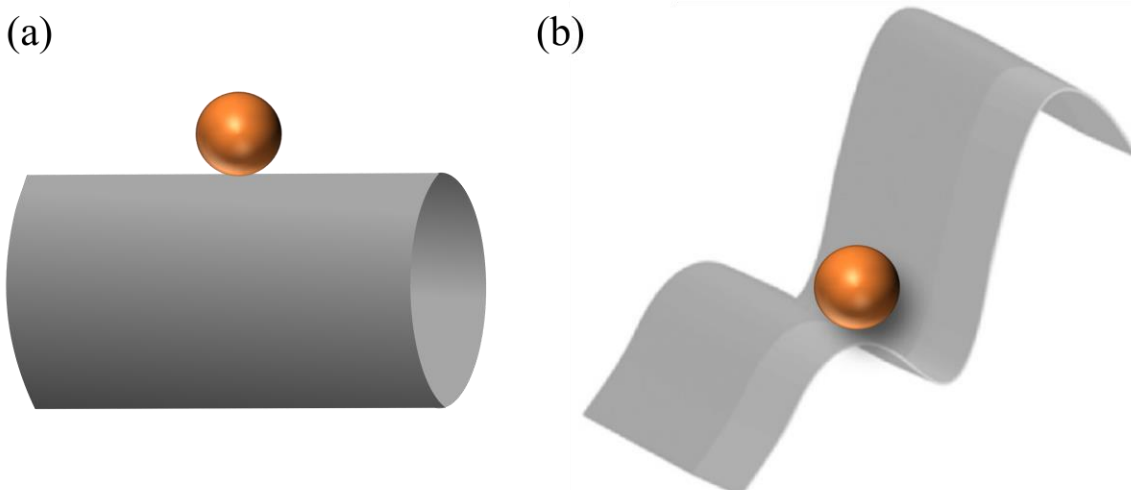

Figure 5-13 Schematic of a particle in contact with a) carbon nanotube, and b) amorphous carbon.

Chapter 6: Identical location STEM on Pt alloy Nanopcatalysts

6.1 Introduction

In the previous chapter, the behavior of Pt NPs supported on carbon nanotubes and amorphous carbon was investigated. In the case of Pt-alloy NPs, we expect that new factors, such as heterogeneous dissolution of Pt, the presence of alloying elements during voltage cycling and enthalpy of mixing of the elements, might affect the mechanisms of loss of specific activity and the active surface area of the NPs during fuel cell operation. Thus, it is not yet clear what parameters control the degradation in alloy nanocatalysts and whether the classical surface area loss mechanisms can fully explain the growth of alloy NPs. Many studies, including post-mortem transmission electron microscopy (TEM) studies have been performed to address the mechanisms of catalyst degradation [8]–[11], [13], [14], [83]. However, a fundamental understanding of particle behavior in real time, during the various stages of fuel cell cycling, needs further investigation. In this context, the focus of this work is to analyze the behavior of PtNi and Pt_3Co NPs, at different stages of fuel cell cycling, using identical location scanning transmission electron microscopy (STEM). Using aberration corrected stem has a lot of advantages to study the alloy NPs. As the STEM high angle annular dark field (HAADF) detector captures electrons that are inelastic scattered to higher angles, the intensity in the HAADF images is proportional to the product of the square of average atomic number and thickness of sample. Thus the

STEM images are mass thickness contrast with no diffraction contrast, which can reveal information on the variations in the chemical composition within a NP. In addition, carbon support particles exhibit very weak intensities in dark-field mode, to a point where single atoms and atomic clusters can be detected.

6.2 Experimental Procedure

The alloy nanocatalyst is de-alloyed PtNi supported on Akzo Nobel Ketjen EC300J (KB) (d-PtNi/KB) provided by Johnson Matthey Fuel Cells Ltd (JM, UK) with a Pt loading of 28.5 wt% and a Ni loading of 6.68 wt% as determined via inductively-coupled plasma atomic emission spectroscopy. The catalyst particles, deposited via a proprietary procedure, had an as-deposited Pt to Ni atomic ratio of 1:3. Following deposition and a proprietary heat treatment procedure to promote alloy formation, the catalyst was subjected to a proprietary acid treatment procedure to leach Ni from the catalyst particles resulting in a final Pt to Ni atomic ratio of 1:0.78.

For Pt_3Co nanocatalysts, the NPs were prepared by deposition of 40 wt % Pt and Co (3:1 atomic ratio) onto Akzo Nobel Ketjen EC300J via proprietary methods, then annealed to achieve alloying and produce Pt_3Co catalysts of 4.9 nm mean equivalent particle size.

The initial PtNi NPs were characterized by high angle annular dark field (HAADF) aberration-corrected STEM using a JEOL JEM ARM 200F at 200 kV. Energy dispersive X-ray spectroscopy (EDS) coupled to the JEOL microscope was used to analyze the Pt/Ni composition distribution of the NPs.

In order to assess the degradation of Pt alloy catalyst NPs, Identical location STEM technique was used. The detail of the procedure was explained in chapter 3.The electrocataslysts were cycled between 0.6 and 1.1 V vs. RHE in N_2-saturated 0.1M $HClO_4$ liquid electrolyte with the sweep rate of 0.2 V/sec. After voltage cycling, the TEM grid was rinsed and dried, and then transferred to the microscope.

6.3 Results and Discussions

6.3.1 Pt-Ni Nanocatalysts

6.3.1.1 Characterization of the Initial Powder

In order to analyze the effect of potential cycling on PtNi NPs, a complete characterization of the initial powder is required. The PtNi powder used for this study has an average equivalent particle diameter of 5.8 nm with a distribution of particles ranging from 3 to 12 nm with the majority of the particles lying between 5 to 7 nm (Figure 6-1).

The majority of NPs exhibit a solid solution of Pt and Ni, as shown by the aberration-corrected HAADF STEM image taken with the beam direction, B=[110] (Figure 6-2a). The lack of super-lattice reflections (see Fast Fourier Transform (FFT) in the inset of Figure 6-2a) shows that the NP has a disordered structure, where Pt and Ni are randomly distributed in a FCC crystal structure. However, as noted in Figure 6-2a, pockets of bright and dark contrast are evident throughout the NP, which is likely due to the heterogeneous distribution of elements. Yet, as the HAADF STEM image contrast is dependent on both thickness and mass, it is important to separate both effects. In this

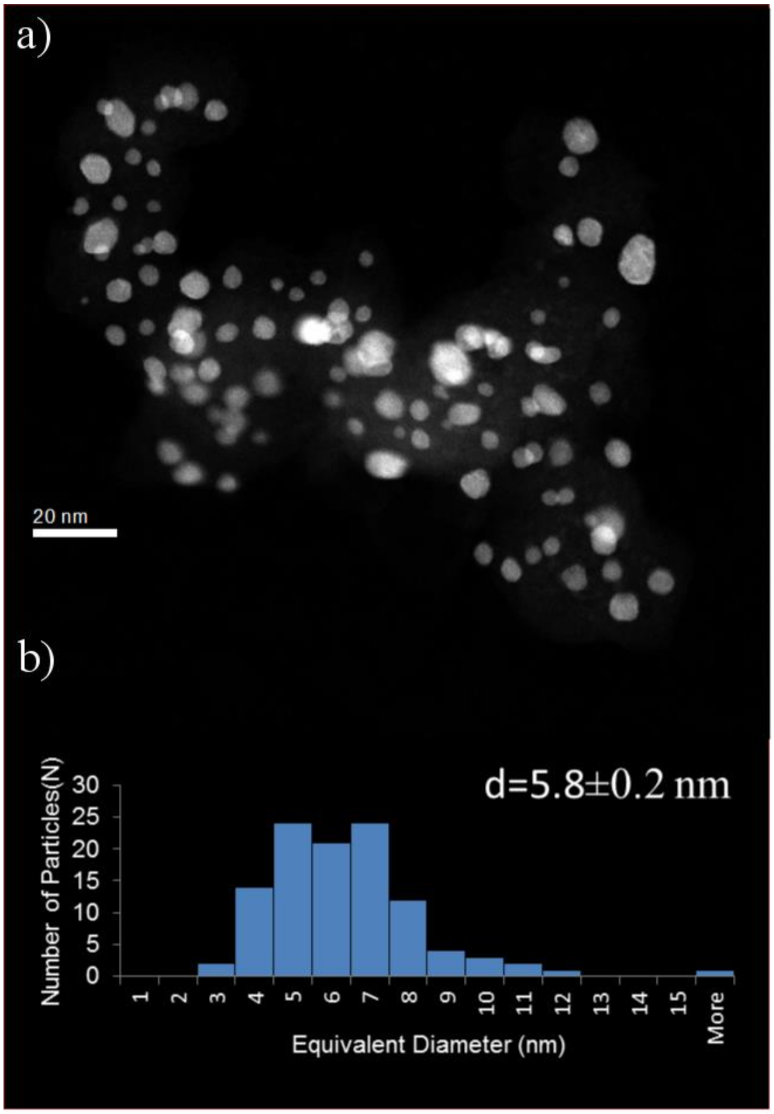

Figure 6-1 a) HAADF STEM image of the Pt-Ni NPs, and b) Particle size distribution of the Pt-Ni NPs.

context, the column-by-column normalized HAADF intensity variation across the NP (orange line in Figure 6-2a) is compared with the normalized thickness variation of a truncated octahedron projected along the same orange line (Figure 6-2b). Since the intensity of the HAADF image is approximately proportional to the square of the atomic number (Z^2) and linearly proportional to thickness (t), we can determine the normalized atomic number of each atomic column along the orange line. This is shown in Figure 6-2c, shows that there are Pt-rich regions (brighter) with higher atomic number, and other regions (darker) with lower atomic numbers.

Although most of the NPs exhibit a solid solution structure, there are NPs which show partially ordered structures, as shown in Figure 6-4 In this image, the super-lattice reflections present in the FTT of the blue square 1 verifies the ordered structure of this region, while the lack of super-lattice reflection in the FFT of square 2 shows a disordered structure. In fact, the atomic structure of the ordered region matches well the HAADF STEM computer simulation of the L_{10} structure viewed along the 111 zone axis (Figure 6-4b) which is the stable structure for 50% Pt-50% Ni according to the Pt-Ni phase diagram [106].

The EDS mapping of the NPs confirms a Pt rich layer on their surface, as well as small Pt rich and Ni rich regions inside the particles **(**Figure 6-3**)**. This is consistent with the intensity variations in the HAADF image shown in Figure 6-2. An important observation from the composition distribution of the NPs is that smaller particles have a considerably higher amount of Pt and a thicker Pt-rich shell (compare particle 1 and 2 in Figure 6-3d). The reason for this behavior starts with the leaching process of Ni, the less

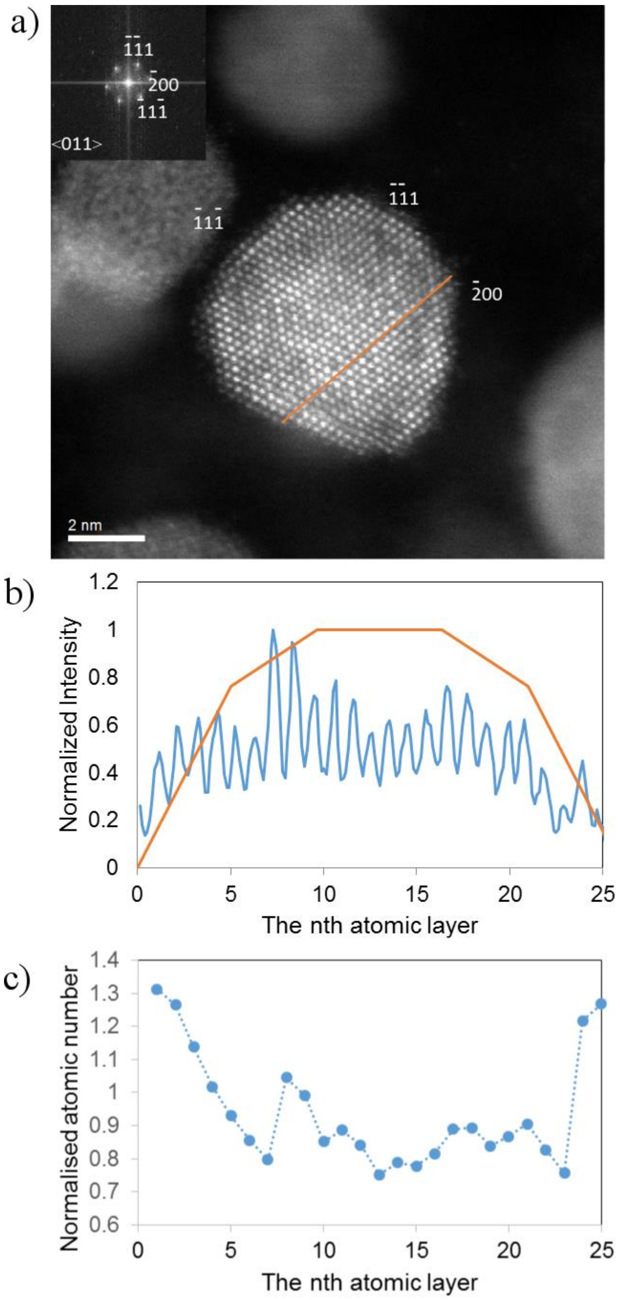

Figure 6-2 a) Aberration-corrected HAADF image of a Pt-Ni NP and corresponding FFT (inset). b) Normalized intensity across the NP and c) Normalized atomic number for each atomic column across the NP (along the orange line).

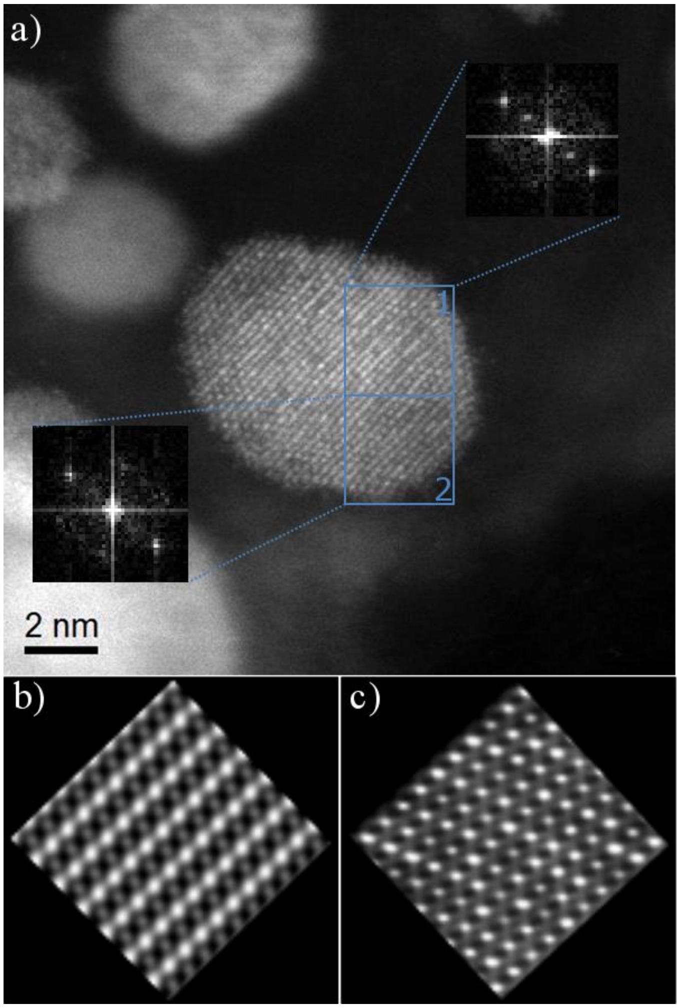

Figure 6-3 a) Aberration-corrected HAADF STEM image of a Pt-Ni NP. The insets show the FFTs of regions 1 and 2 within the NP, b) STEM HAADF computer simulation of the L10 structure (space group P4/mmm) along the <111> zone axis corresponding to region 1, and c) STEM HAADF computer simulation of a random solid solution (space group Fm$\overline{3}$m), corresponding to region 2.

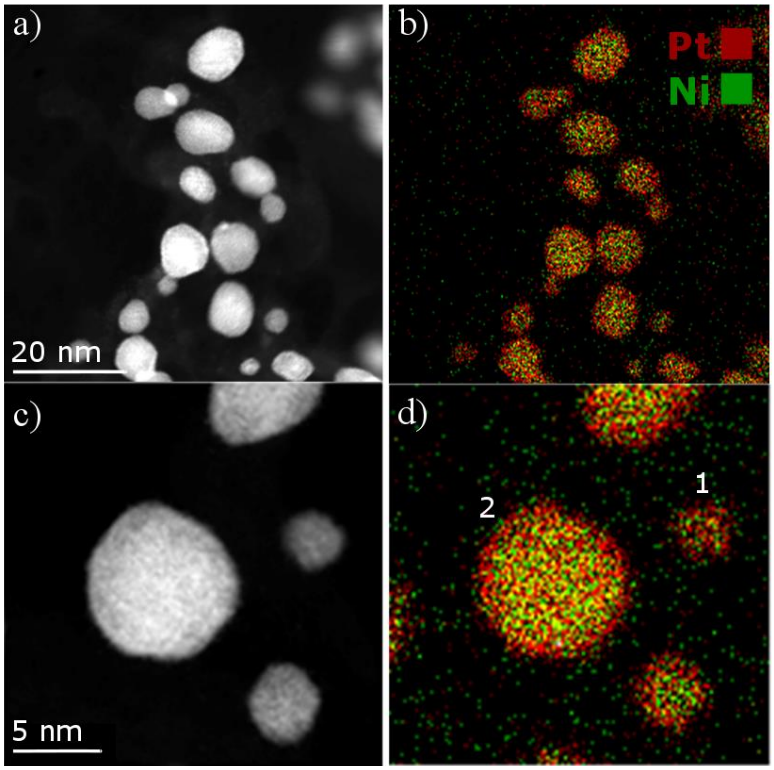

Figure 6-4 HAADF STEM of Pt-Ni NPs, b) EDS mapping of the NPs in a), c) higher magnification HAADF STEM image of the Pt-Ni NPs, and d) EDS mapping of the NPs in c) showing a Pt-rich surface layer on the NPs.

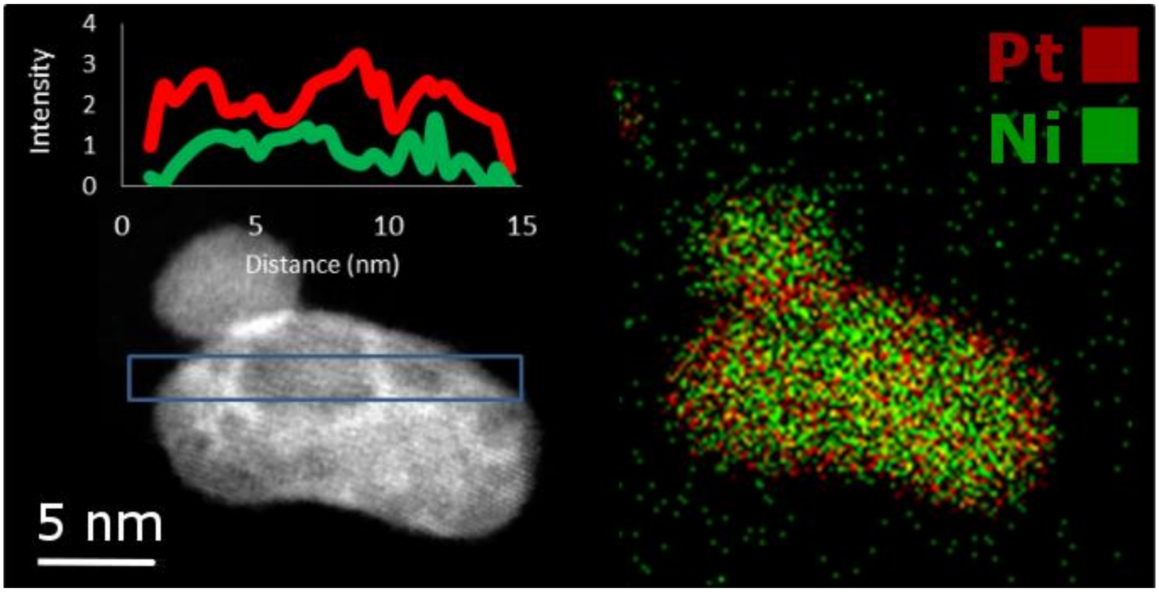

Figure 6-5 HAADF STEM image and EDS mapping of large Pt-Ni NPs (>10 nm). The inset shows the intensity profile of Pt and Ni along the blue rectangle.

noble element, which occurs preferentially at the outermost layers of the NP, leading to the formation of a Pt-rich surface. In smaller NPs, the fraction of surface atoms with respect to bulk atoms increases, and thus smaller NPs are more prone to Ni leaching due to the higher density of low coordination surface sites, such as steps and kinks. This results in the formation of a thicker Pt-rich layer and higher Pt/Ni ratio in these particles [11], [75], [83], [107].

There are other particles, mostly larger than 10 nm, showing high variations in contrast **(**Figure 6-5**)**. EDS mapping and the corresponding average intensity of the Pt and Ni signal along the blue rectangle in the HAADF image confirms the formation of nano-sized pores, as well as large Pt-rich and Ni-rich regions within the NPs. The presence of nano-pores is only seen in the larger NPs. This is confirmed by kinetic Monte Carlo simulations, which show that the amount of porosity is proportional to 1/r [108]. In other words, the formation of pores is initiated faster in larger particles, rather than smaller ones, due to the fact that the higher dissolution rate in smaller particles results in the formation of a passivated Pt-rich layer, protecting Ni from below the surface to dissolve [108]–[113]. As shown by EDS mapping, the Pt-rich layer also exists on the surface of larger particles, but it is thinner than that of smaller particles.

6.3.1.2 Effect of Voltage cycling

Figure 6-6 shows changes in carbon support during the different stages of voltage cycling. These changes are due to carbon corrosion, as a result of series of reactions occurring on the surface of carbon, which produce carbon dioxide and carbon vacancies.

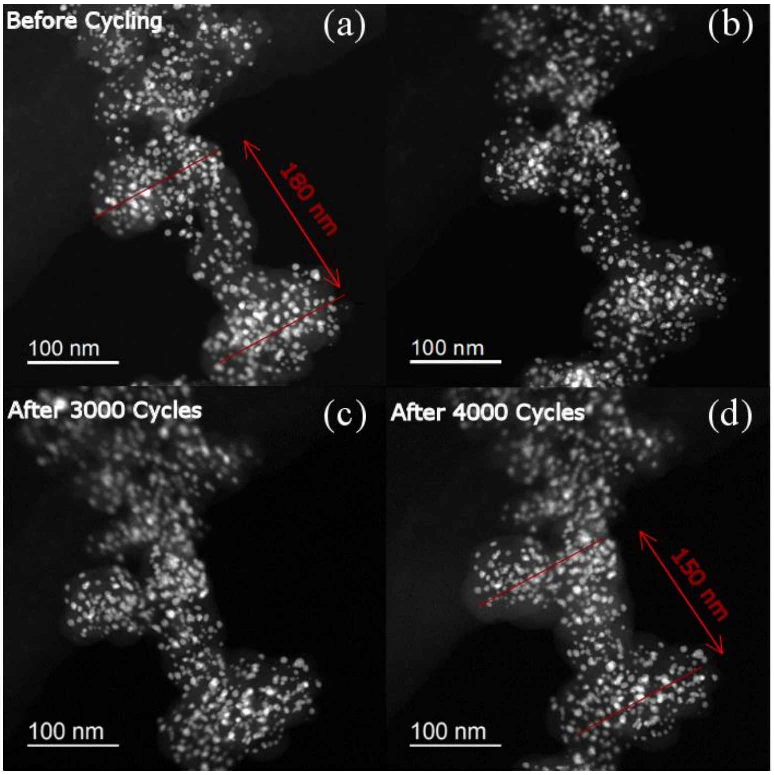

Figure 6-6 HAADF STEM images of Pt-Ni NPs on the carbon support before and after potential cycling.

One of the apparent modifications is the shrinkage of the carbon support. As shown in Figure 6-6, a projected region of the carbon support shrank in length from 180 nm to 150 nm after 7000 cycles. This led to changes in the location of the NPs, although no particle coalescence could be observed. One should consider that STEM images are 2D projected images, and thus the 3D inter-particle distance is not known. Yet, the typical 3D convoluted morphology of the carbon support prevents the particles from making contact and consequently coalescing.

Figure 6-7 shows another phenomenon which occurs during potential cycling. In this case, single atoms and atomic clusters appear on the surface of the carbon support after potential cycling, as a result of dissolution. In fact, the dissolution of single atoms has further consequences, as they move on the surface of the carbon support and re-deposit on larger particles through modified Ostwald ripening. Figure 6-8 shows the re-deposition of single atoms on a {111} type plane of a NP after 2000 cycles. In some cases, the dissolution and re-deposition may happen simultaneously in the same particle. This can be observed in Figure 6-9, where HAADF-STEM images of a particle before and after potential cycling show atoms on surface steps that were dissolved during voltage cycling and new {111} facets formed on the surface of the NP. Steps and kinks are high energy sites due to their lower coordination number, and thus are more prone to dissolution, in contrast to {111} type surfaces which exhibit a lower surface energy [114].

These experiments also show, for the first time, direct evidence of heterogeneous re-deposition of Pt, as shown in Figure 6-10a and b (red squares 1 and 2). Initially, as there

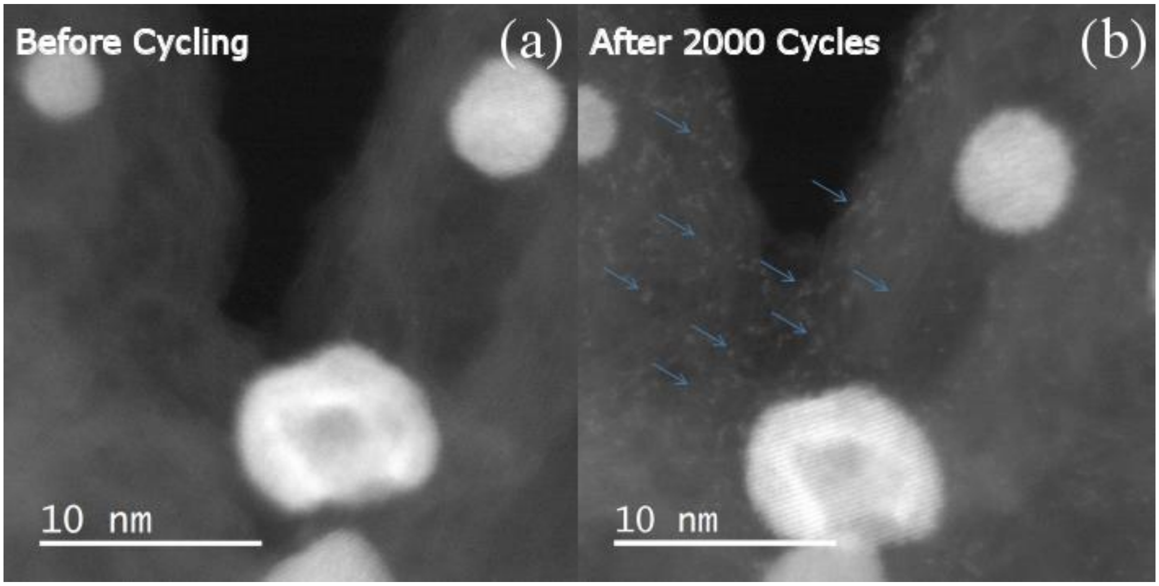

Figure 6-7 Appearance of single atoms and atomic clusters on the carbon support after voltage cycling.

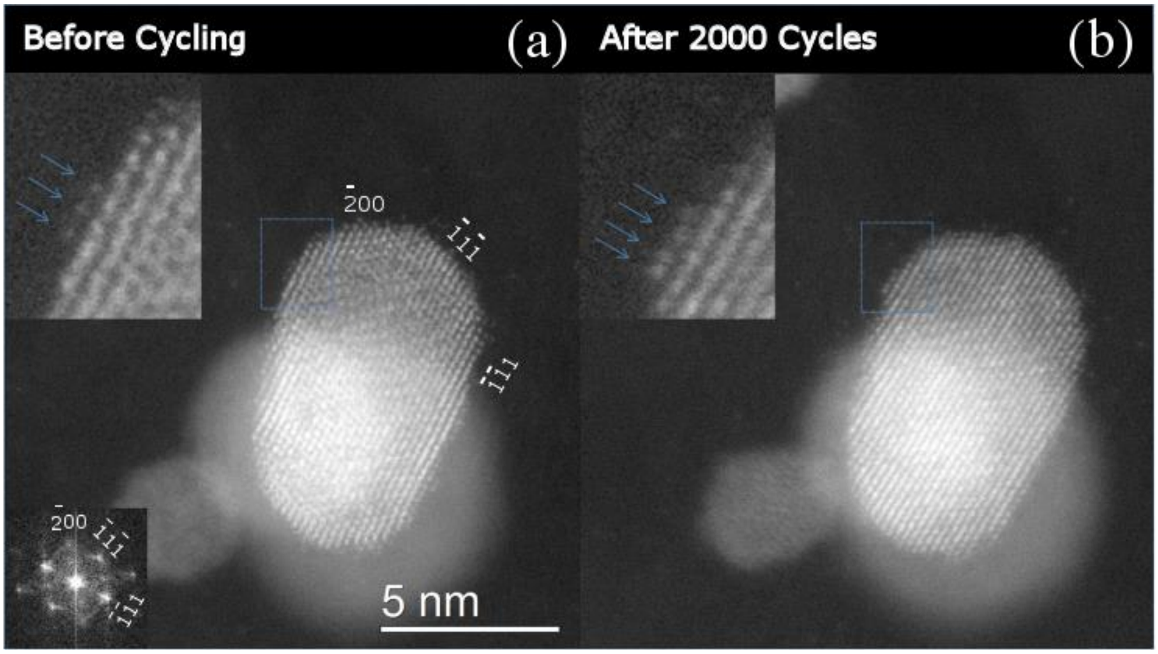

Figure 6-8 Deposition of single atoms on the (1) surface plane of a Pt-Ni NP. The insets on the top left corners are high magnification images of the regions within the blue boxes. The inset in the bottom left corner shows the FFT of the NP.

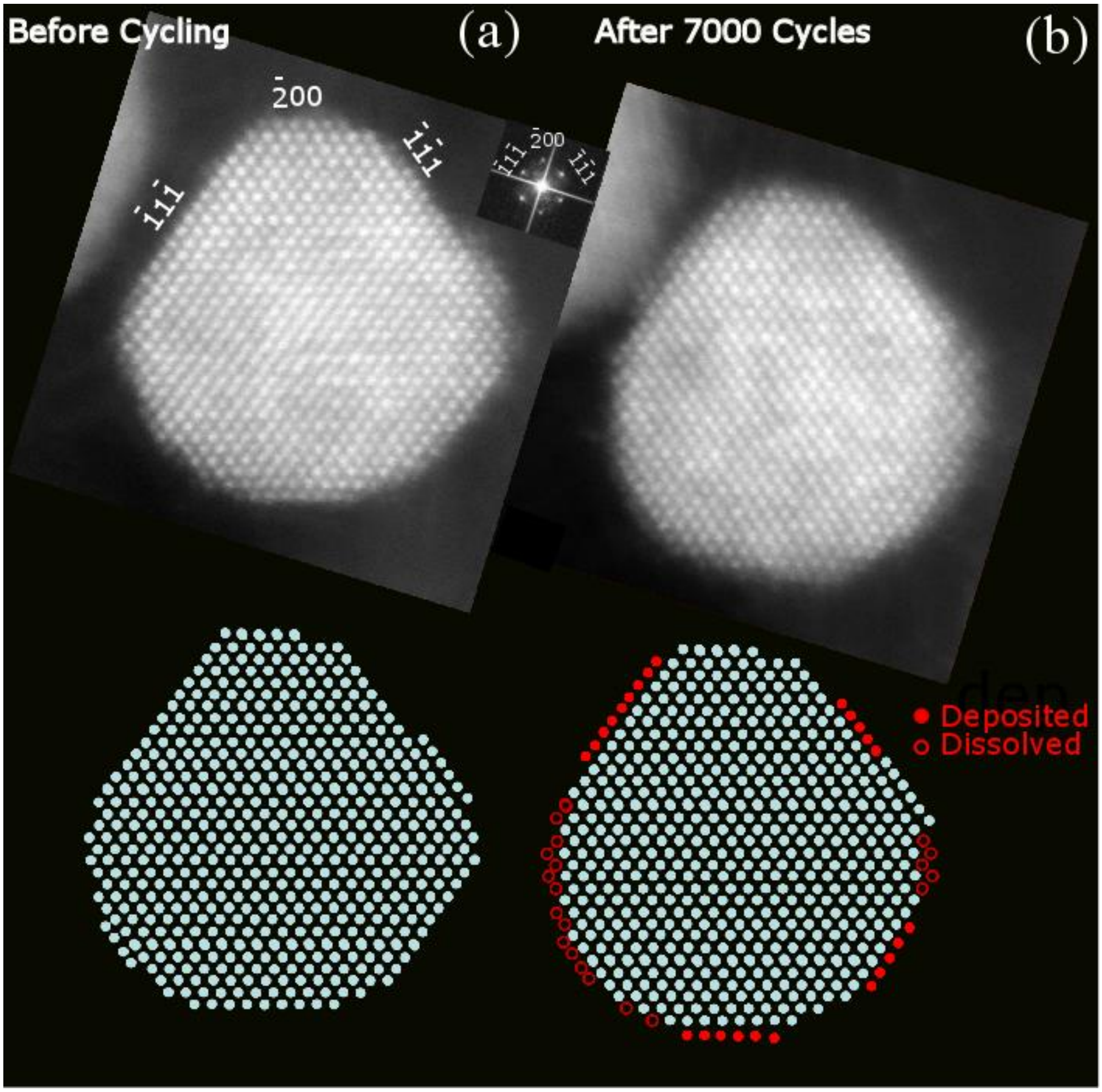

Figure 6-9 Dissolution and re-deposition of surface atomic layers before and after cycling (inset shows the FFT of the NP).

are no other particles nearby the ones shown in the red squares labeled 1 and 2 (see the low magnification image in the inset of Figure 6-10a), the re-deposition of single atoms must have occurred, instead of coalescence, to explain the change in size. However, it is generally accepted that particle dissolution and re-deposition (Ostwald ripening) is an isotropic process, i.e. larger particles grow at the expense of smaller ones but their morphology should not change. Yet, Figure 6-10 shows anisotropic growth of smaller particles (red squares 1 and 2), rather than larger ones, during voltage cycling. Figure 10c, which shows a higher magnification HAADF STEM image of the particle in the red square labeled 2 of Figure 6-10b confirms the extension of the lattice in the newly deposited material. Furthermore, a comparison between the EDS mapping of the particles before and after voltage cycling (red squares 1 and 2 in Figure 6-11a and b) shows that the atomic re-deposition consists of Pt and not Ni. Due to the low Ni/Ni^{2+} redox potential, the re-deposition of Ni on particles is not thermodynamically favorable [90]. As discussed before, smaller particles have lower amounts of Ni and thicker Pt-rich surface layers. This is evident in particles 1 and 2 in Figure 6-11a, where particle 1 has a higher fraction of Pt than the other particles and particle 2 has a thicker Pt-rich shell. This Pt-rich shell can act as a heterogeneous nucleation site for the re-deposition of Pt. In fact, it has been shown in the literature that the presence of a Pt-rich shell induces a lattice strain on the surface layer, which leads to a downshift in the d-band center of Pt as a result of the ligand effect from the transition metal in the core [29], [30] According to Schlapka et al., this ligand effect would considerably be reduced if the Pt-rich shell thickness is beyond four Pt monolayers (approximately 1 nm) [115]. In this case, the ligand effect and consequently the compressive strain on the surface can be neglected, assuming that the presence of the transition metal four monolayers beneath the surface has a negligible impact on the electronic structure. In this regard, we can assume that smaller particles, poor in Ni and exhibiting thicker Pt-rich shells, have surfaces similar to that of pure Pt, particularly with the same lattice parameter. Therefore, the re-deposition of Pt on the surface of these smaller particles will cause minimal lattice mismatch between the newly deposited material and the original particle. On the other hand, due to the shift in the d-band center of Pt in particles with thin Pt-rich shells, these particles have lower binding energy for Pt single atoms, compared to pure Pt particles or those with thick Pt shells. As a result, dissolved Pt atoms present on the carbon support are more prone to re-deposit on smaller particles with higher amount of Pt and thicker Pt-rich surface layers. As shown in Figure 6-11a, particle 1 had initially considerably higher amount of Pt than the neighboring particles, while particle 2 had a Pt-rich layer of about 2 nm, precisely on the area where the deposition later occurred. In summary, it seems that the re-deposition of single atoms on these particles is thermodynamically preferred due to the lower lattice mismatch and higher Pt-Pt binding energy on the surface.

Another important observation is the change in composition among various particles. As shown in Figure 6-12 (as well as Figure 6-12), the percolated structure of particles with Pt-rich and Ni-rich regions in the core became more homogenous inside the particle. It seems that the Pt atoms from Pt-rich regions inside the particles diffused to the surfaces to form a clear core-shell structure.

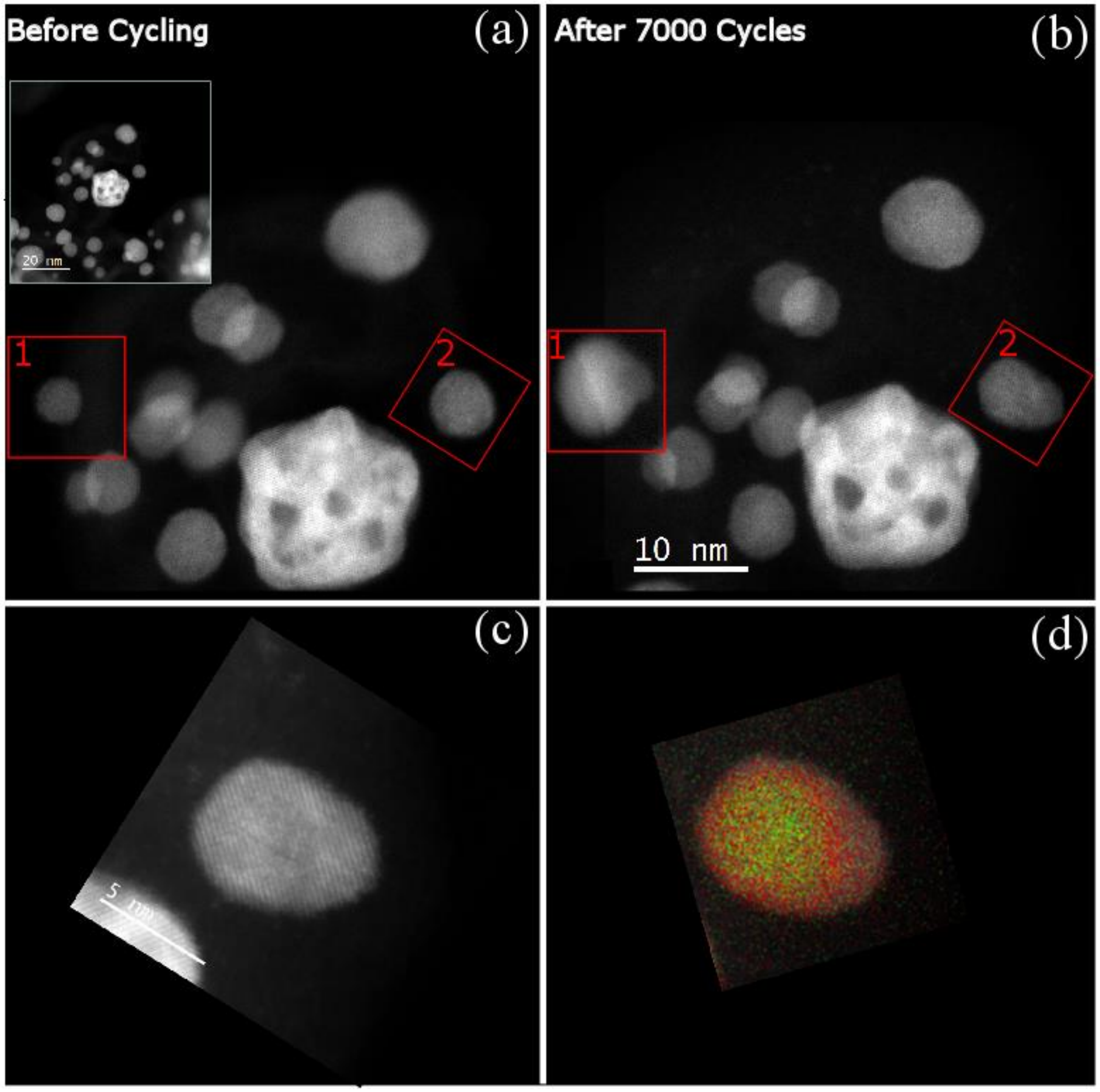

Figure 6-10 a) and b) HAADF STEM images of Pt-Ni NPs before and after voltage cycling, respectively, c) high magnification HAADF STEM image of the particle 2 after 7000 cycles showing a continuous lattice between the newly deposited material and the original particle and d) EDS mapping of particle 2 after 7000 cycles.

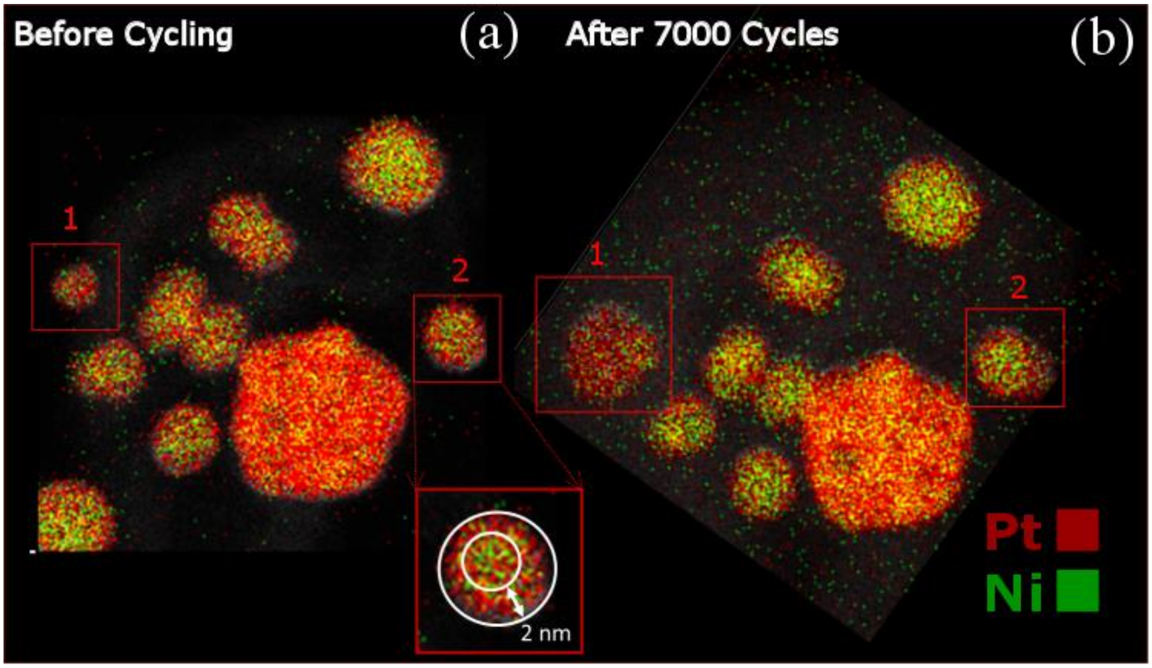

Figure 6-11 EDS mapping of Pt-Ni NPs before and after voltage cycling, showing the heterogeneous deposition of Pt on particles 1 and 2.

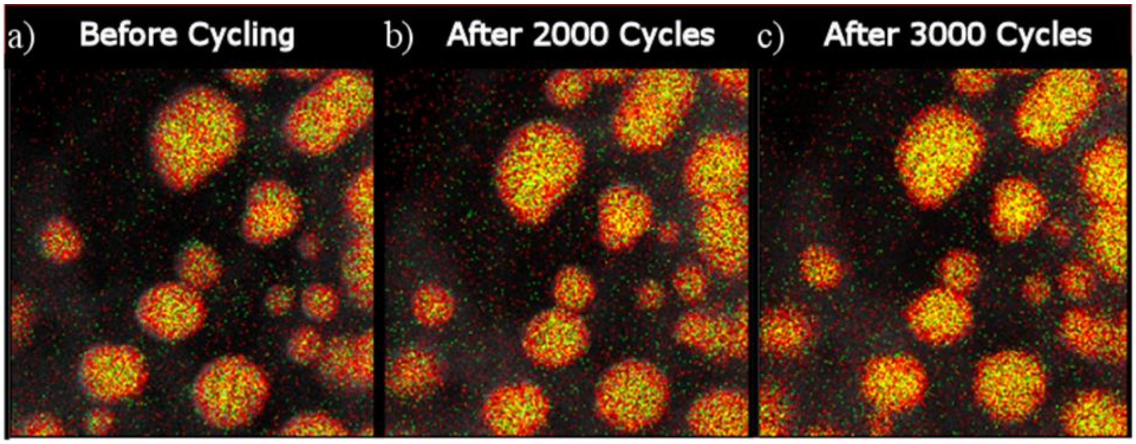

Figure 6-12 EDS mapping of Pt-Ni NPs before and after voltage cycling showing the change in composition distribution inside the core of the NPs.

6.3.2 Pt-Co Nanocatalysts

Figure 6-13 compares the Pt_3Co NPs after 2000 and 5000 potential cycling. As shown in these images, particle dissolution and particle movement happens simultaneously during potential cycling. Almost all of the particles change their location on the surface of carbon support. For instance, particle 1 located at the edge of the carbon support in Figure 6-13a, moves away from the edge in Figure 6-13b. Similarly, particles 2 and 3 change their relative position. As it was shown in the previous sections, this can be due to a change in the shape of carbon support due voltage, in addition to the particle movement on the surface of carbon as a result of carbon corrosion. Since carbon has a 3D convoluted shape, the details of the changes in the carbon support are not clear from the 2-D projected STEM images. However, the fact that some of the particles are in focus and some are out of focus reveals that the particle are located at different heights relative to the eccentric height.

Particle dissolution is another phenomenon that can be observed by comparing Figure 6-13a and b. In particular, particle 4 has completely disappeared, while particles 5 and 6 shrink considerably. This is due to the dissolution of particles as a result of potential cycling. The considerable increase in the amount of single atoms and atomic clusters in the vicinity of those particles confirms particle dissolution. This is clearer in Figure 6-13d and C, which show a high magnification dark and bright field images of the particles subjected to dissolution. One might consider the probability of movement of particles 4 and 6 to the region behind particles 7 and 8, instead of dissolution. However, this probability is revoked

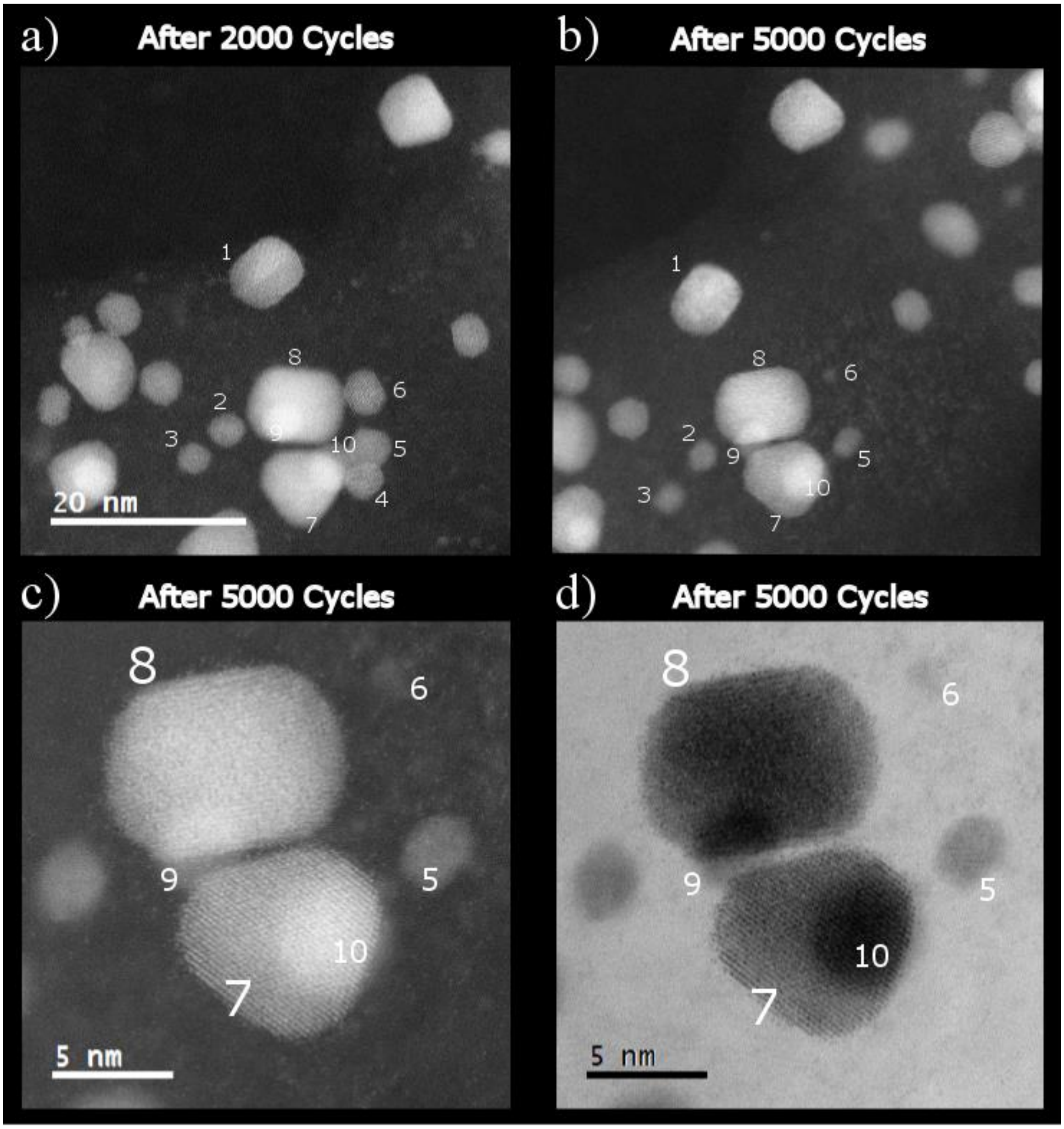

Figure 6-13 HAADF STEM images of the Pt_3Co NPs a) after 2000 cycles, and b) after 5000 cycles, c) and d) high magnification dark field and bright field images of the particles labeled as 5-10.

by looking at the bright field image of this area in Figure 6-13d which shows that the overlapping is related to particle 9 and 10 which were already overlapped with particles 7 and 8 in Figure 6-13a.

Figure 6-14 is another example of particle dissolution where the particle size is reduced as a result of dissolution. Figure 6-14c illustrates the overlapping of the particle after 2000 cycles in red and the one after 5000 cycles in green. Thus the red area in the overlapped image demonstrate the part that has been subjected to dissolution. Similarly to PtNi particles, dissolution happens at the corners and steps of Pt_3Co particles due to their high curvature and consequently high surface energy.

After dissolution, single atoms and atomic clusters are very mobile and unstable on the surface of carbon support and thus are prone to deposit on the surface of other particles to reduce their energy. Figure 6-15 illustrates the deposition on the surface of a large particle. The NP exhibits an ordered structure throughout as confirmed by the superlattice {100} type spots shown in the FFT of Figure 6-15a., The overlapping of the particle before and after potential cycling in red and green, respectively, shows that the deposition happens on 100 surface planes.

Another important observation is the change in the shape of NPs during potential cycling. As it is shown in Figure 6-16, the particle lose its sharp corners and edges and become more spherical under the effect of voltage in contact with electrolyte. This can be either due to the dissolution of high energy edges and deposition on low surface planes, to reduce the surface energy or a result of surface diffusion of atoms from low coordinated high energy sites to lower energy area on the surface. Similar surface modification has been

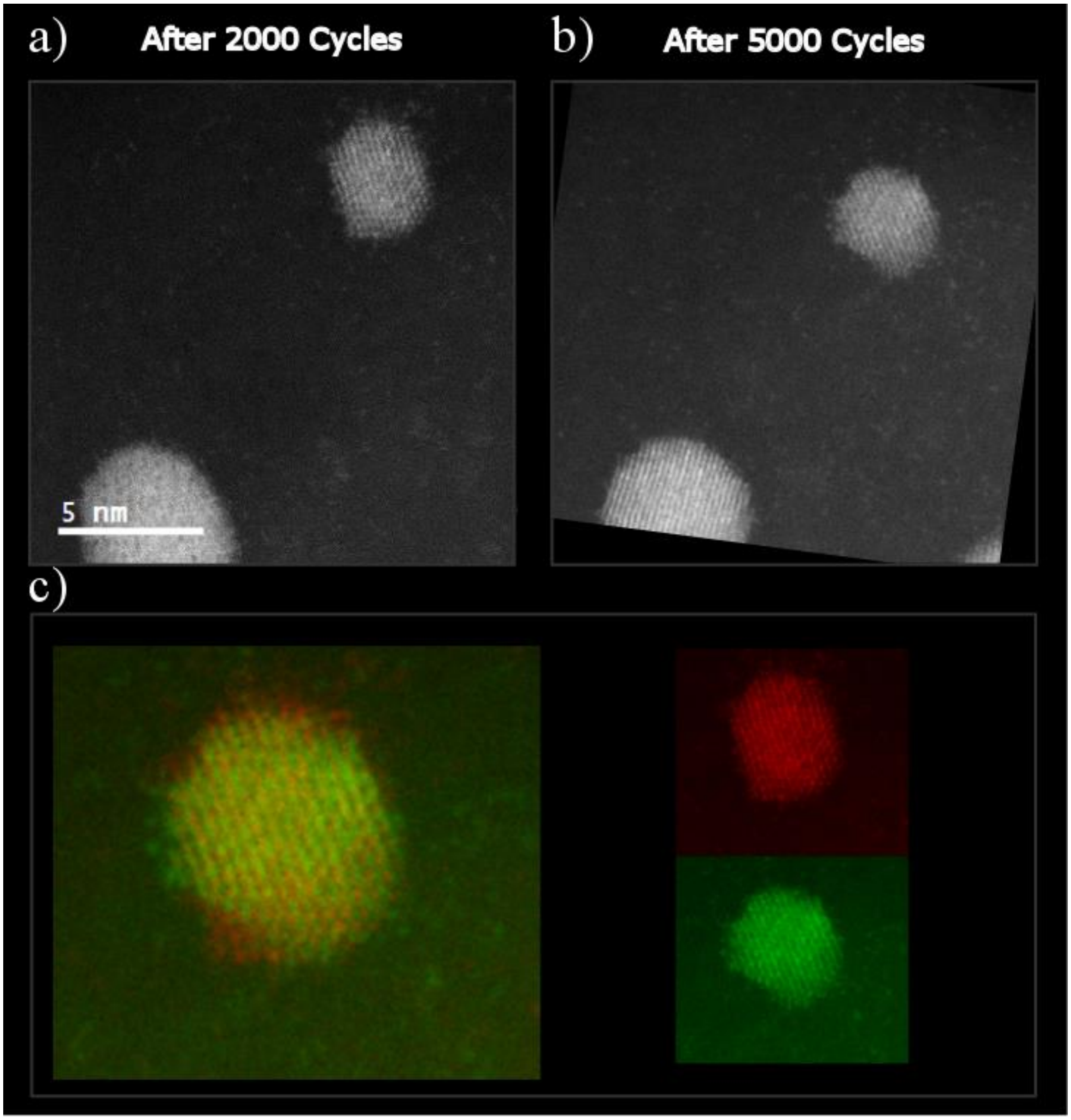

Figure 6-14 HAADF STEM images of a small Pt_3Co NP a) after 2000 cycles and b) after 5000 cycles, c) overlapping of the particle after 2000 cycles in red and after 5000 cycles in green.

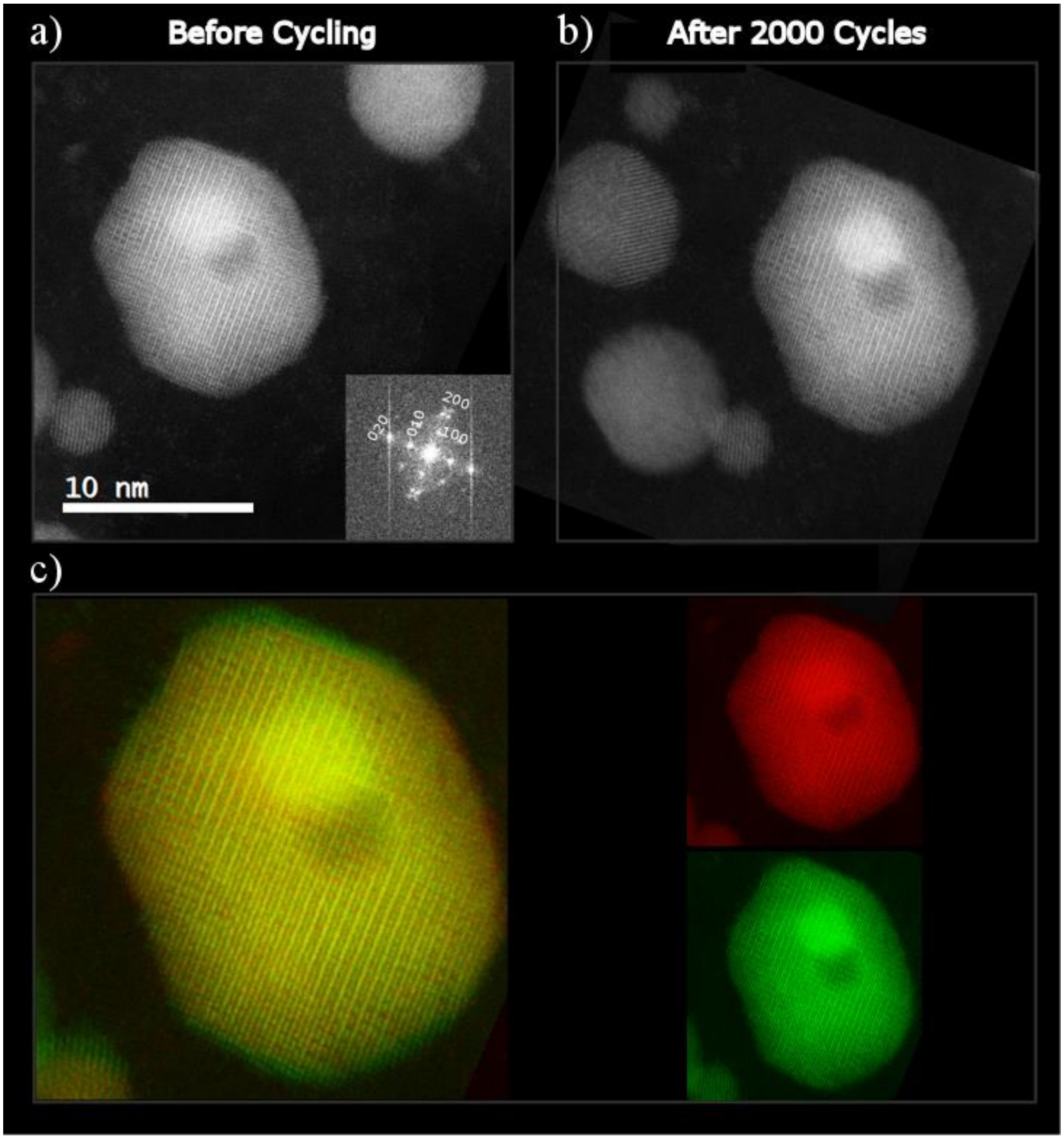

Figure 6-15 HAADF STEM images of a large Pt_3Co NPs a) before and b) after 2000 potential cycling, c) overlapping of the particle before and after potential cycling in red and green, respectively, showing re-deposition occurs on the surface of the large particle.

reported for Pt shaped controlled hexagonal nanoparticles and Pd cubic nanocatalysts in alkaline environment. The increased roundness and surface modification during potential cycling has a deteriorative effect on site selective nanocatalysts as they lose their catalytically active sharp edges and corners during fuel cell operation.

Modification in the composition distribution is another source of degradation for Pt alloy nanocatalysts. Figure 6-17 shows the HAADF STEM images along with EDS mapping of the nanoparticles inside the red boxes labeled 1 and 2 before and after potential cycling. In these images Pt and Co are illustrated in red and green respectively. Co leaching outside of the particles happen for all of the particles. However, it occurs more severely for smaller particles than the larger ones. The small particles shown in Figure 6-17c and d (EDS mapping of box 2) are almost depleted in Co while larger particles only reduce their Co content. In smaller NPs, the fraction of surface atoms with respect to bulk atoms increases, and thus smaller NPs are more prone to Co leaching due to the higher density of low coordination surface sites. This results in the formation of a thicker Pt-rich layer and higher Pt/Ni ratio in these particles.

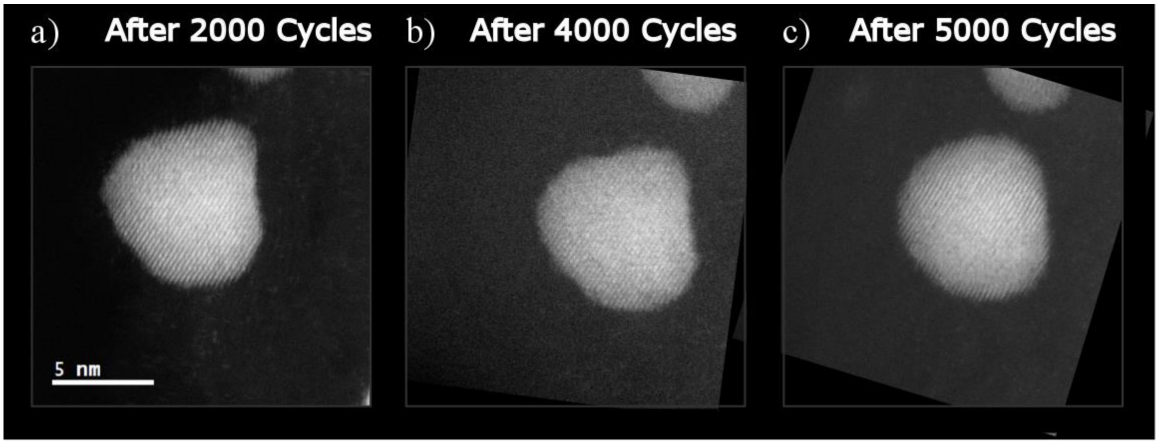

Figure 6-16 morphology modification of a Pt_3Co NP

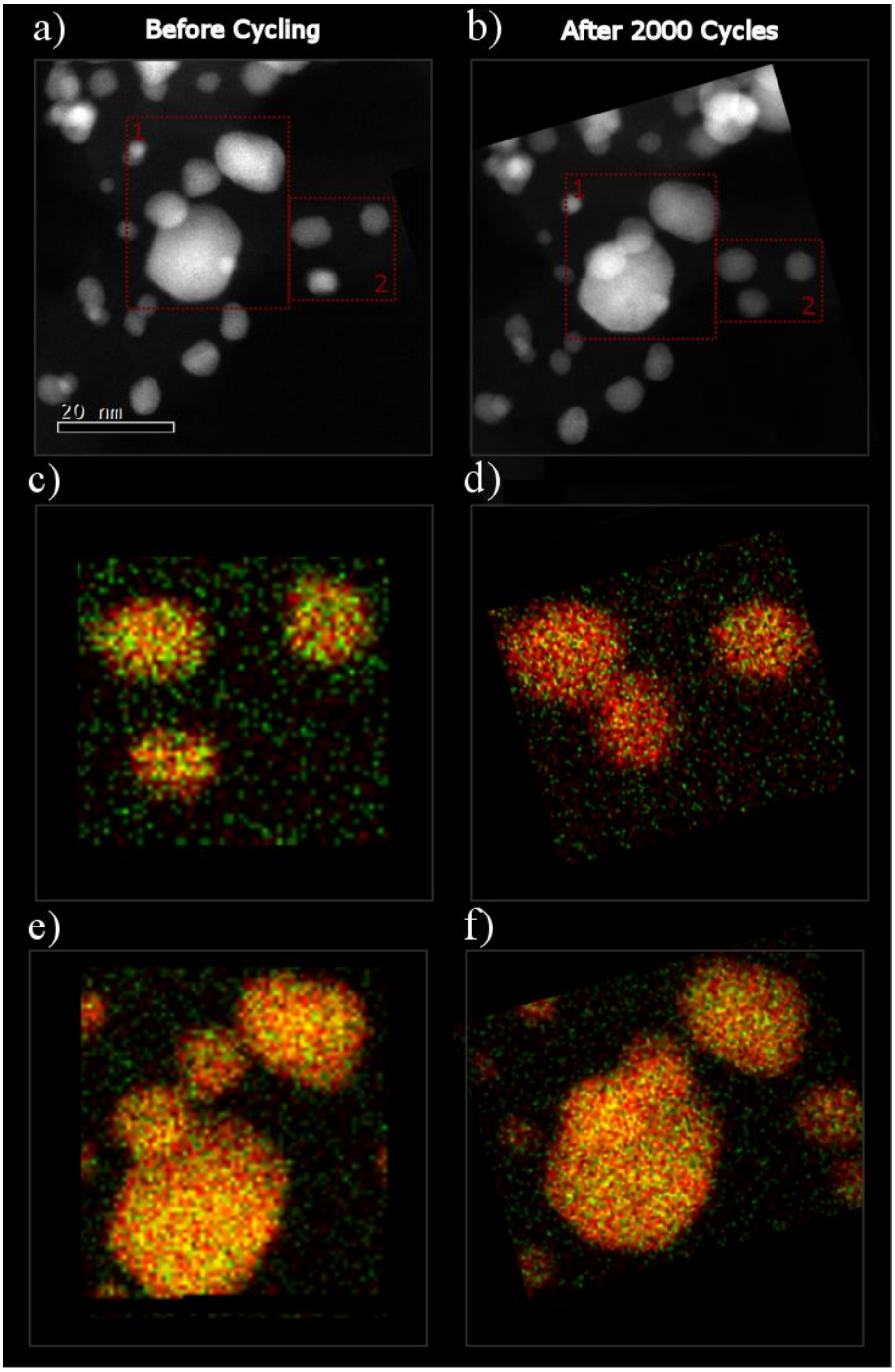

Figure 6-17 AADF STEM images of Pt3Co NPs a) before and b) after 2000 cycles, c) and d) EDS Mapping of the NPs in box 2, e) and f) EDS mapping of the NPs in box 1.

Chapter 7: Conclusions

To fundamentally understand the degradation mechanisms of Pt and Pt alloy nanocatalysts in the cathode of PEM fuel cell during potential cycling, both post mortem parametric TEM and identical location S/TEM studies have been performed on MEAs and nanocatalysts particles, respectively. Post-mortem TEM analysis of the MEAs after 10K voltage cycling produced a general understanding of the surface area loss mechanisms under realistic fuel cell conditions, while the identical location study provided direct evidence for each mechanism.

In the first part, the degradation of the cathode side of four different MEAs after 10K potential cycles was studied, by changing the humidity conditions, upper limit potential and temperature. The experiments show that the most severe particle growth, the largest particle loss from the cathode, and the highest particle precipitation in the membrane occur in the MEAs operated under high potential. This, in turn, results in the loss of the active surface area of the catalyst nanoparticles. On the other hand, no significant particle growth and particle loss happens in the low humidity sample. It is well known that a high potential accelerates particle dissolution, while low humidity restricts the ion transport in the ionomer. Thus, it can be concluded that to restrict the nanocatalysts degradation on the cathode of the MEAs, it is critical to control the Pt dissolution and diffusion in the cathode as a main mechanism of surface area loss. Moreover, two different particle morphologies can be found inside the cathode, spherical particles arising from Ostwald ripening and non-spherical particles resulting from aggregation and coalescence of two or more particles. The highest and the lowest amount of non-spherical aggregated particles in the high potential and low humidity MEAs, respectively, in addition to the increasing amount of coalescence inside the cathode in regions closer to the cathode/membrane interface show a significant role of particle dissolution and ion migration on the coalescence of particles. This is in contrast to the belief that particle movement on the cathode causes coalescence. Given the data, two mechanisms are proposed to be responsible for particle aggregation and coalescence: deposition of dissoluble Pt between two particles with consequent bridging, and modified electrochemical Ostwald ripening until adjacent particles make a contact to each other and finally coalesce. Evidence of these mechanisms for coalescence is provided by EDS analysis of the particles. It is also observed that the amount of Co in the spherical particles increases with the particle size. This can be explained by the formation of Pt-rich surfaces on the larger particles through the deposition of dissoluble Pt on the surfaces via Ostwald ripening which restrict Co leaching from the larger particles. Note, that the deposition of dissoluble Co does not happen because of the low enthalpy of mixing. In addition, we observe that the atomic fraction of Co in the non- spherical aggregated particles is independent of size. An EDS analysis of the particles aggregated through the bridging mechanism shows very low amounts of Co (less than 3 at%) while the amount of Co in particles resulting from necking of spherical particles depends on the size of those individual particles. Further EDS analysis across the cathode shows an increase in Co atomic fraction by decreasing the distance to the membrane the high potential and high temperature samples. However, near the membrane inside the cathode Co at% drops significantly due to the higher amount of coalescence via Pt preferential deposition between particles with consequent bridging. Finally, two types of particle morphologies precipitated in the membrane are identified, dendritic polycrystalline particles in regions nearby the cathode/membrane interface, and faceted single crystalline particles in regions far from the interface. Both types contain only Pt, as Co cannot precipitate because of the small enthalpy of mixing and low reduction potential of Co ions.

To understand the details about each degradation mechanism, the second part of this thesis focused on analyzing the behavior of Pt NPs supported on carbon nanotubes and amorphous carbon at different stages of fuel cell cycling through identical location S/TEM. The reason why carbon nanotubes are used for this part is due to their simpler morphology, compared to the complicated 3-D morphology of carbon black. The convoluted 3-D structure of carbon black makes it difficult to interpret the actual location of the NPs on the carbon support from the 2D projected TEM images.

Through direct observations, it is demonstrated that, in the first 1000 cycles, the main mechanism responsible for the loss of electrochemical active surface area of Pt/CNT electrocatalysts is particle motion, followed by coalescence. Severe structural deformation of the carbon nanotubes during voltage cycling is another source of degradation. The wave-like structure of the carbon formed after voltage cycling is the result of the appearance of the defect sites on the carbon nanotubes, which convert the flat hexagon structure to curved heptagon and pentagon carbon rings. In order to understand if there is any correlation between carbon degradation and particle movement on the carbon support, carbon degradation was accelerated under the electron beam, while the behavior of the nanoparticles was observed. It is shown that the particles start to move as soon as carbon atoms at the interface of the carbon/particle interface are removed. During voltage cycling, carbon corrosion occurs through a series of reactions at the carbon/ionomer, ionomer/particle, and carbon/particle interfaces. These reactions result in the formation of carbon dioxide and removal of carbon atoms at the particle/carbon interface. When carbon atoms at the carbon/particle interface are removed from the surface of carbon, leaving a carbon defect site, the particle tends to make new bonds with the next carbon atoms to possibly decrease its free surface energy. In the next 1000 cycles, single atoms and atomic clusters appeared on the ionomer phase at the surface of carbon nanotubes as a result of dissolution. These single atoms and atomic clusters move subsequently toward large particles and deposit on their surfaces. The atomic clusters will either dissolve again to single atoms or ions and redeposit on the large particles or move toward particles and redeposit between them with consequent bridging.

Similarly to Pt NPs on carbon nanotubes, particle migration and coalescence and particle dissolution are shown to be responsible for the degradation of Pt NPs supported on amorphous carbon (CB). However, particles seem to be more mobile on the surface of CNTs than amorphous carbon. This can be due to the difference in morphology between CNT and CB. Amorphous carbon exhibits a convoluted 3D structure, in contrast to carbon nanotubes with a flat surface. As a result, the particles on the surface of carbon black are likely to have larger fraction of surface area in contact with carbon than particles supported on CNTs. Thus, more vacancies are needed at the carbon/particle interface for particles to start their motion.

In the last part of this work, the behavior of Pt alloy nanocatalysts such as PtNi and PtCo supported on amorphous carbon was investigated during the various stages of fuel cell potential cycling, using identical location aberration-corrected STEM. For PtNi NPS, the characterization of the initial powder shows that most of the particles exhibit a disordered structure where Pt and Ni form a face centered cubic solid solution. This structure shows a heterogeneous composition distribution, where Pt-rich and Ni-rich regions are observed within the nanoparticles. Although most of the nanoparticles exhibit a solid solution, others show a partially ordered $L1_0$ structure. It is also shown that Pt seems to segregate to the surface of the nanoparticles. The Pt concentration and the thickness of the Pt-rich shell are higher in smaller particles compared to larger ones. During the initial voltage cycling, carbon corrosion occurs, which leads to particle motion; however, no particle coalescence could be observed. After 2000 cycles, single atoms and atomic clusters appear on the carbon support. In some cases, a nanoparticle exhibits both dissolution and re-deposition at the same time. Our experiments also showed for the first time direct evidence of heterogeneous re-deposition of Pt on the surface of smaller particles rather than larger ones, which contradicts the traditional view of the Ostwald ripening mechanism. This can be due to the thicker Pt-rich shell of smaller particles, which act as nucleation sites for Pt re-deposition. It seems that the re-deposition of single atoms on these particles is thermodynamically preferred due to the lower lattice mismatch and higher Pt-Pt binding energy on the surface. The comparison between the composition distribution of the nanoparticles before and after voltage cycling shows the formation of a clear core-shell structure after cycling.

Particle migration and particle dissolution are also observed for Pt_3Co NPs supported on amorphous carbon during potential cycling. In case of Pt_3Co, it was shown that Co leaching occurs more severely for smaller particles that larger ones. Particles smaller than 5 nm are almost depleted in Co. Another degradation source is the modification in the morphology of particles which happens more severely in Pt_3Co than PtNi NPs during potential cycling. The particles lose their sharp corners and edges and become more spherical under the effect of voltage. The increased roundness has a deteriorative effect on site selective nanocatalysts as they lose their catalytically active sharp edges and corners during fuel cell operation.

References

[1] E. F. Holby, W. Sheng, Y. Shao-Horn, and D. Morgan, "Pt nanoparticle stability in PEM fuel cells: influence of particle size distribution and crossover hydrogen," *Energy Environ. Sci.*, vol. 2, no. 8, p. 865, 2009.

[2] V. Jalan and E. J. Taylor, "Importance of Interatomic Spacing in Catalytic Reduction of Oxygen in Phosphoric Acid," *Journal of the Electrochemical Society*, vol. 130, no. 11. pp. 2299–12302, 1983.

[3] D. A. Landsman and F. J. Luczak, "Handbook of Fuel Cells: Fundamentals, Technology and Applications." John Wiley & Sons, Chichester, 2003.

[4] H. A. Gasteiger, S. S. Kocha, B. Sompalli, and F. T. Wagner, "Activity benchmarks and requirements for Pt, Pt-alloy, and non-Pt oxygen reduction catalysts for PEMFCs," *Appl. Catal.*, vol. 56, no. 1–2. pp. 9–35, 2005.

[5] V. R. Stamenkovic *et al.*, "Trends in electrocatalysis on extended and nanoscale Pt-bimetallic alloy surfaces," *Nat. Mater.*, vol. 6, no. 3. pp. 241–247, 2007.

[6] P. J. Ferreira *et al.*, "Instability of Pt⁄C Electrocatalysts in Proton Exchange Membrane Fuel Cells," *J. Electrochem. Soc.*, vol. 152, no. 11, p. A2256, 2005.

[7] Y. Shao-Horn, W. C. Sheng, S. Chen, P. J. Ferreira, E. F. Holby, and D. Morgan, "Instability of supported platinum nanoparticles in low-temperature fuel cells," *Top. Catal.*, vol. 46, no. 3–4, pp. 285–305, 2007.

[8] P. J. Ferreira and Y. Shao-Horn, "Formation Mechanism of Pt Single-Crystal Nanoparticles in Proton Exchange Membrane Fuel Cells," *Electrochemical and*

Solid State Letters, vol. 10, no. 3. pp. B60–B63, 2007.

[9] J. A. Gilbert *et al.*, “In-Operando Anomalous Small-Angle X-Ray Scattering Investigation of Pt 3 Co Catalyst Degradation in Aqueous and Fuel Cell Environments,” *J. Electrochem. Soc.*, vol. 162, no. 14, pp. F1487–F1497, Oct. 2015.

[10] S. Chen, H. A. Gasteiger, K. Hayakawa, T. Tada, and Y. Shao-Horn, “Platinum-Alloy Cathode Catalyst Degradation in Proton Exchange Membrane Fuel Cells: Nanometer-Scale Compositional and Morphological Changes,” *J. Electrochem. Soc.*, vol. 157, no. 1, p. A82, 2010.

[11] M. Gummalla *et al.*, “Effect of Particle Size and Operating Conditions on Pt3Co PEMFC Cathode Catalyst Durability,” *Catalysts*, vol. 5, no. 2, pp. 926–948, 2015.

[12] L. Dubau, F. Maillard, M. Chatenet, L. Guetaz, J. André, and E. Rossinot, “Durability of Pt3Co/C Cathodes in a 16 Cell PEMFC Stack: Macro/Microstructural Changes and Degradation Mechanisms,” *J. Electrochem. Soc.*, vol. 157, no. 12, p. B1887, 2010.

[13] R. Borup *et al.*, “Scientific aspects of polymer electrolyte fuel cell durability and degradation,” *Chem. Rev.*, vol. 107, no. 10, pp. 3904–3951, 2007.

[14] R. . Hayre, W. Colella, S. . Cha, and F. . Prinz, *Fuel Cell Fundamentals*. New York: John Wiley & Sons, 2009.

[15] L. Hui, *Proton Exchange Membrane Fuel Cells: Contamination and Mitigation Strategies*. New York: CRC Press, 2010.

[16] J. Larminie and A. Dicks, *Fuel Cell Systems Explained*. Chichester: John Wiley & Sons, 2001.

[17] S. Srinivasan, R. Mosdale, P. Stevens, and C. Yang, “Fuel cells: Reaching the Era of Clean and Efficient Power Generation in the Twenty-First Century,” *Annu. Rev. Energy Environ.*, vol. 24, no. 1, pp. 281–328, 1999.

[18] B. D. McNicol, D. A. J. Rand, and K. R. Williams, “Fuel cells for road transportation purposes — yes or no?,” *J. Power Sources*, vol. 100, no. 1–2, pp. 47–59, 2001.

[19] A. Hamnet, “Energy Storage in Lead-Acid Batteries: The Faraday Way to Sustainability,” *Phil. Trans. R. Soc. Lond. A*, vol. 354, pp. 1529–1544, 1996.

[20] *U.S. Department of Energy, Fuel Cell Handbook, 5th ed., U.S. Department of Energy, Morgantown*. West Virginia, 2000.

[21] S. Gottesfeld and T. A. Zawodzinski, *Electrolyte Fuel Cells*. Weinheim: Wiley-VCH, 1997.

[22] D. A. Landsman and F. J. Luczak, *Catalyst studies and coating technologies. In Handbook of fuel cells: Fundamentals, technology and applications, Vol. 3: Fuel cell technology and applications*. New York: John Wiley & Sons, 2003.

[23] D. A. Landsman, “US Patent,” 4,316,944, 1982.

[24] D. Thompsett, *Handbook of Fuel Cells – Fundamentals, Technology and Applications,*. Chichester: Wiley, 2003.

[25] E. Christoffersen, P. Liu, A. Ruban, H. L. Skriver, and and J. K. Norskov., “Anode Materials for Low-Temperature Fuel Cells: A Density Functional Theory Study,” *Journal of Catalysis*, vol. 199. pp. 123–131, 2001.

[26] V. R. Stamenkovic *et al.*, “Improved oxygen reduction activity on Pt3Ni (111) via increased surface site availability,” *Science*, vol. 315. pp. 493–497, 2007.

[27] J. R. Norskov *et al.*, “Origin of the Overpotential for Oxygen Reduction at a Fuel-Cell Cathode,” *Journal of Physical Chemistry B,* vol. 108. pp. 17886–17892, 2004.

[28] B. Hammer and J. K. Norskov, “Theoretical surface science and catalysis--calculations and concepts,” *Adv. Catal.*, vol. 45. pp. 71–129, 2000.

[29] R. R. Adzic *et al.*, “Platinum Monolayer Fuel Cell Electrocatalysts,” *Top. Catal.*, vol. 46. pp. 249–262, 2007.

[30] J. Zhang, M. B. Vukmirovic, Y. Xu, M. Mavrikakis, and R. R. Adzic, “Controlling the Catalytic Activity of Platinum-Monolayer Electrocatalysts for Oxygen Reduction with Different” *Angew. Chemie Int. Ed.*, vol. 44, no. 14, pp. 2132–2135, 2005.

[31] Huang, Y. . Zhang, J. . Kongkanand, A. . Wagner, F. T. . J. Li, and J. Jorne, “Transient Platinum Oxide Formation and Oxygen Reduction on Carbon-Supported Platinum and Platinum-Cobalt Alloy Electrocatalysts,” *J. Electrochem. Soc.*, vol. 161, no. 1. pp. F10--F15, 2014.

[32] S. Mukerjee and S. Srinivasan, “Enhanced electrocatalysis of oxygen reduction on platinumalloys in proton exchange membrane fuel cells,” *Journal of Electroanalytical Chemistry*, vol. 357. pp. 201–224, 1993.

[33] H. R. Colon-Mercado and B. N. Popov, “Stability of Platinum Based Alloy Cathode Catalysts in PEM Fuel Cells,” *J. Power Sources*, vol. 155. p. 253--263., 2006.

[34] C. Wang *et al.*, “Monodisperse Pt3Co Nanoparticles as a Catalyst for the Oxygen Reduction,” *J. Phys. Chem.*, vol. 113. pp. 19365–19368, 2009.

[35] B. Patrick, H. C. Ham, Y. Shao-Horn, L. F. Allard, G. S. Hwang, and P. J. Ferreira,

"Atomic structure and composition of Pt3Co" nanocatalysts in fuel cells: An aberration-corrected STEM HAADF study," *Chem. Mater.*, vol. 25, no. 4, pp. 530–535, 2013.

[36] U. A. Paulus *et al.*, "Oxygen reduction on high surface area Pt-based alloy catalysts in comparison to well defined smooth bulk alloy electrodes," *Electrochem. Acta*, vol. 47. pp. 3787–3798, 2002.

[37] J. Zhang, M. B. Vukmirovic, K. Sasaki, A. U. Nilekar, M. Mavrikakis, and R. R. Adzic, "Mixed-metal Pt monolayer electrocatalysts for enhanced oxygen reduction kinetics," *J. Am. Chem. Soc.*, vol. 127, no. 36, pp. 12480–12481, 2005.

[38] J. Zhang, Y. Mo, M. B. Vukmirovic, R. Klie, K. Sasaki, and R. R. Adzic, "Platinum monolayer electrocatalysts for O2 reduction: Pt monolayer on Pd(111) and on carbon-supported Pd nanoparticles," *J. Phys. Chem. B*, vol. 108, no. 30, pp. 10955–10964, 2004.

[39] P. Mani, R. Srivastava, and P. Strasser, "Dealloyed Pt-Cu core-shell nanoparticle electrocatalysts for use in PEM fuel cell cathodes," *J. Phys. Chem. C*, vol. 112, no. 7, pp. 2770–2778, 2008.

[40] S. Koh and P. Strasser, "Electrocatalysis on bimetallic surfaces: Modifying catalytic reactivity for oxygen reduction by voltammetric surface dealloying," *J. Am. Chem. Soc.*, vol. 129, no. 42, pp. 12624–12625, 2007.

[41] R. Srivastava, P. Mani, N. Hahn, and P. Strasser, "Efficient oxygen reduction fuel cell electrocatalysis on voltammetrically dealloyed Pt-Cu-Co nanoparticles," *Angew. Chemie - Int. Ed.*, vol. 46, no. 47, pp. 8988–8991, 2007.

[42] Y. X. and S. Ye, “Recent advances in activity and durability enhancement of Pt/C catalytic cathode in PEMFC: Part II: Degradation mechanism and durability enhancement of carbon supported platinum catalyst,” *J. Power Sources*, vol. 172, p. 145, 2007.

[43] Y. Shao *et al.*, “The influence of the electrochemical stressing (potential step and potential-static holding) on the degradation of polymer electrolyte membrane fuel cell electrocatalystsNo Title,” *J. Power Sources*, vol. 280, p. 280, 2008.

[44] S. Kocha, “Electrochemical Degradation: Electrocatalyst and Support Durability,” in *Polymer Electrolyte Fuel Cell Degradation*, M. M. Mench, E. C. Kumbur, and T. N. Veziroglu, Eds. Oxford: Academic Press, 2012, p. 89.

[45] W. H. Yuan X.-Z., Li H., Zhang S., Martin J., “A review of polymer electrolyte membrane fuel cell durability test protocols,” *J. Power Sources*, vol. 196, p. 9107, 2011.

[46] V. S. Murthi, R. C. Urian, and S. Mukerjee, “Oxygen Reduction Kinetics in Low and Medium Temperature Acid Environment: Correlation of Water Activation and Surface Properties in Supported Pt and Pt Alloy Electrocatalysts,” *J. Phys. Chem. B*, vol. 108, pp. 11011–11023, 2004.

[47] J. H. Cynthia A. Ricea, Patrick Urchaga, Antonio O. Pistono, Bryce W. McFerrin, Benjamin T. McComb, “Platinum Dissolution in Fuel Cell Electrodes: Enhanced Degradation from Surface Area Assessment in Automotive Accelerated Stress Tests,” *J. Electrochem. Soc.*, vol. 162, p. F1175, 2015.

[48] J. W. Alina Marcua, Gabor Totha, Patrick Pietraszb, “Cathode catalysts degradation

mechanism from liquid electrolyte to membrane electrode assembly," *Comptes Rendus Chim.*, vol. 17, p. 752, 2014.

[49] B. J. Eastwood, P. A. Christensen, R. D. Armstrong, and N. R. Bates, "Electrochemical oxidation of a carbon black loaded polymer electrode in aqueous electrolytes," *J. Solid State Electrochem.*, vol. 3, no. 4, pp. 179–186, May 1999.

[50] J. Willsau and J. Heitbaum, "The influence of Pt-activation on the corrosion of carbon in gas diffusion electrodes—A dems study," *J. Electroanal. Chem. Interfacial Electrochem.*, vol. 161, no. 1, pp. 93–101, 1984.

[51] D. A. Stevens and J. R. Dahn, "Thermal degradation of the support in carbon-supported platinum electrocatalysts for PEM fuel cells," *Carbon N. Y.*, vol. 43, no. 1, pp. 179–188, 2005.

[52] D. a. Stevens, M. T. Hicks, G. M. Haugen, and J. R. Dahn, "Ex Situ and In Situ Stability Studies of PEMFC Catalysts," *J. Electrochem. Soc.*, vol. 152, no. 12, p. A2309, 2005.

[53] T. Akita *et al.*, "Analytical TEM study of Pt particle deposition in the proton-exchange membrane of a membrane-electrode-assembly," *J. Power Sources*, vol. 159, no. 1 SPEC. ISS., pp. 461–467, 2006.

[54] E. Guilminot, A. Corcella, F. Charlot, F. Maillard, and M. Chatenet, "Detection of Pt Ions and Pt Nanoparticles Inside the Membrane of a Used PEMFC," *J. Electrochem. Soc.*, vol. 154, no. May 2010, p. B96, 2007.

[55] E. Guilminot, A. Corcella, M. Chatenet, and F. Maillard, "Comparing the thin-film rotating disk electrode and the ultramicroelectrode with cavity techniques to study

carbon-supported platinum for proton exchange membrane fuel cell applications," *J. Electroanal. Chem.*, vol. 599, no. 1, pp. 111–120, 2007.

[56] J. Zhang, B. a. Litteer, W. Gu, H. Liu, and H. a. Gasteiger, "Effect of Hydrogen and Oxygen Partial Pressure on Pt Precipitation within the Membrane of PEMFCs," *J. Electrochem. Soc.*, vol. 154, no. 10, p. B1006, 2007.

[57] H. A. Gasteiger and J. Garche, *Handbook of Heterogeneous Catalysis, 2nd ed*. Weinhaim: Wiley-VCH, 2008.

[58] R. M. Darling and J. P. Meyers, "KiCells Model of Platinum Dissolution in PEMFCs," *Journal of the electrochemical Society*, vol. 150. pp. A1523--A1527, 2003.

[59] D. C. Johnson, D. T. Napp, and S. Bruckenstein, "A ring-disk electrode study of the current/potential behaviour of platinum in 1.0 M sulphuric and 0.1 M perchloric acids," *Electrochim. Acta*, vol. 15, no. 9, pp. 1493–1509, 1970.

[60] Y. Shao-Horn, W. C. Sheng, S. Chen, P. J. Ferreira, E. F. Holby, and D. Morgan, "Instability of Supported Platinum Nanoparticles in Low-Temperature Fuel Cells," *Top Catal.*, vol. 46. pp. 285–305, 2007.

[61] M. Uchimura, S. Sugawara, Y. Suzuki, J. B. Zhang, and S. S. Kocha, "Electrocatalyst Durability under Simulated Automotive Drive Cycles," *ECS Trans.*, vol. 16, no. 2, pp. 225–234, 2008.

[62] C. H. Paik, G. S. Saloka, and G. W. Graham, "Influence of Cyclic Operation on PEM Fuel Cell Catalyst Stability," *Electrochem. Solid-State Lett.*, vol. 10, no. 2, pp. B39–B42, 2007.

[63] C. G. Granqvist and R. A. Buhrman, “Size distributions for supported metal catalysts: Coalescence growth versus ostwald ripening,” *J. Catal.*, vol. 42, no. 3, pp. 477–479, 1976.

[64] P. Wynblatt and N. A. Gjostein, “Supported metal crystallites,” *Prog. Solid State Chem.*, vol. 9, pp. 21–58, 1975.

[65] S. B. Simonsen, I. Chorkendorff, S. Dahl, M. Skoglundh, J. Sehested, and S. Helveg, “Direct Observations of Oxygen-induced Platinum Nanoparticle Ripening Studied by In Situ TEM,” *J. Am. Chem. Soc.*, vol. 132, no. 23, pp. 7968–7975, Jun. 2010.

[66] M. Asoro, “Coalescence and Sintering in Metallic Nanoparticles:In-situ Transmission Electron Microscopy (TEM) Study, Ph.D. Dissertaion.” University of Texas at Austin, Austin, TX, 2012.

[67] K. Schlögl, M. Hanzlik, and M. Arenz, “Comparative IL-TEM Study Concerning the Degradation of Carbon Supported Pt-Based Electrocatalysts,” *J. Electrochem. Soc.*, vol. 159, no. 6, p. B677, 2012.

[68] Z. W. Shan, R. K. Mishra, S. A. Syed Asif, O. L. Warren, and A. M. Minor, “Mechanical annealing and source-limited deformation in submicrometre-diameter Ni crystals.,” *Nat. Mater.*, vol. 7, no. 2, pp. 115–119, 2008.

[69] G. C. Kuczynski, “Measurement of self-diffusion of silver without radioactive tracers,” *J. Appl. Phys.*, vol. 21, no. 7, pp. 632–635, 1950.

[70] A. G. Guy, *Essentials of Materials Science. 1976*. New York: McGraw Hill, 1976.

[71] W. D. Kingery and M. Berg, “Study of the initial stages of sintering solids by viscous flow, evaporation-condensation, and self-diffusion,” *J. Appl. Phys.*, vol. 26, no. 10,

pp. 1205–1212, 1955.

[72] C. Greskovich and K. W. Lay, “Grain Growth in Very Porous Al2O3 Compacts,” *J. Am. Ceram. Soc.*, vol. 55, no. 3, pp. 142–146, 1972.

[73] S. Mukerjee and S. Srinivasan, “Handbook of Fuel Cells-Fundamentals, Technology and Application,” H. A. G. W. Vielstich, A. Lamm, Ed. Chichester: Wiley, 2003, p. 502.

[74] M. Watanabe, K. Tsurumi, T. Mizukami, T. Nakamura, and and P. Stonehart, “Activity and Stability of Ordered and Disordered Co/Pt Alloys for Phosphoric Acid Fuel Cells,” *J. Electrochem. Soc.*, vol. 141. p. 2659, 1994.

[75] S. Chen, P. J. Ferreira, W. Sheng, N. Yabuuchi, L. F. Allard, and Y. Shao-Horn, “Enhanced Activity for Oxygen Reduction Reaction on Pt3Co Nanoparticles: Direct Evidence of Percolated and Sandwich-Segregation Structures,” *J. Am. Chem. Soc.*, vol. 130, no. 42, pp. 13818–13819, Oct. 2008.

[76] S. C. Ball, S. L. Hudson, B. R. Theobald, and D. Thompsett, “PtCo, a Durable Catalyst for Automotive PEMFC?,” *ECS Trans.*, vol. 11, no. 1, pp. 1267–1278, 2007.

[77] S. C. Ball, B. Theobald, D. Thompsett, and S. Hudson, “Enhanced Stability of PtCo catalysts for PEMFC,” in *ECS Transactions*, 2006, vol. 1, no. 8, pp. 141–152.

[78] V. R. Stamenkovic, B. S. Mun, K. J. J. Mayrhofer, P. N. Ross, and N. M. Markovic, “Effect of Surface Composition on Electronic Structure, Stability, and Electrocatalytic Properties of Pt-Transition Metal Alloys: Pt-Skin versus Pt-Skeleton Surfaces,” *J. Am. Chem. Soc.*, vol. 128, no. 27, pp. 8813–8819, Jul. 2006.

[79] A. Bonakdarpour *et al.*, “Studies of Transition Metal Dissolution from Combinatorially Sputtered, Nanostructured Pt1−xMx (M = Fe, Ni, 0<x<1) Electrocatalysts for PEM Fuel Cells,” *J. Electrochem. Soc.*, vol. 152, no. 1, p. A61, 2005.

[80] A. Bonakdarpour, K. Lake, K. Stevens, and J. R. Dahn, “Oxygen Reduction Activity of Magnetron-Sputtered Pt1−xCo x (0≤x≤0.5) Films,” *J. Electrochem. Soc.*, vol. 155, no. 2, p. B108, 2008.

[81] a. Bonakdarpour *et al.*, “Dissolution of Transition Metals in Combinatorially Sputtered Pt1−x−yMxMy′ (M, M′=Co, Ni, Mn, Fe) PEMFC Electrocatalysts,” *J. Electrochem. Soc.*, vol. 153, no. 10, p. A1835, 2006.

[82] S. Chen, W. Sheng, N. Yabuuchi, P. J. Ferreira, L. F. Allard, and and Y. Shao-Horn, “Origin of oxygen reduction reaction activity on Pt3Co nanoparticles: atomically resolved chemical compositions and structures,” *J. Phys. Chem. C.*, vol. 113. pp. 1109–1125, 2008.

[83] J. Prabhuram, X. Wang, C. L. Hui, and I.-M. Hsing, “Synthesis and Characterization of Surfactant-Stabilized Pt/C Nanocatalysts for Fuel Cell Applications,” 2003.

[84] W. Bi and T. F. Fuller, “Temperature Effects on PEM Fuel Cells Pt⁄C Catalyst Degradation,” *J. Electrochem. Soc.*, vol. 155, no. 2, p. B215, 2008.

[85] Hui Yang, Nicolás Alonso-Vante, A. Jean-Michel Léger, and C. Lamy, “Tailoring, Structure, and Activity of Carbon-Supported Nanosized Pt−Cr Alloy Electrocatalysts for Oxygen Reduction in Pure and Methanol-Containing Electrolytes,” 2004.

[86] W. Bi, Q. Suna, Y. Denga, and T. F. Fuller, “The effect of humidity and oxygen partial pressure on degradation of Pt/C catalyst in PEM fuel cell,” *Electrochimica Acta*, vol. 54. pp. 1826–1833, 2009.

[87] J. Zhang, *PEM fuel cell electrocatalysts and catalyst layers: fundamentals and applications*. London: Springer.

[88] J. Zhang *et al.*, “High temperature PEM fuel cells,” *J. Power Sources*, vol. 160, no. 2, pp. 872–891, 2006.

[89] A. Bard and L. Faulkner, “Allen J. Bard and Larry R. Faulkner, Electrochemical Methods: Fundamentals and Applications, New York: Wiley, 2001,” *Russ. J. Electrochem.*, vol. 38, no. 12, pp. 1505–1506, 2002.

[90] R. Greef, R. Peat, L. M. Peter, D. Pletcher, and J. Robinson, *Instrumental Methods in Electrochemistry*. Chichester: Ellis Horwood Ltd., 1985.

[91] K. J. J. Mayrhofer, M. Arenz, B. B. Blizanac, V. Stamenkovic, P. N. Ross, and N. M. Markovic, “CO surface electrochemistry on Pt-nanoparticles: A selective review,” in *Electrochimica Acta*, 2005, vol. 50, no. 25–26 SPEC. ISS., pp. 5144–5154.

[92] B. E. Conway and B. V. Tilak, “Interfacial processes involving electrocatalytic evolution and oxidation of H2, and the role of chemisorbed H,” *Electrochim. Acta*, vol. 47, no. 22–23, pp. 3571–3594, 2002.

[93] G. Jerkiewicz, “Electrochemical Hydrogen Adsorption and Absorption. Part 1: Under-potential Deposition of Hydrogen,” *Electrocatalysis*, vol. 1, no. 4, pp. 179–199, Dec. 2010.

[94] S. Pennycook and D. Jesson, "High-resolution incoherent imaging of crystals," *Phys. Rev. Lett.*, vol. 64, no. 8, pp. 938–941, Feb. 1990.

[95] E. Abe, "Electron microscopy of quasicrystals – where are the atoms?," *Chem. Soc. Rev.*, vol. 41, no. 20, p. 6787, 2012.

[96] J. Darling, R., Meyers, "Kinetic Model of Platinum Dissolution in PEMFCs," *J. Electrochem. Soc.*, vol. 150, pp. A1523–A1527, 2003.

[97] R. M. Darling and J. P. Meyers, "Mathematical Model of Platinum Movement in PEM Fuel Cells," *J. Electrochem. Soc.*, vol. 152, no. 1, p. A242, 2005.

[98] P. J. Ferreira and Y. Shao-Horn, "Formation Mechanism of Pt Single-Crystal Nanoparticles in Proton Exchange Membrane Fuel Cells," *Electrochemical and Solid-State Letters*, vol. 10, no. 3. pp. B60–B63, 2007.

[99] C. E. Carlton, S. Chen, P. J. Ferreira, L. F. Allard, and Y. Shao-Horn, "Sub-nanometer-resolution elemental mapping of Pt3Co nanoparticle catalyst degradation in proton-exchange membrane fuel cells," *J. Phys. Chem. Lett.*, vol. 3, no. 2, pp. 161–166, 2012.

[100] M. A. Asoro, P. J. Ferreira, and D. Kovar, "In situ transmission electron microscopy and scanning transmission electron microscopy studies of sintering of Ag and Pt nanoparticles," *Acta M*, vol. 81. pp. 173–183, 2014.

[101] A. K. Niessen, A. R. Miedema, F. R. Deboer, and and R. Boom, "Enthalpies of formation of liquid and solid binary alloys based on 3d metals: IV. Alloys of cobalt," *Physica B \& C*, vol. 151. pp. 401–432, 1988.

[102] M. R. Berber, T. Fujigaya, K. Sasaki, and N. Nakashima, "Remarkably Durable

High Temperature Polymer Electrolyte Fuel Cell Based on Poly(vinylphosphonic acid)-doped Polybenzimidazole," *Sci. Rep.*, vol. 3, p. 1764, 2013.

[103] M. C. Evora, D. Klosterman, K. Lafdi, L. Li, and L. G. A. Silva, "Mechanism of electron beam radiation damage on carbon nanofiber surface," *UV EB Tech. Conf. Proc.*, 2012.

[104] A. Pandy *et al.*, "A Carbon Corrosion Model to Evaluate the Effect of Steady State and Transient Operation of a Polymer Electrolyte Membrane Fuel Cell," *J. Electrochem. Soc.*, vol. 160, no. 9, pp. F972–F979, Jun. 2013.

[105] J. Rankin and L. A. Boatner, "Unstable Neck Formation during Initial-Stage Sintering," *J. Am. Ceram. Soc.*, vol. 77, no. 8, pp. 1987–1990, Aug. 1994.

[106] P. J. Ferreira *et al.*, "Instability of Pt/C Electrocatalysts in Proton Exchange Membrane Fuel Cells A Mechanistic Investigation," *J Electrochem Soc*, vol. 152. pp. A2256--A2271, 2005.

[107] H. Baker and H. Okamoto, "ASM handbook," *ASM Int.*, 1992.

[108] R. C. Snyder and M. F. Doherty, "Faceted crystal shape evolution during dissolution or growth," *AIChE J.*, vol. 53, no. 5, pp. 1337–1348, May 2007.

[109] I. McCue, J. Snyder, X. Li, Q. Chen, K. Sieradzki, and J. Erlebacher, "Apparent inverse Gibbs-Thomson effect in dealloyed nanoporous nanoparticles," *Phys. Rev. Lett.*, vol. 108, no. 22, 2012.

[110] J. Snyder, I. McCue, K. Livi, and J. Erlebacher, "Structure/Processing/Properties Relationships in Nanoporous Nanoparticles As Applied to Catalysis of the Cathodic Oxygen Reduction Reaction," *J. Am. Chem. Soc.*, vol. 134, no. 20, pp. 8633–8645,

May 2012.

[111] M. Oezaslan, M. Heggen, and P. Strasser, “Size-Dependent Morphology of Dealloyed Bimetallic Catalysts: Linking the Nano to the Macro Scale,” *J. Am. Chem. Soc.*, vol. 134, no. 1, pp. 514–524, Jan. 2012.

[112] X. Li *et al.*, “Dealloying of Noble-Metal Alloy Nanoparticles,” *Nano Lett.*, vol. 14, no. 5, pp. 2569–2577, May 2014.

[113] C. Baldizzone *et al.*, “Stability of Dealloyed Porous Pt/Ni Nanoparticles,” *ACS Catal.*, vol. 5, no. 9, pp. 5000–5007, Sep. 2015.

[114] C. Jeyabharathi *et al.*, “Time evolution of the stability and oxygen reduction reaction activity of ptcu/c nanoparticles,” *ChemCatChem*, vol. 5, no. 9, pp. 2627–2635, 2013.

[115] H. Wise and J. Oudar, *Materials and Concepts in Surface Reactivity and Catalysis*. New York: Dover Publications, 1990.

[116] A. Schlapka, M. Lischka, A. Gross, U. Kasberger, and P. Jakob, “Surface strain versus substrate interaction in heteroepitaxial metal layers: Pt on Ru(0001),” *Phys. Rev. Lett.*, vol. 91, no. 1, p. 016101/1-016101/4, 2003.

[117] Y. Tang *et al.*, “Temperature Dependent Performance and In Situ AC Impedance of High-Temperature PEM Fuel Cells Using the Nafion-112 Membrane,” *J. Electrochem. Soc.*, vol. 153, no. 11, p. A2036, 2006.

Vita

SomayeSadat Rasouli obtained her Bachelor's Degree from Iran University of Science and Technology and her Master's Degree from the Tarbiat Modares University in Teheran, Iran, both in Materials Science & Engineering-Ceramics. In August 2011, she started her PhD in Material Science and Engineering Program at the University of Texas at Austin. During the course of her PhD, she received the Microscopy and Microanalysis Student Scholar Award, Professional Development Award, Microscopy and Microanalysis Best Poster Award, and Frontiers of Electron Microscopy in Materials Science (FEMMS) Best Poster Presentation Award. While obtaining her degree, she worked as a Teaching Assistant for Materials Processing Laboratory in Mechanical Engineering Department, and Graduate Research Assistant in Materials Science and Engineering Program. She also worked as a Visiting Researcher at Kyushu University, Japan, International Institute for Carbon Neutral Energy Research (I^2CNER) in Fukuoka, Japan, as well as Arizona State University in Tempe, AZ.

Permanent Address: No 47, 29th St. Gisha Avenue, Tehran, Iran.
This dissertation is typed by SomayeSadat Rasouli.